COHERENT PLASMON COUPLING IN SPHERICAL METALLODIELECTRIC MULTILAYER NANORESONATORS

by

CHARLES ALAN ROHDE

A DISSERTATION

Presented to the Department of Physics
and the Graduate School of the University of Oregon
in partial fulfillment of the requirements
for the degree of
Doctor of Philosophy

September 2008

University of Oregon Graduate School

Confirmation of Approval and Acceptance of Dissertation prepared by:

Charles Rohde

Title:

"Coherent Plasmon Coupling in Spherical Metallodielectric Multilayer Nanoresonators"

This dissertation has been accepted and approved in partial fulfillment of the requirements for the Doctor of Philosophy degree in the Department of Physics by:

Jens Noeckel, Chairperson, Physics
Miriam Deutsch, Member, Physics
Gregory Bothun, Member, Physics
Michael Raymer, Member, Physics
Jeffrey Cina, Outside Member, Chemistry

and Richard Linton, Vice President for Research and Graduate Studies/Dean of the Graduate School for the University of Oregon.

September 6, 2008

Original approval signatures are on file with the Graduate School and the University of Oregon Libraries.

An Abstract of the Dissertation of

Charles Alan Rohde for the degree of Doctor of Philosophy

in the Department of Physics to be taken September 2008

Title: COHERENT PLASMON COUPLING IN SPHERICAL METALLODIELECTRIC MULTILAYER NANORESONATORS

Approved: _____

Dr. Miriam Deutsch

In this thesis we theoretically and experimentally investigate the subwavelength manipulation of light with nano-scale patterned metallodielectric resonators. By coupling light to surface plasmon excitations, we calculate the modified dispersion relation of the resulting surface plasmon polartion (SPP) modes in two types of subwavelength resonators: (i) closed, spherical micro-resonators with nano-scale metal-dielectic-metal shells; (ii) periodic, metal-dielectric-metal-layered silica surfaces.

We show theoretically that with the proper geometric parameters, one can use subwavelength structure on spherical surfaces to manipulate the SPP dispersion relation in a highly tunable fashion. A tunable avoided-crossing of plasmonic dispersion bands is found to be the result of the coherent near-field coupling of silver nano-shell SPP modes. By developing our own stable computational algorithms, we calculated

the far-field scattering of these metal-dielectric-metal layered micro-resonators. We demonstrate that the near-field interaction of the SPPs leads to a tunable, SPP induced transparency in the composite particle's scattering and extinction cross-sections.

Utilizing finite element calculations, periodically-modulated metal-dielectric-metal layers are shown to alter the transmission properties of plasmon enhanced transmission through their support of interior surface plasmon (ISP) modes. Our simulations indicate that, subwavelength silver-silica-silver trilayers coating arrays of silica cylinders support ISP modes analogous to those found in spherical metal-dielectric-metal shells. We examine the coupling between ISP and radiating SPPs, and find the possibility of efficient free-space coupling to ISP modes in planar geometries. Further, the excitation of these ISP modes is found to predicate plasmon enhanced transmission, adding directionality and refined frequency selection.

Experimentally, we show that self-assembled monolayers of silica spheres form a novel substrate for tunable plasmonic surfaces. We have developed a deposition method to conformally coat these hexagonal-close-packed substrates with nano-scale silver-polystyrene-silver coatings. We use angle-resolved spectroscopy to study their transmission properties. We have discovered that the presence of the silver-polystyrene-silver layer supports the excitation of ISP modes, and that these excitations significantly alter the plasmon enhanced transmission. Finally, we have discovered that the use of the ordered monolayers as a plasmonic substrate can create a new effect in conjunction

with plasmon enhanced transmission: directionally asymmetric transmission. This is demonstrated with optically thick silver coatings evaporated upon onto the ordered sphere monolayers.

CURRICULUM VITAE

NAME OF AUTHOR: Charles Alan Rohde

PLACE OF BIRTH: Saginaw, Michigan

DATE OF BIRTH: May 10, 1977

GRADUATE AND UNDERGRADUATE SCHOOLS ATTENDED:

University of Oregon, Eugene, Oregon
Michigan Technological University, Houghton, Michigan

DEGREES AWARDED:

Doctor of Philosophy in Physics, 2008, University of Oregon
Master of Science in Physics, 2005, University of Oregon
Bachelor of Science in Physics, 2000, Michigan Technological University

AREAS OF SPECIAL INTEREST:

Optics, Photonics, and Plasmonics.

PROFESSIONAL EXPERIENCE:

Graduate Research Assistant,
University of Oregon, 2001 - 2008
Post-baccalaureate Student Intern
Los Alamos National Laboratory, 1999-2001
Undergraduate Research Assistant
Michigan Technological University, 1997-1999

GRANTS, AWARDS AND HONORS:

National Science Foundation, Integrative Graduate Education and Research Traineeship Fellow (2002)
Los Alamos National Laboratory Distinguished Performance Team Award (2000)
LANL Nonproliferation and International Security Division Student Scholarship (1999)
National Merit Scholarship Finalist (1995)

PUBLICATIONS:

Charles Rohde, Keisuke Hasegawa, and Miriam Deutsch, Optics Letters **32**, 415 (2006).

Keisuke Hasegawa, Charles Rohde, and Miriam Deutsch, Optics Letters **31**, 1136 (2006).

C. A. Rohde, K. Hasegawa, and Miriam Deutsch, Physical Review Letters **96**, 045503 (2006).

Charles Rohde, Keisuke Hasegawa, Aiqing Chen, and Miriam Deutsch, Materials Research Society Symposium Proceedings **846** (2005).

ACKNOWLEDGEMENTS

I would like to thank the following people who labored with me or or by my side as I have struggled to achieve. Thank you to my parents Charles and Diana Rohde, and to my siblings Julia, Cynthia, and David Rohde; to my friends both old and new(er): Brian Weeden, Natasha Sefcovic, Alysia McLain, Aaron Morrison, Brock Bose, Danniel Cassel, and "da' Man Ranch"; thank you to the influential teachers in my life: Dan Sealey, Gary Barker, Rose Nickodemous, William Slough, and Bob Weidman; to my research colleagues (both in and out of school): Keisuke Hasegawa, Eric Hoffmann, Larwarence "Mick" Davis, and Peter Erslev; and finally, a thank you the mentors and advisors that have most strongly influenced the direction of my work and my professional life: Ken Flurchick, Bruce Rafert, Anthony Davis, and Miriam Deutsch.

This thesis is dedicated to my better (though too often, distant) half: Amy C. Mills.

TABLE OF CONTENTS

Chapter Page

Chapter Page

LIST OF FIGURES

Figure Page

Figure Page

Figure Page

Figure Page

Figure Page

Figure Page

LIST OF TABLES

CHAPTER I

INTRODUCTION

Historical Context and Introduction

In this thesis, we examine the interaction of light[1] with structured metal surfaces which vary on scales much smaller than that of the external free space wavelength (λ_0). In this, we are part of a new optics frontier, bringing manipulation of light down to length scales on the order of tens of nanometers. This is made possible by the existence of bound surface waves, called surface plasmon polaritons (SPP) at the interfaces between metal and insulating materials. This revolution in the way we think about controlling light waves has been brought about by the substantial advances in the fabrication of nano-scale metallic surface features, modern optical characterization techniques, the availability of powerful computational tools, and an increasing pressure to create nanoscale integrated devices [1]. In this thesis, we will utilize all of these enabling aspects to study the effects of coherent coupling of SPP surface waves on and between spherical and hemispherical metal-dielectric (MD) interfaces.

For approximately one-hundred years, studying the interaction of electromagnetic

[1]Note that "light" in this work refers to electromagnetic radiation in the visible and near-infrared regions of the electromagnetic spectrum (400nm-1000nm). Other electromagnetic spectral regions will be denoted with their conventional labels: microwaves, terahertz, etc.

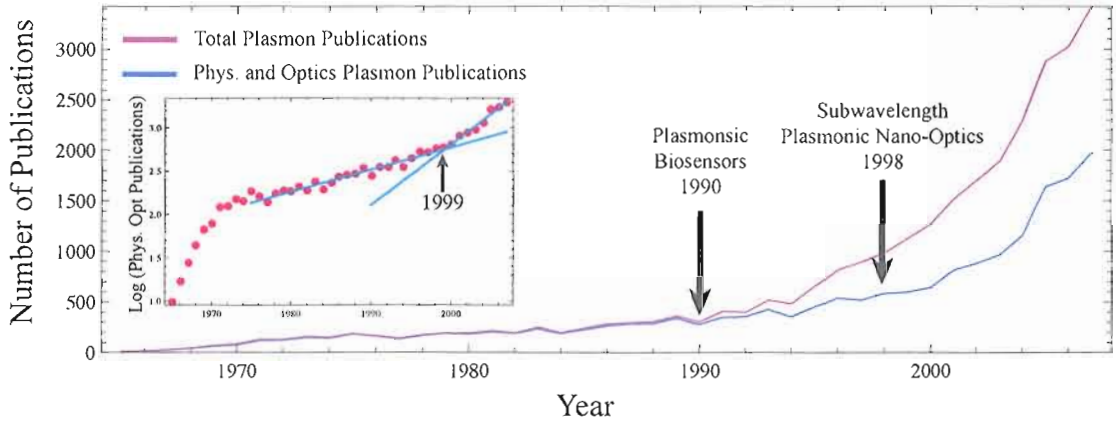

Figure 1.1. Papers with the topic of "plasmons," as retrieved from, and analyzed with, the ISI Web of Knowledge database. [7] (blue curve) analysis is limited to ISI's physics and optics subcategories. The difference from the total can mainly be attributed to the use of plasmonic sensors in the life sciences. (inset) Log of physics and optics publications illustrating the scale break correlated with the start of the study of plasmons in coherent nano-optics. Blue lines are linear fits to the data from 1986-1996 and from 2000-2007.

(EM) radiation at the interface of metals and insulators has piqued the interest of many physical-scientists. Over the past two decades there has been an explosion in the amount of research contributed to this field, figure 1.1. From their beginnings, these investigations have been driven by a wealth of possible applications, and have been made possible by technological advances in our ability to manipulate the structure of metal-insulator interfaces on an ever decreasing size scale. From its theoretical foundations (Sommerfeld [2], Zennek [3], and Mie [4]) and its experimental beginnings (Wood [5] and Farady [6]) has sprung the modern field of surface plasmon polaritons: the coupling of the EM field and the nano-structured metallic surfaces of today's most advanced materials science technologies.

Delocalized Surface Plasmon Polaritons

Central to the optical study of nano-structured metal surfaces is the coherent excitation of the conduction electrons at the metal-insulator interface. The earliest theoretical work on this concept is generally considered to be Sommerfeld's and Zennek's studies of radio frequency surface waves along finite conductivity wires and planes. Experimentally, in 1902 Wood found "most remarkable" [5] the rapid intensity variation in some spectral emission lines, upon reflection from the surface of a metallic grating. Nearly forty year later, Wood's "almost incomprehensible" [5] anomalous diffraction was brought together with Sommerfeld's bound surface wave by Fano [8]. This work combined the coupling of the freely propagating EM wave continuum with radiating surface currents at optical frequencies. Finally, Ritchie [9] linked this previous work and that of thin film electron electron loss spectroscopy [10, 11] bringing together and solidifying the field of bound surface waves at metal-insulator interfaces under the single rubric of surface plasmon polaritons (SPP).[2]

As will be discussed more formally in chapter II, the high mobility of a metal's (essentially free) conduction electrons allows excitation of ensemble plasma oscillations against the restoring force of the ionic lattice background. Provided that both energy and momentum are conserved, these coherent oscillations can be excited with both charged particle bombardment and external EM waves. In this thesis, we are only concerned with the subset of oscillations that exist exclusively at the metal surface

[2]Although it is only in the context of surface plasmons coupled to EM-fields that the addendum polariton is added, this is the exclusive condition under which we will be operating in this work.

that are referred to as surface plasmons (in opposition to the bulk plasmon excitation). These SP excitations are bound to the metal-insulator interface, and as such they possess a maximum electromagnetic field intensity at the interface and evanescently decay into the adjacent media. The decay lengths of these exponential tails are on the order of tens of nanometers on the the metal side of the interface and on the order of hundreds of nanometers on the insulator side. Because they are confined to dimensions smaller than the free space wavelength in the single dimension perpendicular to the interface, the lack of confinement in the remaining two dimensions allows the SPPs to freely propagate along the surface. As such, this class of SPP excitations are referred to as delocalized. This distinguishes them from localized SPP excitations, where variations in the interface nanoscale geometry further restrict the SPP decay length in all three dimensions.

Localized Surface Plasmons

Since the seminal work of Mie in 1908 [4], it has been recognized that metal particles with small radii (with respect to an incident wavelength, $r \ll \lambda_0$) support resonant modes that result in very large absorption. This phenomenon can be attributed to localized surface plasmons, and it can be observed in every-day contexts such as the color of artisan stained glass and some ceramic glazes. Since Roman times, it has been known that mixing metals such as silver and gold with glasses, ceramics, and dyes can add spectacular color to the work [12]. In 1857, Faraday [6] was the first to purposely create pure colloidal suspensions of monodisperse gold nanoparticles for

optical investigation. When viewed in transmission, these colloidal solutions exhibit the rich red color indicative of the localized gold plasmon dipole resonance.[3] It is due to the very small size of the gold particulates ($r \sim 10$nm) that the solution color is no longer "gold." The lowest order spherical absorption resonance for 10nm gold nanoparticles is centered in the green part (500nm, c.f. chapter III) of the optical spectrum. The green absorption thus results in the weighted transmission of red light.

As will be examined in detail in chapter III when the metal particles become larger, and/or are coated with additional shells of insulating and metallic materials, this simple picture of dipole plasmon excitation becomes much more complicated. By implementing an extend form of Mie's curvilinear scattering theory we will explore the effects on SPP coupling by multi-shell plasmonic particles whose radii are on the same scale as that of the incident EM wavelength. This will lead us to several fascinating effects, including nano-engineered coatings that can induce both enhanced electromagnetic absorption, narrow frequency scattering transparencies. We will also go beyond Mie's scattering theory, and its multi-shell extensions, to examine theoretically and experimentally the effects of thin, fractal, silver shells on the spherical surface plasmon resonance.

Because the SPP is the result of the coupling of freely propagating EM radiation and these various surface modes, it can be regarded as the propagation of a bound (or guided) photon with a modified dispersion relation. It is this one-to-one

[3]It is interesting to note that these suspensions are highly stable, and that in fact, you can still view the original gold colloids created by M. Faraday at the Royal Institution of Great Britain [13].

correspondence between SPPs and photons, and the extreme sensitivity of SPPs to nano-scale surface structure, that has rekindled the interest of the physics community. In the next section, we will look at this renewed study of SPP properties in novel nano-scale geometries. We will show that it has led to many recent discoveries in the sub-wavelength control of EM radiation, and holds the promise to create sensors that may be able to "see" single molecules.

Modern Use and Research of SPPs

In many modern industries there exists the technological pressure to generate smaller, more efficient, and cheaper material structures in a wide variety of applications. This is especially true in the information technology and biomedical industries. The race to keep pace with Moore's "law"[4] and the investigation of biological systems at the sub-cellular level is manifesting as a huge drive towards creating nano-scale solutions. In both biology and the semiconductor industry, light has historically been used as the primary tool for non-invasive investigation and process control. The fundamental barrier of the diffraction limit (limiting resolution to $\sim \lambda/2$) hinders the future use of freely propagating and guided optical light in such nano-scale applications. However, as has been recently discovered [15], we can utilize SPPs as a tool to manipulate EM fields at optical and near-infrared frequencies in volumes much smaller than the free space diffraction limit would otherwise allow. In addition to

[4]In 1965 IBM cofounder Gordon Moore noted the annual doubling trend of IC component density [14]. With nearly 50 years of industry adherence this trend has taken on the force of law.

increased resolution, the sensitivity of the SPP resonance to the complimentary dielectric environment creates the possibility of using delocalized and localized SPPs as extremely sensitive surface detectors [16] and nanoscale labels for subwavelength biomedical imaging [17, 18].

The above enumerates the two main branches of plasmon application. These can be broadly separated into the two categories of subwavelength optics ("light-on-a-chip") and SPP based sensors ("lab-on-a-chip"). As the colloquial names suggest, both objectives aim towards creating compact and complete solutions to technological problems such as integrated optical circuits and immunoassay of biologically interesting molecules. The large, exponentially decaying EM fields at the metal-insulator interface produced by SPPs allows them to be both highly confined, and highly sensitive to/influential on their immediate environment. The quest to structurally control and measure the SPP near-field energy distribution comprises a major part of the research of SPPs for real world applications. Below we briefly outline some current active areas of research in the field of SPP manipulation which are the most relevant to our work.

Coherent Nanophotonics and Plasmonics

Sub-Wavelength Confinement of Light

In 1998, Ebbesen, et al. published their work on the extraordinary transmission of visible light through arrays of subwavelength cylindrical holes in metallic films [19]. As illustrated in figure 1.1, this publication created a renewed interest in surface plasmon research within the physics and optics community for their use in the sub-wavelength manipulation of EM fields.

The potential of SPPs to create active and passive optical elements on scales far below the diffraction limit may bring integrated optical components down to the same length scale as their electronic counterparts ($<$ 100nm). There are a wide variety of paths currently being pursued to achieve this goal. The most promising geometric configurations proposed are: thin ($\sim 10nm$) metal strips (dielectric-metal-dielectric, DMD, films) [20], nanoparticle chains and arrays [21, 22], and metal-dielectric-metal (MDM) structures[5] [23–25]. On top of these "basic" substrates, further control can be gained from adding patterning and/or periodic structure to create SPP analogs of waveguides [26, 27], lenses [28, 29], Bragg reflectors, beam splitters, and other passive optical elements [30].

Multilayer plasmonic (specifically MDM) structures, such as we are studying, are a very promising avenue to creating highly confined optical components with

[5]MDM structures are also called gap and channel configurations, because the SPP is confined to the small dielectric space interior to two metal interfaces.

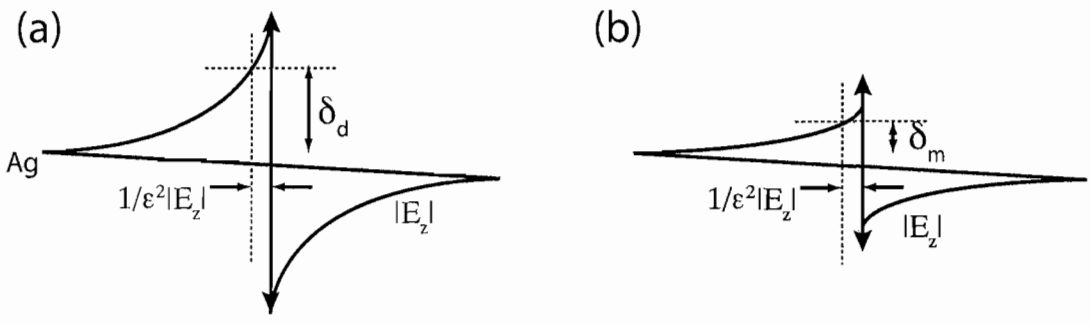

Figure 1.2. Schematic comparison of (a) a DMD strip SPP waveguide to a (b) MDM SPP waveguide. The strip guide has a propagation length on the order of centimeters, and weak confinement perpendicular to the metal interface ($\gtrsim 5\,\mu$m). MDM SPP waveguides have propagation lengths $\sim 100\,\mu$m and perpendicular confinement $\sim \lambda_0/10$.

reasonable propagation lengths. In SPP systems there is an inherent correlation between increased confinement and increased loss. This has historically limited their usefulness as a ultra-high density component of nano-scale optical circuitry. Strip wave guides (DMD structures) have recently been proposed as a low loss (long range propagation) alternative to single interface SPP waveguides.

However, strip waveguides posses low loss because the thin ($\sim 10nm$) metal strips guiding the SPP force much of the electric field of the plasmon into the adjacent dielectric. This causes the extended decay length of metal strip SPPs into the adjacent dielectric. This can cause the SPP excitation to extend into the dielectric as far as 5μm from the metal strip (figure 1.2). This places severe restrictions on the scalability of SPP based strip waveguides in high component density applications.

In contrast, Zia, et al. have demonstrated that MDM waveguides can achieve

high component densities ($\sim 10^4$/m) while maintaining propagation lengths of $\sim$ 50μm [25]. Further, Veronis and Fan [24] have theoretically shown that MDM waveguides can be fashioned with no propagation loss around very sharp bends approaching 90°. It has also been shown that MDM waveguides can simultaneously support both plasmonic and conventional waveguide modes for gap sizes on the order of 100nm [23]. We distinguish conventional waveguide modes from SPP guided modes, as those that posses significant wave-vector components perpendicular to the metal interface. This dual support is important from the point-of-view of coupling conventional guided waves to SPP MDM waveguide modes [1]. In chapters V and VII we will explore the free-space coupling and dispersion characteristics of such MDM SPP modes on periodically modulated surfaces.

Metamaterials

Two other applications of subwavelength MDM layers are found in the construction of optical metamaterials [31, 32]. An optical metamaterial is a material whose geometric structure defines, in whole or in part, its optical properties. Given the effects of nano-scale structure on the propagation and coupling of SPPs, it should not be surprising that plasmonic multilayers can play an important role in the creation of such materials [33]. Two concepts which have sparked a great amount of research are the "perfect lens" [34] and EM cloaking [35–37]. As illustrated in figure 1.3, the perfect lens proposed by Pendry utilizes the special metamaterial property of neg-

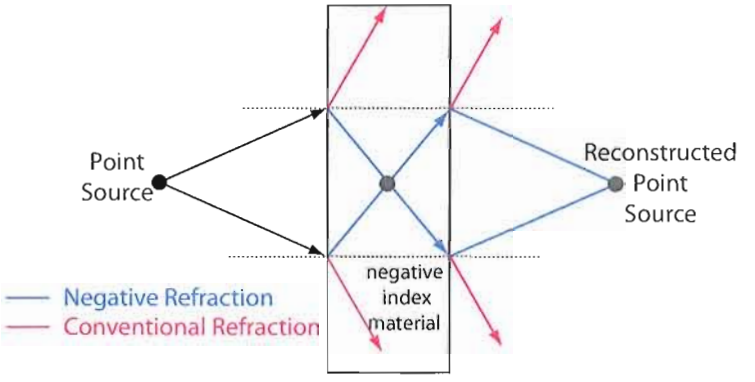

Figure 1.3. A slab of negative index material reconstructs point sources in the near-field with resolution greater than the diffraction limit. The refracted wave-vector into a negative index material remains on the same side of the surface normal as the incident wave-vector. A conventional material refracts on the opposite side of the surface normal.

ative refraction to create images with resolution greater than the diffraction limit with flat surfaces. Through similar mechanisms, Pendry, et al. and Alŭ and Engheta have independently proposed methods to hide objects from impinging EM radiation. We have also made contributions to this last area of EM particle cloaking, and we examine the effects of plasmon induced transparency in chapter III.

These ideas are made possible through the exploitation of nanoscale metallic resonator configurations to create artificial optical magnetic resonances (optical "magnetic-atoms") [38]. With MDM geometries, materials that possesses simultaneous negative permitivity and negative permeability can be created. Such materials are referred to as negative index materials (NIM), left-handed materials, or doubly negative materials. They derive their name and effects from the fact that phase and group velocities in such materials are anti-parallel [39]. NIMs have been proposed theoretically [34],

and shown experimentally in the microwave region [40] to construct lenses that can reproduce near-field images that surpass the diffraction limit. While NIM materials have been produced in the gigahertz [41] and terahertz [42] frequencies, there is currently a major research thrust to produce NIM materials at optical frequencies [31]. A wide variety of approaches are currently being pursued including periodic nanoparticle arrays [43], disordered nanoparticle arrays [44], and planar MDM structures [45].

Optical cloaking has been suggested as another application of plasmonic metamaterials. Through the use of effective negative index materials and/or plasmonic coatings Alŭ and Engheta have proposed the shielding of small ($r \ll \lambda_0$) dielectric and metallic particles from external EM fields [35]. We have extended this work, theoretically demonstrating that it is possible to greatly reduce the scattering of micron-scale metal and dielectric particles through SPP-SPP coupling inherent in MDM geometries [46]. Our work and that of Alŭ and Engheta constitute only a restricted subset of the possibilities for EM cloaking with metamaterials. In 2006 Leonhardt has formally shown the needed dielectric functional dependence to conformally map the path of a propagating ray incident upon a spherical shell onto the optical path of a ray traveling through empty space [36]. The affected rays are excluded from the region inside the shell material, and instead are bent around it, reemerging from the shell as though no interstitial interaction has taken place. Pendry, et al. have used a metamaterial shell to apply this mapping, and thus shown that it is, in principle, possible to generate shells with the needed radial and azimuthal dielectric functional

dependence. They have also extended the concept past the originally proposed ray approximation, and theoretically demonstrated that lossy materials can act as imperfect cloaks [37]. These functional dependencies have been simplified to dielectric functions that need only radial variation in the 2D case of cylinder cloaks. This has allowed the experimental demonstration of imperfect optical cloaking at microwave frequencies utilizing split ring resonator metamaterials [47] and at visible frequencies in 2D geometries with propagating plasmon modes and multishell MDM structures [48]. In imperfections in the cloaking come from both material loss and the approximations producing the simplified dielectric variation with respect to the complete conformal mapping solution.

These two applications only are a small piece of the large amount of research on metamaterials formed through metallodielectric subwavelength structure. With the vast number of continuing publications it seems that only imagination and the speed with which the newest MD_x pattern can be laid down with ion milling, electron lithography or self-assembly limits the potential for new applications.

Plasmon Based Sensors

The large field enhancement and strong localization of SPPs near the metal-insulator interface presents the opportunity to utilize SPPs as extremely sensitive sensors of the local interface environment. SPPs based sensors can be utilized to detect changes in the index of refraction at the MD interface through shifts in the delocalized surface plasmon resonance (SPR) [16] of smooth interfaces, and alter-

ations in the localized surface plasmon resonance (LSPR) of nanoparticles [49–51]. Or, selective molecular detection is made possible by exploiting the localized SPP EM field to enhance nonlinear Stokes and anti-Stokes emission from molecules adsorbed onto a rough metal surface, an effect known as surface enhanced Raman spectroscopy (SERS) [52]. In addition, with the absorption inherent in the LSPR, noble metal nanoparticles have found use as nanoscale labels in a variety of biological investigations such as fluorescence spectroscopy and nanoparticle immunoassay [18].

Surface plasmons began to be used as sensors for biologically interesting molecules around 1990 [53–56]. From figure 1.1 one can surmise the large impact that this has had on SPP application as a detection tool. Their strength comes from the extreme sensitivity that the SPP excitation provides. Through functionalization of the metal surface or nanoparticles, selective binding of specific molecules to the functional group can can be monitored at very low concentrations [57]. Typically gold interfaces are used due to their lack of toxicity, and their well developed surface chemistry. The latter allows the attachment of gold nanoparticles to many types of molecules through surface functionalization with sulphur terminated ligands [12]. In cases where toxicity is not an issue, silver is also used, because of its stronger SPR dielectric sensitivity [58].

The shift in the SPR of delocalized SPPs is currently used extensively in a number of sensor schemes [16, 59, 60]. However, much of the current research work is concentrated on the use of LSPRs of tailored nanoparticles to achieve the highest sensitivities. McFarland et al. have measured concentrations of 1-hexadecanthiol at

the 100 zeptomolar level [61]. The high sensitivity of this experiment is the result of the large particle LSPR (~40nm) shift incurred upon the adsorption of a self-assembled molecular monolayer. This concentration is equivalent to $\sim 10^5$ molecules adsorbed onto the surface of a silver nano-particle with a surface area of $\sim 10^4 \text{nm}^2$. The monolayer coating thus changes the local dielectric response nanoparticle, yielding a far-field macroscopic change in the frequency of the absorbed light. Haes et al. have furthered this work and reported detection of $\lesssim 10^3$ streptavidin molecules by monitoring the LSPR of individual silver particles in silver nanoparticle arrays with dark-field microscopy [51].

This work is bringing the sensitivity levels of LSPR detection down to those found in SERS based sensors. In SERS both SPP field enhancement and SPP localization (due to nanoscale roughness) conspire to create huge enhancements of the scattered Stokes emission. It has been claimed that the presence of single rhodamine 6G dye molecules on a rough silver surface have been detected [62, 63]. This represents localized EM field intensity enhancements on the order of 10^{14}. While this is a controversial result, it is generally accepted that very large enhancements are possible due to the presence of LSPRs on rough metal surfaces. Utilizing arrays of silver "bow-tie" nano-antenna resonators, Haynes et al. demonstrated the beneficial results of using tailored SPPs surfaces to create SERS enhancement factors on the order of 10^{10} [64].

The tailoring of surfaces for use in surface enhanced Raman spectroscopy (SERS)

and sensor technologies are the most relevant sensor applications to the work done in this thesis. We have shown in previous work that LSPRs on the surface of silver coated silica microresonators can be coherently coupled through the resonator Mie resonances [65]. Because Mie resonances are tunable with the particle radius, this may provide an additional tuning parameter for creating tailored LSPR surfaces.

As one may imagine there is a very large amount of work in other areas that has investigators examining the properties of SPPs. It is worth briefly mentioning the breadth of applications for which SPPs are currently being investigated. These other directions of research include: low volume temperature sensing [66], cancer therapy [17], photo-induced drug delivery [67], enhanced absorption in silicon solar cells [68], nanoscale circuitry elements [69], subwavelength microscopy[70], plasmon photolithography [71, 72], entanglement of photons [73], single photon transistors [74] and active plasmonic devices such as surface plasmon lasing [75]. While this list is in no way complete, it gives the reader the sense of the amazing utility of a metal-insulator interface that can be controlled on the nano-scale. With this in mind we go forward with our own specific investigations of SPPs that exist on the boundaries of spheres and hemispheres. We hope to show that new and interesting effects continue to come out of Maxwell's equations and classical physics even 100 years after Zennek and Sommerfeld first contemplated bound waves at the surface of a finite conductor.

The Motivation for Investigating SPPs on Curved Surfaces

A defining characteristic of the SPP excitation is its bound nature. We have seen above the usefulness resulting from confining the EM field to the MD interface. However, this can also be a major hindrance. The momentum missing from a propagating photon that is associated with its binding to the metal surface doesn't allow direct coupling to SPPs on flat MD interfaces. One way to overcome this is through the high degree of curvature present at the surface of a metal sphere with a diameter smaller than, or comparable to, an impinging planewave ($r \lesssim \lambda_0$). A second useful characteristic of spherical MD-interfaces is the SPR tunability parameterized by the radii of nobel metal nanoshells. Prodan et al. have shown that it is possible to tune the SPR of metallodielectric core-shell particles across the visible-NIR spectrum [76] .

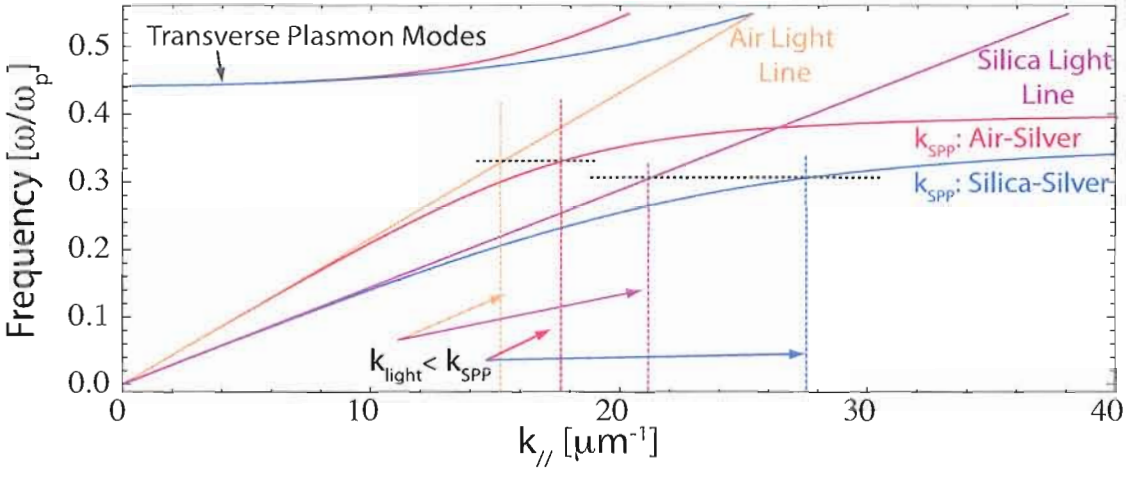

Figure 1.4. Dispersion relations for SPPs on air-silver and air-silica interfaces. Also plotted are the light lines in air $k = \omega/c$ and silica $k = n_{silica}\omega/c$. $k_{light} < k_{SPP}$ reflecting the bound nature of SPP modes, and their smaller effective wavelength.

This is made possible due to plasmon hybridization resulting from SPP-SPP coupling through the thin metal shell resting on the dielectric core. As will be discussed in more detail in chapter IV the coupling of SPPs on the shell's interior and exterior results in the splitting of the SPP resonance frequency with one resonance branch continuously pushed through the visible/NIR frequency spectrum as the core and shell radii are varied.

We are interested in studying SPPs on spherical surfaces to exploit this tunability and to investigate new mechanisms for additional SPP-SPP coupling. In chapter IV we exploit the coupling of SPPs between multiple silver-titania shells to theoretically demonstrate plasmon induced transparency (PIT) in micron-scale MDM multishell particles at visible wavelengths [46]. Once again, PIT is a consequence of coherent plasmon coupling induced hybridization. This time the coupling exists between the delocalized shell plasmons formed in the interior dielectric gaps and exterior SPPs on the outer surfaces of a multi-shell MDM particle. Because of their strong coupling to plane-waves, this near-field coupling of the plasmon resonances results in a reduction in the far-field scattering cross section of the MDM particle.

In addition to simply curving a surface, periodic modulation of a flat surface can also result in coupling between free-propagating EM waves and surface plasmons. When a planar interface is periodically modulated the missing free photon momentum can be gained from scattering at the modulated surface. When combined into a periodic hexagonal-close-packed lattice through evaporative self-assembly, silica spheres

create a 3-dimensionally modulated substrate. We coat this surface with an MDM trilayer to create a novel plasmonic surface that allows the far field investigation of delocalized MDM SPP-SPP coupling with angle-resolved extinction spectroscopy.

Thus, the presence of spherical curvature allows the coupling of radiating EM waves to surface plasmons in both localized and delocalized regimes with a set of tunability parameters via the various geometric radii. The tunability of the SPRs found in spherical shells brings forth exciting possibilities for future applications, and it is the radiative spherical SPP modes that allow us to use far-field scattering techniques to investigate the near-field coherent coupling of SPPs between surfaces and nanoparticles.

Thesis Outline

Chapter II is a brief tutorial of the basic dispersion properties of delocalized SPPs on flat interfaces. In this chapter we review the effects of planar SPP-SPP coupling and the resulting hybrid flat surface SPP modes. The important coupling property of sub-wavelength confinement in MDM structures is also outlined as this will be re-examined in the curved geometries of chapter IV and chapter V.

In addition to reviewing the localized SPP modes excited on spherical nanoparticles, Chapter III introduces the formalism of Mie scattering from an arbitrarily sized spherical scatterer. The effects of plasmon hybridization in spherical metal shells are introduced, and we review the extension of Mie scattering to multiple concentric

spherical shells with absorbing dielectric functions. We also examine the discrete algorithm we have developed to compute scattering from an arbitrary number of absorbing shells and validate its results against other published work.

In Chapter IV we utilize our developed computational resources and analytical methods to examine the effects of coupling of shell SPPs between multiple silver and titania shells. We identify two coupling regimes that delineate weak and strong coupling of external EM fields to SPP excitations on the interior of the particle's multilayer shell. We show that in the weak coupling regime the MDM particle can exhibit greatly enhanced absorption from an engineered flat SPP band. In the strong coupling regime we show SPP-SPP coupling can lead to an induced transparency window for particles with radii on the same scale as the external EM field free-space wavelength ($r \sim \lambda_0$).

In the second part of this work we apply the theoretical ideas developed in the previous chapters to an examination of SPPs in two separate, periodically-modulated, MDM planar systems. First, coupling between SPPs at the surface of silver-silica-silver-coated silica cylinder arrays are computationally examined. With finite element analysis (FEM), the SPP coupling in such periodic MDM coatings are shown, as in the closed resonator case of chapter IV, to support the strong excitation of interior surface plasmon polaritons. Second, coupling between SPP modes in silver-polystyrene-silver coatings formed on top of ordered monolayers of silica spheres are experimentally investigated. The manufacture of periodic MDM surfaces are detailed in chapter VI,

and experimentally studied with angle-resolved spectroscopy in chapter VII. This is experimentally shown to result in the modification of the angular and spectral emission patterns of plasmon enhanced transparency [19].

CHAPTER II

BASIC THEORY OF SURFACE PLASMON POLARITONS

This chapter presents a brief review of delocalized surface plasmons as they pertain to our work. Although all of this information can be found elsewhere [1, 77, 78] we've brought it together here for completeness and to introduce formula and nomenclature for future use. The concept of delocalized SPPs has been briefly introduced in chapter I and will be expanded upon here. Of particular importance is the method used to couple freely propagating light into surface plasmon modes through surface roughness will be discussed. This chapter ends with the important topic of coherently coupling delocalized plasmons through thin, flat metal and dielectric films. This last topic is the precursor to the main focus of this thesis: coupling delocalized plasmons on curved interfaces, and coherently coupling localized plasmons with silica micro-resonators.

Dielectric Function of Metals

The properties of plasmons can be completely described classically, provided that a suitable description of the metal's dielectric function ($\varepsilon_m(\omega)$) is supplied a priori. Thus, before we begin with our discussion of the properties of plasmons, surface plasmons, and surface plasmon polaritons, it will be instructive to examine the frequency response of bulk metals.

To a good approximation the conduction electrons of metal at room temperature can be modeled as a non-interacting free electron gas interacting with the background lattice ions solely through elastic collision events at a frequency γ [79]. From this model (proposed by Drude), we combine quantum corrections from Sommerfeld,[1] add additional empirical corrections accounting for interband transitions, and the band theory of metals[2] to arrive at an adequate expression for $\varepsilon_m(\omega)$:

$$\varepsilon(\omega) = \varepsilon_\infty - \frac{\omega_p^2}{\omega(\omega + i\gamma)} \tag{II.1}$$

Where ε_∞ accounts for the interband contributions to $\varepsilon(\omega)$ from transitions of d-orbital electrons into the s-p conduction band, and ω_p, called the bulk plasmon frequency, is given by [79]:

$$\omega_p \equiv \sqrt{\frac{ne^2}{\varepsilon_0 m^*}}$$

with n being the free electron density, e the electric charge, ε_0 the permittivity of free space, and m^* the electron effective mass.

The Drude-Sommerfeld model does a reasonable job of describing most of the optical properties of silver, the metal used in our work, in the visible/NIR spectrum. Equation II.1 is used when we require an analytical expression for $\varepsilon_m(\omega)$, but when possible, we use the tabulated empirical results for $\varepsilon_{Ag}(\omega)$ complied by Palik [58].

Using the appropriate parameters for silver ($\hbar\omega_p$=9.1 eV, $\hbar\gamma = 0.021$ eV, $\varepsilon_\infty = 5.1$) a comparison of the tabulated data and the Drude-Sommerfeld model is given in figure

[1] use of the Fermi-Dirac velocity distribution for electrons

[2] substitution of an effective electron mass (m^* for m_e)

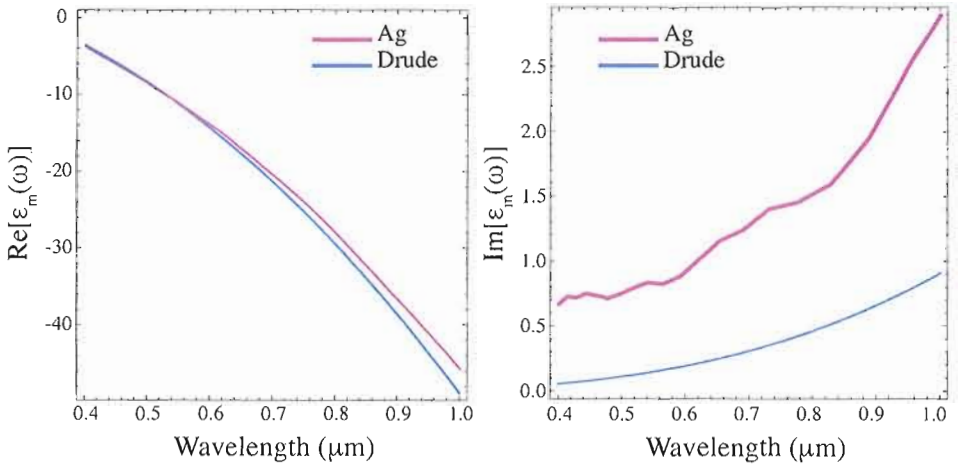

Figure 2.1. Comparison between Drude-Sommerfeld model for $\varepsilon_m(\omega)$ and empirically collected data for silver from Palik [58].

2.1. The agreement is quite good in the visible/NIR region between the real parts of $\varepsilon_m(\omega)$ and $\varepsilon_{Ag}(\omega)$ while the $\mathrm{Im}[\varepsilon_m(\omega)] < \mathrm{Im}[\varepsilon_{Ag}(\omega)]$. The imaginary part of ε_m is proportional to the absorption of energy in the material. The underestimation of $\mathrm{Im}[\varepsilon_{Ag}(\omega)]$ with $\mathrm{Im}[\varepsilon_m(\omega)]$ in some of our theoretical work thus result in reduced absorption and narrower resonance peaks compared to simulations using tabulated and experimental results.

Bulk Plasmons

Bulk plasmons are the longitudinal volume eigenmodes of the collective oscillation of the quasi-free conduction electrons in metal materials. They occur at frequencies where $\varepsilon(\omega) = 0$ (at ω_p for Drude metals). As noted above, ω_p occurs at frequencies in the ultra-violet spectral region for nobel metals such as gold ($\omega_p^{Au} = 138\mathrm{nm}$),

silver ($\omega_p^{Ag} = 136\text{nm}$) and copper ($\omega_p^{Cu} = 141\text{nm}$). EM waves cannot couple to bulk plasmons due to their longitudinal nature, but they set the energy scale for our subsequent discussion of SPPs. The bulk plasmon resonances of silver and gold are close to the visible spectrum. As we will see, the SPP mode frequencies that do couple to EM waves are proportional to ω_p and thus can fall into the visible spectrum. Combined with their low loss this makes silver and gold the metals of choice for the study and use of visible/NIR SPP excitation.

Surface Plasmons at Flat Interfaces

The simplest interface supporting bound surface modes is the flat interface between a metal and a dielectric. The surface plasmons dispersion (energy–momentum) relation for this geometry is given by [1]:

$$k_{sp} = k_0\sqrt{\frac{\varepsilon_d\varepsilon_m}{\varepsilon_d+\varepsilon_m}} = \frac{\omega}{c}\sqrt{\frac{\varepsilon_d\varepsilon_m}{\varepsilon_d+\varepsilon_m}} \tag{II.2}$$

where k_0 is the free space wavevector, ε_d is the dielectric constant of the adjacent insulator and c is the speed of light in vacuum. For metals in the visible/NIR spectral region $\varepsilon(\omega) < 0$. This implies that:

$$\begin{aligned} k_{sp} &= k(1+\delta) \\ &\text{where } \delta \simeq \frac{\varepsilon_d}{2|\varepsilon_m|}\text{, and } k \equiv \sqrt{\varepsilon_d}k_0 \end{aligned} \tag{II.3}$$

Because we assume $\varepsilon_d > 0$, equation (II.3) implies that $k_{sp} > k_0$ by the amount δ. This reflects the bound nature of the surface plasmon wave, and prevents direct coupling of

freely propagating EM waves to such modes. We can see that the resonance condition for the surface plasmon occurs when the real part of the denominator of equation (II.2) is zero. That is when

$$\varepsilon_m = -\varepsilon_d \tag{II.4}$$

If we apply the lossless equivalent of equation (II.1), ($\gamma = 0$), to the surface plasmon resonance condition, equation (II.4), we arrive at an often quoted estimate of the surface plasmon resonance frequency for single flat interfaces:

$$\varepsilon_m(\omega) = \varepsilon_\infty - \frac{\omega_p^2}{\omega^2} = -\varepsilon_d \tag{II.5a}$$

$$\Rightarrow \quad \omega_{sp} = \frac{\omega_p}{\sqrt{\varepsilon_\infty + \varepsilon_d}} \tag{II.5b}$$

We plot $\omega(k_{sp})$ in figure 2.2 for air–silver and silica–silver interfaces. The larger loss in the true dielectric function leads to a significant difference in the k_{sp} wavevector near ω_{sp}, but away from the resonance point the Drude-Sommerfeld model does not deviate greatly from the true dispersion relation.

Coupling to Surface Plasmons

As stated above, freely propagating EM waves do not couple to surface plasmon modes due to the larger surface plasmon momentum ($k_{sp} > k$). There are three mechanisms to overcome this discrepancy: Attenuated total internal reflection, grating, and curvature coupling. These methods utilize diffraction and surface alteration to account for the missing momentum in the free-space wavevector or to alter the

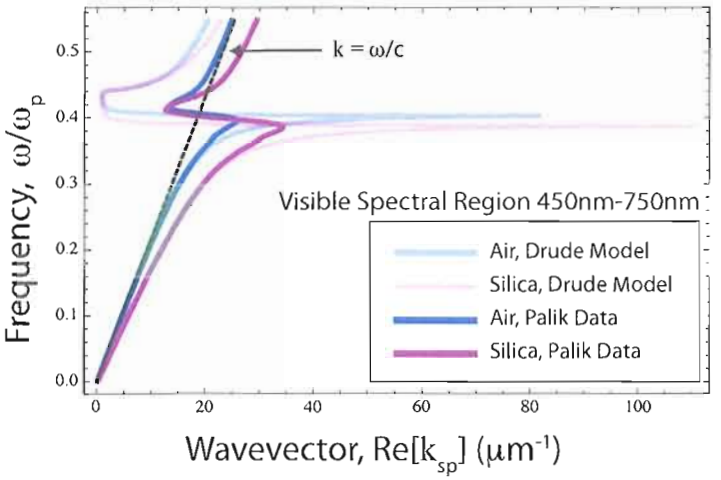

Figure 2.2. The dispersion relation $\omega(k_{sp})$ for two interfaces: air–silver and silica–silver, using the Drude-Sommerfeld model and tabulated values of $\varepsilon_m(\omega)$.

dispersion relation for SPPs to contain radiating modes. Next, we will discuss grating coupling, while curvature coupling will be covered in chapter III. ATR coupling is not used in this work, and the interested reader is encouraged to look at reference [1] for a description of this method.

Grating Coupling

When light scatters from a periodic surface it can gain extra momentum in units of the reciprocal lattice vector(s) $\vec{G} = 2\pi/a\,\hat{g}$. This alters the momentum matching condition, and equation (II.2) should now be written as:

$$k_{sp} = \vec{k_{//}} + m\vec{G_i} \quad m = (1, 2, 3, ...) \tag{II.6}$$

As illustrated in figure 2.3(a), $\vec{k}_{//} = \sqrt{\varepsilon_1}\vec{k}_0 \sin\theta$ is the in-plane component of the incident planewave. Figure 2.3(b) is the electric-field (E-field) intensity distribution

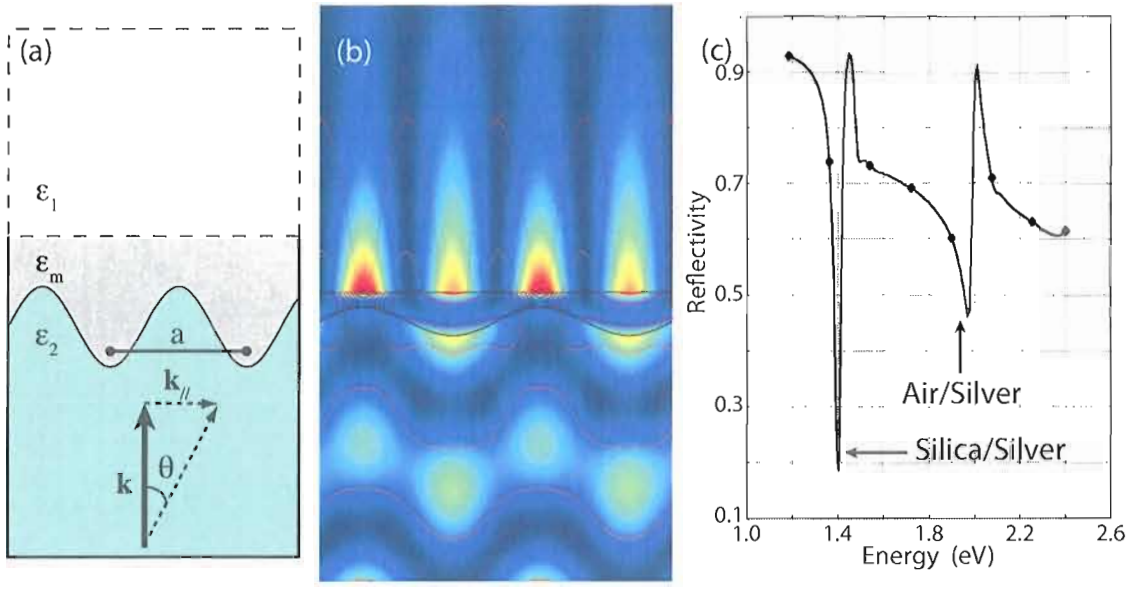

Figure 2.3. Grating coupling to normally incident plane waves. (a) Simple grating and planewave geometry (b) H-field intensity (color map) and E-field intensity (contours) of the air–silica plasmon resonance (c) reflection spectrum exhibiting silica–silver (1.4 eV, 886nm) and air–silver (1.97 eV, 629nm) SPP resonances.

calculated with the finite element method (FEM, cf. chapter V). As shown, a normally incident ($\vec{k_{//}} = 0$) free-space planewave couples to a thin, sinusoidally modulated silver layer laying atop a silica substrate in air. The frequency of the simulation is chosen to be at the frequency of the air-silver SPP resonance ($\hbar\omega = 1.97$eV). Also shown in figure 2.3(c) is the calculated transmission spectrum for the structure shown in figure 2.3(a). This illustrates the fulfillment of the phase matching condition of equation (II.7) at two frequencies: $\hbar\omega = 1.97$eV (air-silver interface) and $\hbar\omega = 1.40$eV (silica-silver interface).

In the case of a 2D grating, additional reciprocal lattice vectors are allowed in equation (II.6). For example, in a hexagonal lattice there are two principle lattice

vectors: $\vec{G}_{\Gamma K} = 4\pi/3a$ and $\vec{G}_{\Gamma M} = 2\pi/\sqrt{3}a$ resulting in the periodic SPP coupling equation:

$$\vec{k}_{spp} = \vec{k_{//}} + m_1\vec{G}_{\Gamma K} + m_2\vec{G}_{\Gamma M} \quad m_1, m_2 = (1, 2, 3...) \tag{II.7}$$

This coupling equation will be revisited in chapter VII when we investigate hexagonally modulated plasmonic surfaces with angle resolved spectroscopy.

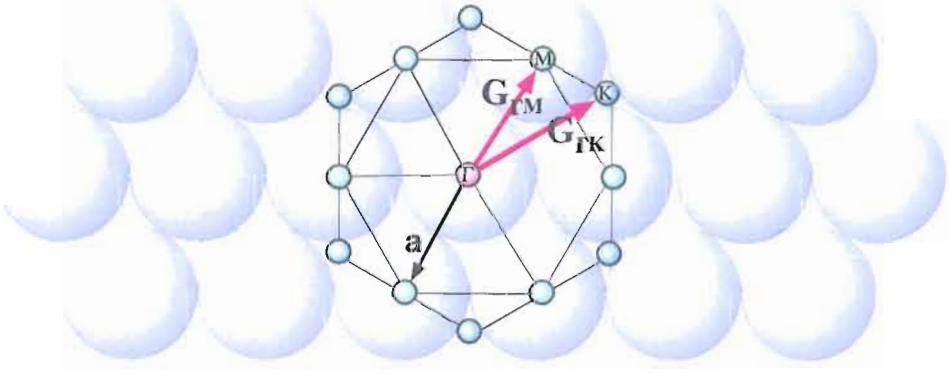

Figure 2.4. Principle reciprocal lattice vectors of a hexagonal lattice: $\vec{G}_{\Gamma K} = 4\pi/3a$ and $\vec{G}_{\Gamma M} = 2\pi/\sqrt{3}a$, superimposed on the hcp structure with lattice constant a.

SPP-SPP Coupling in Flat MD Trilayers

We have so far only reviewed the properties SPPs on isolated single MD interfaces. If we have a system with two or more interfaces spaced closely enough[3] strong coupling of the SPPs associated with each surface will occur. Just as in the case of any linearly coupled system this results in the splitting of degenerate resonance

[3] "closely enough" depends on the medium through which we are coupling. Distances on the order of 100nm is sufficient for dielectrics, but $d \sim 10$nm is needed for metals.

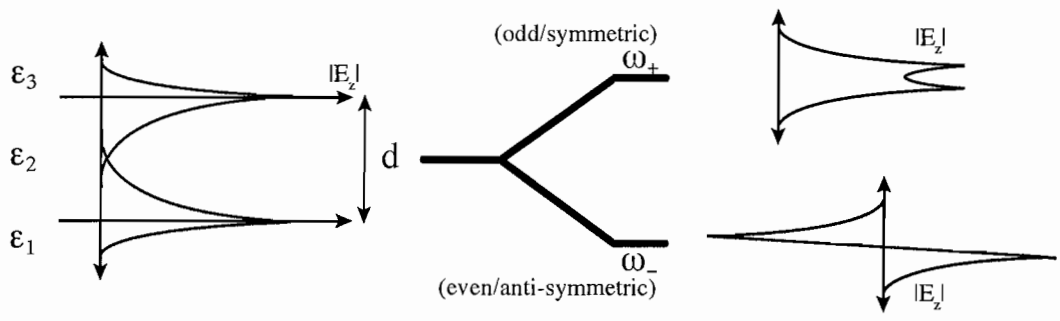

Figure 2.5. Coupling of two surfaces supporting surface plasmon excitations $\Rightarrow$ $\varepsilon_2 \propto -\varepsilon_{1,3}$. The mode splitting will exist for both dielectric slabs (MDM) or metal films (DMD) structures.

modes, an effect sometimes referred to in the literature as plasmon hybridization. As illustrated in figure 2.5, when two SPP modes are brought together the modes couple into even (anti-symmetric) and odd (symmetric) modes. As it is central to the results of chapters IV and V it is important that we examine some of the results of this coupling.

The dispersion relation for the fundamental coupled SPP modes through a thin layer of width d is given by [1, 78]:

$$e^{-2k_2 d} = \frac{k_2/\varepsilon_2 + k_1/\varepsilon_1}{k_2/\varepsilon_2 - k_1/\varepsilon_1}\frac{k_2/\varepsilon_2 + k_3/\varepsilon_3}{k_2/\varepsilon_2 - k_3/\varepsilon_3} \tag{II.8}$$

If we make the assumption of symmetric cladding layers ($k_1 = k_3$) then II.8 reduces to the following two possible solutions:

$$\tanh(k_2 d/2) = -\frac{k_1\varepsilon_2}{k_2\varepsilon_1} \quad \text{(odd)} \tag{II.9a}$$

$$\tanh(k_2 d/2) = -\frac{k_2\varepsilon_1}{k_1\varepsilon_2} \quad \text{(even)} \tag{II.9b}$$

There are several interesting results of equations (II.8) and (II.9) that apply to MDM structures. First, due to the evanescent nature of the SPP modes, the coupling of equation (II.8) is exponential in the separation distance d for either MDM or DMD configurations. We will encounter a similar condition in chapter IV when we derive the SPP coupling for core-shell MDM spheres. Second, in flat MDM systems it has been shown by Prade et al. that the lowest order odd solutions (equation (II.9a)) do not exhibit a cutoff with decreasing dielectric film thickness ($d \to 0$) [80]. This has the effect of allowing both high confinement ($\sim \lambda/(\sqrt{\varepsilon_2}10)$) and reasonable propagation lengths of $\sim 100\mu$m, as stated in chapter I. These types of interior SPP modes (ISP) will be used in chapter V to excite spectrally narrow plasmon ISP bands. We will show that we can use such ISP bands to control the angular and spectral emission of the plasmon enhanced transmission of periodic metallic surfaces.

The final result of MDM coupling in flat systems that we wish to review is the effect of SPP-SPP coupling on the dispersion relation of higher order mode solutions. Using the transfer matrix method, Shin et al. have theoretically shown that in the case of a lossless Drude metal, there is a new band of modes that have flat dispersion. For this second order band $\omega_2(k \to \infty) = \omega_{sp}$, and additionally the value of the solution in the DC limit $\omega_2(k \to 0)$ is a function of the separation distance d [81]. And thus the following condition holds:

$$\omega_2(k \to 0) = \omega_{sp} \quad \text{for} \quad d = \frac{2\pi c}{\omega_{sp}\sqrt{\varepsilon_d}} \tag{II.10}$$

Calculation of $\omega_2(k)$ shows that this second band of solutions to equation (II.9a)

is essentially flat and fixed to the line $\omega_2(k) = \omega_{sp}$. We will use this in chapter IV when analyzing the scattering properties of MDM spheres. The same condition for the thickness of a dielectric shell has been shown by my co-authors to result in a flat band in the angular dispersion of the MDM sphere [82]. In chapter IV we use this flat band to both enhance the absorption of MDM spheres, and reduce the scattering of an MDM layered sphere (through additional SPP couplings).

CHAPTER III

THEORY OF METALLODIELECTRIC MIE SCATTERING

Introduction

When a flat interface supporting a bound SPP mode is bent, that mode will lose some fraction of its energy to radiative decay. As a consequence, the SPP modes excited on spherical particles (or any shape comparable in size to λ_0) are naturally coupled to radiating far-field excitations. Hence, contrary to the flat MD interface we can excite SPP modes on small particles simply by illuminating them. In this chapter we will build up the theoretical and computational tools needed to discuss the question: When a radiating SPP on the surface of a metal sphere coherently couples to an ISP mode bound to the interior of the sphere, how is the far-field scattering effected? We will *answer* this question in the chapters that follow.

Localized SPPs on Small Spheres

We begin with the "simple" example of a plane-wave with wavevector $\vec{k} = \sqrt{\varepsilon_M} k_0 = \sqrt{\varepsilon_M} 2\pi/\lambda_0 \hat{z}$ scattering from very small ($r \ll \lambda_0$) spherical object such as in figure 3.1. In this case the phase variation of the external plane-wave across the particle

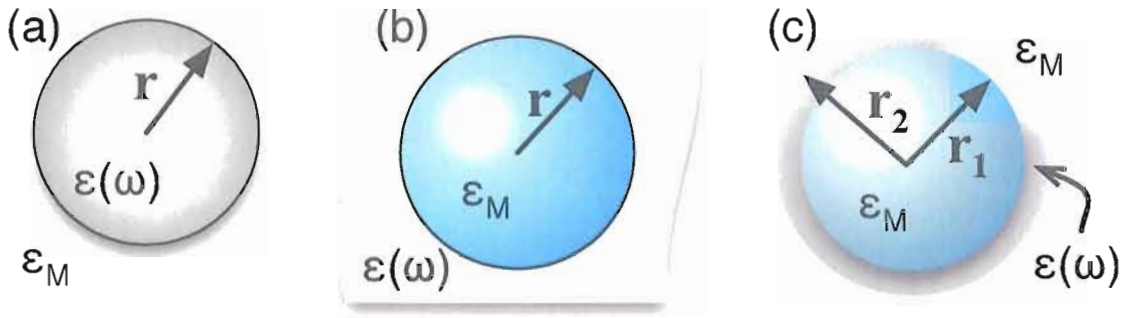

Figure 3.1. Plasmonic particle types and our abbreviated nomenclature: (a) Metal sphere, embedded in a dielectric medium (Md) (b) dielectric void (Dm) (c) one or more metal-dielectric shells (DMd, MDm, MDMd, $(MD)_x$d, etc.

is very small. Using the approximation of a spherical particle in a spatially uniform external field (the quasi-static approximation, $\vec{E}_0 = |\vec{E}_0|\hat{x}$) the particle polarizability is given by the relation [83]:

$$\alpha = 4\pi\varepsilon_M r^3 \frac{\varepsilon - \varepsilon_M}{\varepsilon + 2\varepsilon_M} \tag{III.1}$$

It follows that polarization of the sphere and the electric field in and around it are given by:

$$\vec{p} = 4\pi\varepsilon_0\varepsilon_M\alpha\vec{E}_0 \tag{III.2}$$

$$\vec{E}_{\text{interior}} = \frac{3\varepsilon_M}{\varepsilon + 2\varepsilon_M}\vec{E}_0 \tag{III.3}$$

$$\vec{E}_{\text{exterior}} = \vec{E}_0 + \frac{3\vec{n}(\vec{n}\cdot\vec{p}) - \vec{p}}{4\pi\varepsilon_0\varepsilon_M}\frac{1}{r^3} \tag{III.4}$$

For either spheres or voids we have exterior dipole near-field, and interior field reso-

nances when the dispersive dielectric function fulfills the conditions:

$$\begin{aligned} \text{sphere}: \quad & \varepsilon(\omega) = -2\varepsilon_M \\ \text{void}: \quad & \varepsilon(\omega) = -\frac{1}{2}\varepsilon_M \end{aligned} \tag{III.5}$$

These equations lead to the commonly quoted estimates for localized surface plasmon resonances when we assume a loss-less Drude $\varepsilon(\omega)$ such as we did for equation (II.5):

$$\text{LSPR}_{\text{sphere}} = \frac{\omega_p}{\sqrt{\varepsilon_\infty + 2}} \simeq \frac{\omega_p}{\sqrt{3}} \tag{III.6a}$$

$$\text{LSPR}_{\text{void}} = \frac{\omega_p}{\sqrt{\varepsilon_\infty + 1/2}} \simeq \sqrt{\frac{2}{3}}\omega_p \tag{III.6b}$$

Scattering, Absorption, and Extinction Cross-Sections

From a practical optics point of view, the quantities of interest when investigating the scattering of small particles are the efficiencies with which they scatter far-field radiation. This efficiency is measured with the particle's cross-section, a quantity related to the EM field through Beer's Law. Beer's Law describes the exponential decay of a plane-wave's intensity (I_0) as it passes through an absorbing and/or scattering medium of thickness d:

$$\frac{I}{I_0} = e^{-n\,d\,C_{ext}} \tag{III.7}$$

where n is the number density of the scattering particles, and I is the intensity after propagating through the media. The single particle extinction cross-section, C_{ext}, has units of area and is given by:

$$C_{ext} = -\ln\frac{I}{I_0} \tag{III.8}$$

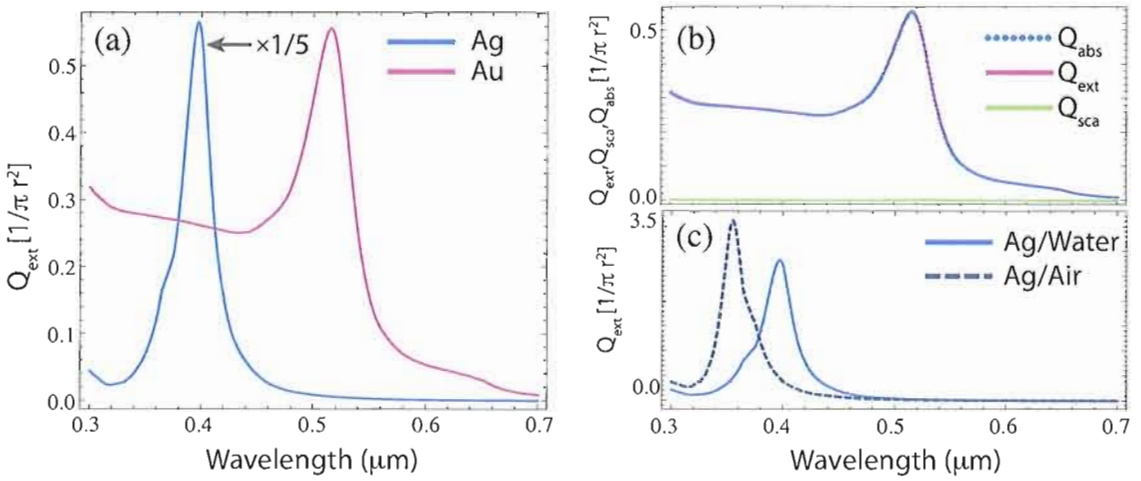

Figure 3.2. (a) Calculated extinction cross-section efficiencies of $r = 10$nm silver and gold spherical nanoparticles using tabulated dielectric functions. (b) Comparison of gold nanoparticle extinction, scattering, and absorption scattering efficiencies showing the dominate absorption of nano-scale particles. (c) Comparison of silver particle in water vs. air.

The cross-section represents the effective EM size of the particle, and extinction refers to the sum of the scattering and absorption $C_{ext} = C_{sca} + C_{abs}$. For a dispersive spherical dipole scatterer with $\varepsilon(\omega) = \varepsilon' + i\varepsilon''$ the cross-sectional areas are given by [83]:

$$C_{sca} = \frac{k_0^4}{6\pi}|\alpha|^2 = \frac{8\pi}{3}k_0^4 a^6 \left|\frac{\varepsilon - \varepsilon_M}{\varepsilon + 2\varepsilon_M}\right|^2 \tag{III.9a}$$

$$C_{abs} = k_0 \mathrm{Im}[\alpha] = 4\pi k_0 a^3 \mathrm{Im}\left[\frac{\varepsilon - \varepsilon_M}{\varepsilon + 2\varepsilon_M}\right] \tag{III.9b}$$

$$C_{ext} = 12\pi k_0 \varepsilon_M^{3/2} r^3 \frac{\varepsilon''}{[\varepsilon' + 2\varepsilon_M]^2 + (\varepsilon'')^2} \tag{III.9c}$$

We can see that in addition to the polarization and near-field electric fields, these cross-sections all have corresponding resonances associated with excitation of SPP

modes. With these small radius particles, the r^3 absorption cross-section dominates the r^6 scattering cross-section as $k \rightarrow 0$. In figure 3.2 we have plotted the extinction cross-section spectra of a 10 nm radius gold nanoparticle and a $r = 10$ nm silver nanoparticle in water and air. These plots illustrate three points: the absorption dominated character of C_{ext} for small particles, the correlation between silver's lower losses and the increased strength of the localized SPP resonance, and the sensitivity of the resonance condition on the external dielectric media.

Equation (III.9) also demonstrates that it is possible to find far-field signatures of the near-field energy distributions created by the excitation of SPP resonances. We will utilize this fact extensively in the rest of this thesis to investigate SPP modes and their coupling through far-field scattering experiments.

Mie Theory: Beyond the Quasistatic Approximation

Mie theory is the rigorous solution to the problem of scattering a plane-wave by an azimuthally isotropic spherical object. The central results are the spherical harmonic expansion coefficients for the EM fields internal and external (scattered) to the sphere. The scattered field coefficients are given by:

$$a_\ell = \frac{m^2 j_\ell(mx)\psi'_\ell(x) - \psi'_\ell(mx)j_\ell(x)}{m^2 j_\ell(mx)\xi'_\ell(x) - \psi'_\ell(mx)h_\ell(x)} \quad \text{(III.10a)}$$

$$b_\ell = \frac{j_\ell(mx)\psi'_\ell(x) - \psi'_\ell(mx)j_\ell(x)}{j_\ell(mx)\xi'_\ell(x) - \psi'_\ell(mx)h_\ell(x)} \quad \text{(III.10b)}$$

where, for a dispersive sphere in a non-dispersive media $m \equiv \sqrt{\varepsilon(\omega)}/\sqrt{\varepsilon_M}$, $x \equiv kr =$

$\sqrt{\varepsilon_M}(2\pi/\lambda_0)r$ is the so called size parameter, $\psi_\ell(x) \equiv x j_\ell(x)$, $\xi_\ell(x) \equiv x h_\ell(x)$ are the spherical Riccati-Bessel and Hankel functions of the first kind, and the prime denotes derivation with respect to the argument. A full derivation of equation (III.10) can be found in appendix A. The cross-sections for a spherical particle can be calculated in terms of the scattering coefficients [83]:

$$C_{sca} = \frac{2\pi}{k_M^2}\sum_{\ell=1}^{\infty}(2\ell+1)(|a_\ell|^2+|b_\ell|^2) \tag{III.11a}$$

$$C_{ext} = \frac{2\pi}{k_M^2}\sum_{\ell=1}^{\infty}(2\ell+1)Re[a_\ell+b_\ell] \tag{III.11b}$$

$$C_{abs} = C_{ext} - C_{sca} \tag{III.11c}$$

Equations (III.10) and (III.11) show that there are scattering and absorption resonances in the fields and in the cross-sections at the zeros of the real part of the denominators of equation (III.10). The a_ℓ fields (transverse magnetic, TM) are associated with SPP resonances, while the b_ℓ fields (transverse electric, TE) are associated with eddy currents arising from magnetic resonances. The resonance mode equations for a_ℓ and b_ℓ can be expressed as the determinants:

$$\text{TM Modes:} \quad \det[\vec{U}_{Md}] \equiv \begin{vmatrix} m^2\xi_\ell'(mx) & \psi_\ell(mx) \\ h_\ell(x) & j_\ell(x) \end{vmatrix} = 0 \tag{III.12a}$$

$$\text{TE Modes:} \quad \begin{vmatrix} \xi_\ell(x) & \psi_\ell'(mx) \\ h_\ell(x) & j_\ell(mx) \end{vmatrix} = 0 \tag{III.12b}$$

We will only concern ourselves with the TM modes for which, in the small metal sphere limit, equation (III.12a) reduces to the Frölich resonance condition stated

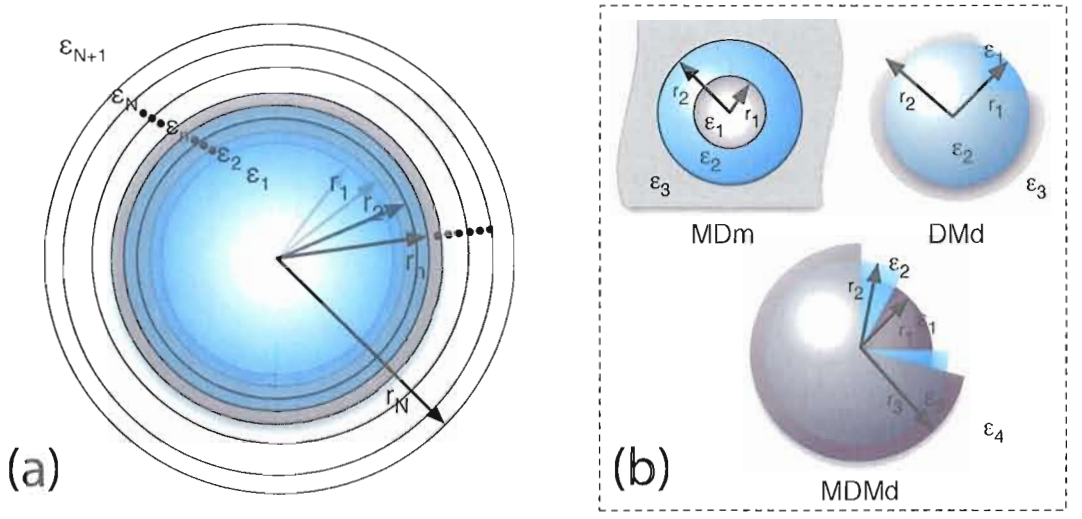

Figure 3.3. (a) Spherical scatterer with N shells each with index of refraction $\sqrt{\varepsilon_i}$ and radius r_i, embedded in a medium with index of refraction $\sqrt{\varepsilon_{N+1}}$. (b) Specific types of single and double shell particles which we will address later in this chapter.

above: $\varepsilon(\omega) = -2\varepsilon_M$. The TE modes will not influence our results. In addition to being relatively weak, they occur at frequencies above ω_{sp} for our geometries of interest such as in figure 3.3(b). Also shown in figure 3.3(b) is the nomenclature used throughout this text to specify the constituent components of a multi-shelled spherical particle. As stated above, the capitol letters denote the type of shell/core material (**M**etal or **D**ielectric) and the final, lowercase letter denotes the type of embedding medium.

SPP-SPP Coupling in MD Shells

If we wish to examine the SPP-SPP coupling between multiple spherical surfaces, we need to extend the original Mie theory results to multiple interfaces placed at the radii r_1, r_2, r_3, etc. This was done for two interfaces by Aden and Kerkker [84] and expanded to an arbitrary number of shells by Bhandari [85]. For an arbitrary number of shells, the scattered TM field coefficient, $\bar{a}_\ell^{N+1}$, can be calculated recursively through the formula (cf. appendix B):

$$\bar{a}_\ell^{N+1} = \frac{\psi_\ell(m_{N+1}x_N)}{\psi_\ell(m_{N+1}x_{N+1})}\frac{\xi_\ell(m_{N+1}x_{N+1})}{\xi_\ell(m_{N+1}x_N)}\cdot \frac{\bar{a}_\ell^N[\frac{m_{N+1}}{m_N}F_\ell(m_Nx_N) - D_\ell(m_{N+1}x_N)] - [\frac{m_{N+1}}{m_N}D_\ell(m_Nx_N) - D_\ell(m_{N+1}x_N)]}{\bar{a}_\ell^N[\frac{m_{N+1}}{m_N}F_\ell(m_Nx_N) - F_\ell(m_{N+1}x_N)] - [\frac{m_{N+1}}{m_N}D_\ell(m_Nx_N) - F_\ell(m_{N+1}x_N)]} \quad \text{(III.13)}$$

for an N shelled particle such as in figure 3.3(a). As above, $x_i = k_i r_i$ and $m_i = \sqrt{\varepsilon_i}/\sqrt{\varepsilon_{i+1}}$ is the relative index of refraction ratio. The logarithmic derivatives $F_\ell(x) = \xi'_\ell(x)/\xi_\ell(x)$ and $D_\ell(x) = \psi'_\ell(x)/\psi_\ell(x)$ are used for computational stability.

The two specific instantiations of equation (III.13) that we will concern ourselves with in this work are that of the single-layer (core-shell: MDm and DMd) and double-layer (MDMd) particles. We have placed no restrictions on the dielectric functions of equations (III.12a) and (III.13), and therefore they are valid for any combination of metal and dielectric shells. But, as we are interested in studying the coupling of SPPs, we require at least two metal interfaces. From the denominator of equation (III.13), the mode equations for the the core-shell and double-layer systems can, respectively,

be written as:

$$\det[\vec{U}_{DMd,MDm}] \equiv \begin{vmatrix} \xi'_\ell(m_3x_2) & \psi'_\ell(x_2) & \xi'_\ell(x_2) & 0 \\ h_\ell(m_3x_2) & j_\ell(x_2)\eta_2 & h_\ell(x_2)\eta_2 & 0 \\ 0 & \psi'_\ell(m_2x_1) & \xi'_\ell(m_2x_1) & \psi'_\ell(x_1) \\ 0 & j_\ell(x_1)\eta_2 & h_\ell(x_1)\eta_2 & j_\ell(x_1)\eta_1 \end{vmatrix} = 0 \qquad \text{(III.14)}$$

$$\det[\vec{U}_{MDMd}] \equiv$$

$$\begin{vmatrix} \xi'_\ell(m_4x_3) & \psi'_\ell(x_3) & \xi'_\ell(x_2) & 0 & 0 & 0 \\ h_\ell(m_4x_3) & j_\ell(x_3)\eta_3 & h_\ell(x_2)\eta_3 & 0 & 0 & 0 \\ 0 & \psi'_\ell(m_3x_2) & \xi'_\ell(m_3x_2) & \psi'_\ell(x_2) & \xi'_\ell(m_3x_2) & 0 \\ 0 & j_\ell(m_3x_2) & h_\ell(m_3x_2) & j_\ell(x_2)\eta_2 & h_\ell(m_3x_2)\eta_2 & 0 \\ 0 & 0 & 0 & \psi'_\ell(m_2x_1) & \xi'_\ell(m_2x_1) & \psi'_\ell(x_1) \\ 0 & 0 & 0 & j_\ell(m_2x_1) & h_\ell(m_2x_2) & j_\ell(x_1)\eta_1 \end{vmatrix} = 0 \qquad \text{(III.15)}$$

The physical implications of equations (III.14) and (III.15) are not immediately obvious. However we have shown (cf. appendix A) that they can be re-expressed as [46]:

$$\det[\vec{U}_{DMd}] = \begin{vmatrix} |\vec{U}_{Dm}| & |\vec{V}_{Dm}| \\ |\vec{W}_{Md}| & |\vec{U}_{Md}| \end{vmatrix} \qquad \text{(III.16)}$$

$$\det[\vec{U}_{MDm}] = \begin{vmatrix} |\vec{U}_{Md}| & |\vec{V}_{Md}| \\ |\vec{W}_{Dm}| & |\vec{U}_{Dm}| \end{vmatrix} \qquad \text{(III.17)}$$

$$\det[\vec{U}_{MDMd}] = \begin{vmatrix} |\vec{U}_{Md}| & |\vec{V}_{Md}| \\ |\vec{W}_{MDm}| & |\vec{U}_{MDm}| \end{vmatrix} \tag{III.18}$$

The equations for the coupling matrices, $\vec{V}_{Dm}$, and $\vec{W}_{MDm}$, are given in appendix A. $\vec{V}_{Md}$ will be discussed below. The equations (III.17) and (III.18) demonstrate that the coupling between spherical shells in an arbitrary MD system can be broken down into the couplings between their more "basic" elements. This has proven to be a useful tool for the theoretical study of the couplings between spherical MD modes. This technique has been proposed in the case of small ($r \ll \lambda_0$) MD particles and is referred to as plasmon hybridization [76]. But, to our knowledge, this is the first time the technique has been extended to arbitrarily large particles, or multishell particles.

For the specific example of the MDMd particle, an important result of equation (III.18) is the expansion of the coupling matrix $\vec{V}_{Md}$:

$$\det[\vec{V}_{Md}] = \begin{vmatrix} \xi'_\ell(m_{N+1}x_N) & \xi'_\ell(x_N) \\ h_\ell(m_{N+1}x_N) & h_\ell(x_N) \end{vmatrix} \tag{III.19}$$

In this case $x_1 = k_1 r_1 = \sqrt{\varepsilon_m} k_0 r_1$, $x_2 = k_2 r_2 = \sqrt{\varepsilon_d} k_0 r_2$, $x_3 = k_3 r_3 = \sqrt{\varepsilon_m} k_0 r_3$, $k_4 = \sqrt{\varepsilon_M} k_0$, and $k_0 = 2\pi/\lambda_0$, representing dielectric (ε_d) and metal (ε_m) and medium (M) components. By keeping r_1 and r_2 constant (and hence the keeping the second off diagonal element of equation (III.18), $|\vec{W}_{MDm}|$, constant) we can examine the effect of scaling the thickness of the outer shell, $|r_3 - r_2|$, by looking at the effect of scaling r_3 on $|\vec{V}_{Md}|$. In the limit of $x_3 \gg \ell^2$ the mode coupling may be expressed using the

asymptotic expansion of the Hankel function, $h_\ell(x) \sim (-i)^{\ell+1} e^{ix}/x$. This shows that the plasmon coupling between the inner sphere and outer shell decays exponentially with metal shell thickness $|r_3 - r_2|$:

$$|\mathbf{V_{Md}}| \sim \left[(-1)^\ell \left(\frac{\sqrt{\epsilon_3} - 1}{k_4 r_3}\right) e^{i(k_4 + k_3')r_3 + \pi/2}\right] e^{-k_3'' r_3} \tag{III.20}$$

where $k_3 \equiv k_3' + ik_3''$. We see, that similarly to the result of the coupling in flat MDM systems reviewed in chapter II, the coupling in spherical systems scales exponentially with thickness of the metal layer. This same analysis applies to equation (III.17) for $|\vec{U}_{MDm}|$. Because the form of $|\vec{V}_{Md}|$ has the same functional form as $|\vec{V}_{MDm}|$ we can conclude that coupling between spherical metal surfaces through dielectric shells has the same exponential coupling dependence on shell thickness.

In addition to studying their properties analytically, we can use equations (III.17) and (III.18) to compute the angular mode bands (angular momentum dispersion relation) for multilayered spherical MD systems on a element by element basis. Thus, we can use these equations to study the mode coupling between SPP bands as the model parameters (radii and dielectric functions) are systematically varied. Combined with equation (III.13) we can correlate SPP-SPP coupling with the induced far-field scattering effects on absorption, scattering, and extinction. This will be done in the next chapter for the special case of an MDMd silver and titania sphere.

Discrete Computation of Field Coefficients

The effects of the resonant SPP modes defined by equations (III.17) and (III.18) on the particles far-field scattering can be calculated through the extinction, scattering and absorption cross-section formula (III.11). By calculating the outward propagating and inward propagating field coefficients ($\bar{a}_\ell^n$, $\bar{b}_\ell^n$, $\bar{c}_\ell^n$, and $\bar{d}_\ell^n$, defined fully in appendices A and B) we have completely solved the EM scattering problem. However, the discrete computation can be unstable if not approached carefully. It is therefore worthwhile to briefly mention the steps we have taken to advance the available computational tools for calculating the field coefficients and spherical Riccati-Bessel functions.

Many authors have published work on the computation of scattering from spheroidal particles that are arbitrarily large, absorbing, multi-shelled, *or* have absorbing shells. However, we found that there were no publicly available computational libraries for calculating the field coefficients and the full EM fields for a large ($r \gg \lambda_0$), multishell, absorbing particle. We have therefore brought together the work of several authors [86–90] to create our own C++ library for these computations.

The main stability issue in this computation is the divergence of Riccati-Hankel functions for large, complex arguments and large mode number ℓ. Algorithms for the discrete computation of the family of Bessel functions are based upon recursion schemes of the form [91]:

$$C_{n+1}(x) = \frac{n}{x} C_n(x) - C_n'(x) \tag{III.21}$$

for any of $j_n(x), y_n(x), h_n^{(1)}(x), h_n^{(2)}(x)$. These recursions have the computational flaw that when the Bessel function is in an exponential domain and the argument is complex, the error that propagates with successive iteration grows exponentially. Because metal dielectric functions in the visible/NIR range are intrinsically both large and complex, and the particle sizes we wish to examine have $r \sim \lambda_0$, we immediately encounter convergence issues. To ensure the proper convergence we follow the below steps in our algorithm. [1]

1. Utilize the logarithmic derivative formulation of the spherical harmonic expansion coefficients ($\bar{a}_\ell^n$, etc.) set out by Toon and Akerman [86] and Kaiser and Schweiger [90].

2. Use the method of Cachorro and Salcedo [88] to accurately estimate the needed number of expansion terms ($\ell = L_{max}$) in the expansion of the field coefficients.

3. Restrict the calculation to only non-absorbing embedding media ($\mathrm{Im}[\varepsilon_{N+1}] = 0$). This eliminates the inherent instability in calculating the ratio $\psi_\ell(x)/\xi_\ell(x)$ for complex arguments [87].

To test the convergence and accuracy of our algorithm we have compared it to several published results. These comparisons validate the work against the available parameter ranges: absorbing small particles, large dielectric particles, and large absorbing single shells. In figure 3.4 we can see the comparison with Yang [87] for the

[1] For full details of the computation the interested reader is referred to the source code documentation available from http://mo.uoregon.edu/.

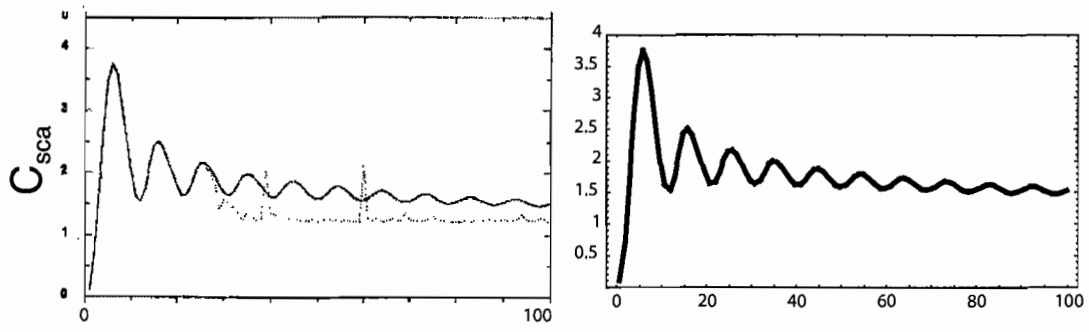

Figure 3.4. The scattering cross-section efficiency as a function of size parameter for an absorbing soot covered water droplet. (Left) Results of W. Yang [87]. (Right) Computation of Q_{sca} using our algorithm.

scattering efficiency ($C_{sca}/(\pi r^2)$) of an absorbing soot shell on a water droplet as a function of size parameter. This confirms that large particles with complex ε be safely computed for size parameters $\gtrsim 100$.

To check the accuracy of our calculation of the complete EM field, figures 3.5(a-b) and 3.5(c-d) show the near-field intensity plots of a large dielectric sphere in comparison with Lecler [89], and of a small silver sphere in comparison with Wang et al. [92]. We see that in both size regimes, the scattered (external) and internal fields are accurately reproduced. With the validity of our computational approach confirmed we now move on, in the next chapter, to investigate the coupling of SPPs between multiple MD shells in micron-scale particles.

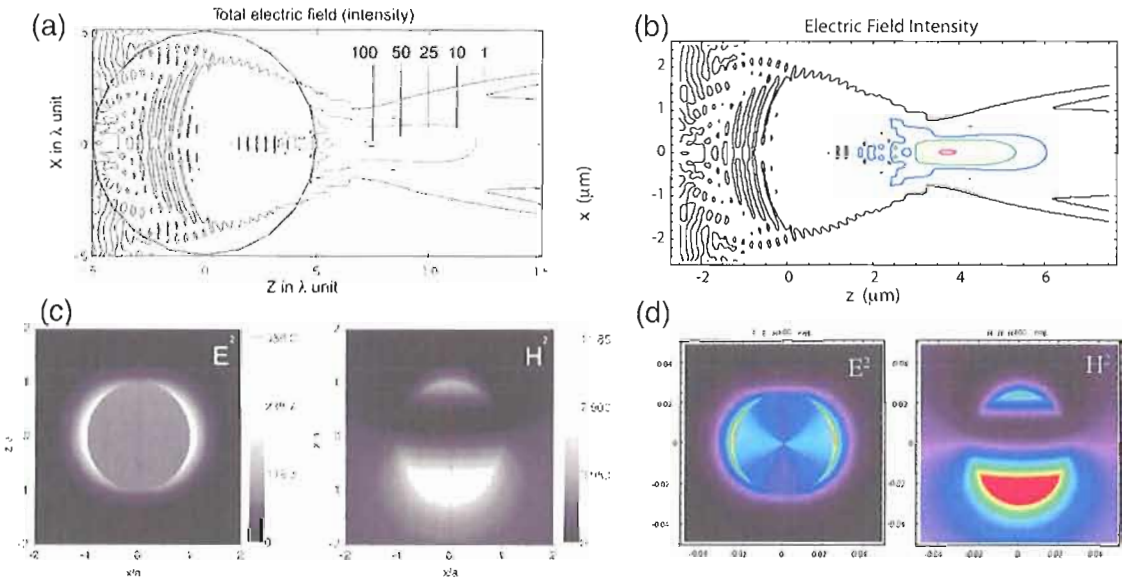

Figure 3.5. Comparison of EM field algorithm. (a) E-field intensity from Lecler et al. [89] compared with (b) our computation for a large silica sphere. (c) E and H field intensities from Wang et al. [92] compared with (d) for a small metal sphere with $\varepsilon = -2 + 0.2i$.

CHAPTER IV

PLASMON COUPLING IN MDM SPHERES

Introduction

Nanostructured metallodielectric materials have been extensively studied in recent years due to their promise for new photonic device applications. As discussed in the pervious chapter, and in chapter I, metallodielectrics patterned periodically in three dimensions (3D) exhibit novel dispersion characteristics which rely on coherent coupling of SPPs [15, 93, 94], potentially allowing sub-wavelength manipulation of light signals. An important geometry extensively addressed in the literature, is that of the nanoscale 3D spherical plasmonic resonator. Previously noted as the dipole approximated DMd geometry, it consists of a metal nanoshell surrounding a nanoscale dielectric core, and may be designed to allow tuning of the SPP field distribution as well as its *absorption* resonance [95]. The large plasmon fields in these systems have proven useful for surface-enhanced Raman spectroscopy [96], and the tunability in the resonance has been successfully used in a variety of applications including cancer therapy and photo-induced drug delivery [17, 76].

In this chapter we apply the formalism of chapter III to extend these investigations to large ($r \simeq \lambda_0$), multilayer particles. Specifically, we analyze the greatly reduced

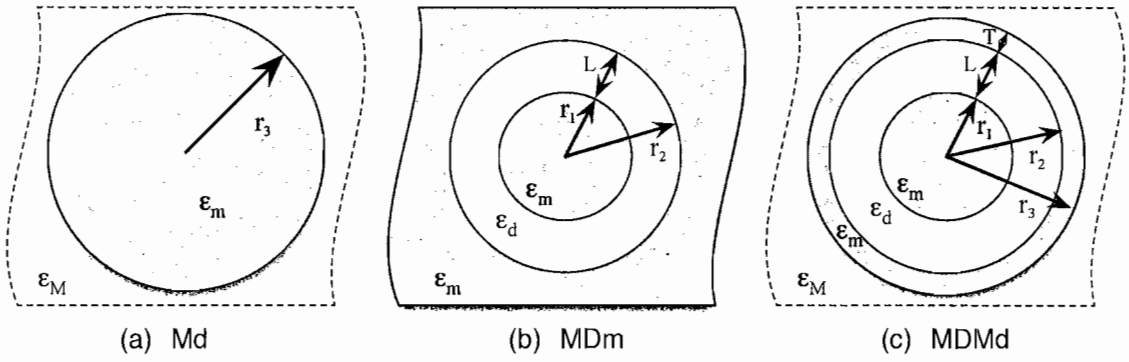

Figure 4.1. Examples of the geometry and composition of the metal and dielectric (Md, MDm and MDMd) resonators studied in this chapter.

scattering cross sections of micron-scale MDMd particles with nano-scale coatings, such as shown in figure 4.1 and show that we can tune *both* the absorption *and* scattering properties of the plasmonic particle. The use of plasmonic coatings to reduce dipole scattering from small spheres has been investigated previously by Alŭ and Engehta [97]. Here we use the two-band coupling formalism of equation (III.18) to show that similar EM transparencies may be achieved in spheres of *any size.*

MDMd Particle Band Structure

Our system consists of a micron-size metal sphere of permittivity ε_m and radius r_1 surrounded by concentric sequences of dielectric (permittivity ε_d) and metal (ε_m) shells. The shells have thicknesses L ($|r_2 - r_1|$) and T ($|r_3 - r_2|$), respectively. The composite particle is either embedded in an isotropic and homogeneous dielectric host with permittivity ε_M or it is a cavity embedded in an infinite metallic medium with

permittivity ε_m. We show that with proper design of the metal-dielectric shells it is possible to engineer the dispersion characteristics of a MDMd resonator such that the forward scattering cross section is strongly suppressed. This results in a tunable transparency of the particles scattering cross-section. By solving the eigenvalue problem set forth in equation (III.18) we show that the observed transparency is associated with an avoided-crossing of the dominant plasmonic bands of the Md and MDm sub-elements.

Weakly Coupled Flat Dispersion

In work closely related to that which is detailed here, my co-researcher K. Hasegawa has shown that concentric metal-dielectric shells surrounding a meso-scale *metal* sphere (MDMd resonator) allow as much as an order of magnitude enhancement of the particle's absorption cross section, while maintaining the broad tunability of the composite particle SPR [82]. This results from the formation of a flat band in the angular mode dispersion of MDm cavities. In figure 4.2(a) we plot the mode diagram of an MDm cavity computed with equation (III.17). The black bands represent the zeros of equation(III.17) and show the flat band near $\omega = 0.3\omega_{sp}$. As will be shown below, this flat band is confined to the dielectric gap of the MDm cavity. We therefore refer to it as an interior surface plasmon (ISP) mode. In figure 4.2(b,c) we plot the absorption cross-section of an MDMd particle constructed through the truncation of the infinite metal medium of the MDm cavity. The cross-section calculation shows that this flat band can result in the simultaneous excitation of multiple absorption

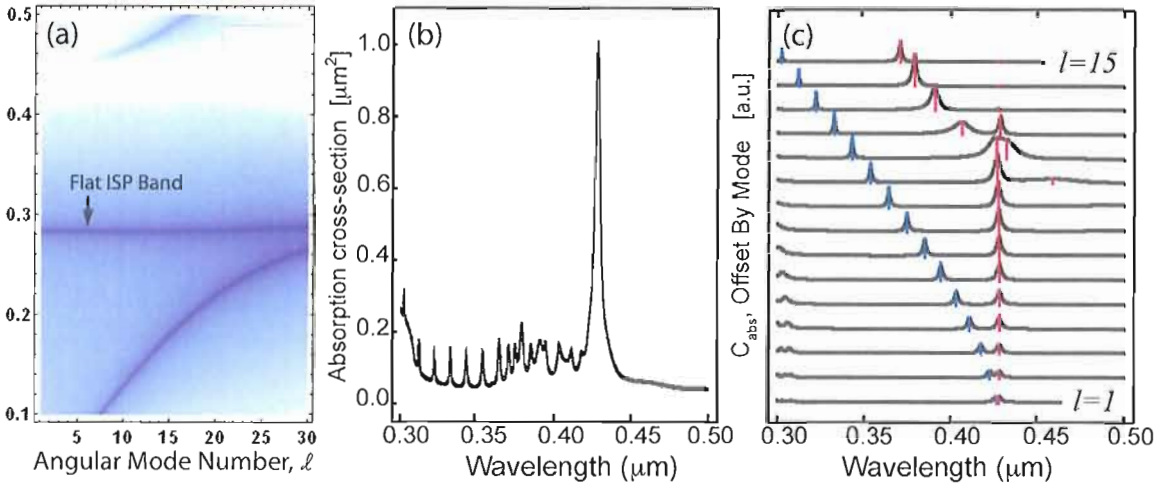

Figure 4.2. (a) TM mode, angular dispersion for a Drude-silver/titania MDm with $r_1 = 500\,\text{nm}$ and $L = L^{\star}$(b) Total absorption cross-section of a geometrically optimized MDMd particle created from titania and silver shells. (c) Individual angular mode (ℓ) absorption cross-sections showing the simultaneous excitation of ~ 12 modes (red hashes). Reproduced with permission from [82].

multipoles at a single incident frequency. This concurrent excitation is predicated upon the minimal distortion of the flat ISP band induced by the ISP coupling to the radiating exterior surface plasmons (ESP) on the outer metal shell. We therefore say that optimized absorption enhancement occurs in the "weak" ISP-ESP coupling regime. When the outer shell thickness is sufficiently large, significant coupling (and significant ISP distortion) is avoided. The threshold for the delineation between the weak and strong coupling regimes can be characterized by the skin depth (δ) of the outer metal shell ($\delta \sim 25\,\text{nm}$ for silver in the visible region).

The calculation of the needed geometry to produce a flat ISP band can be obtained by the expansion of equation (III.17). In the high multipole limit ($\ell \gg k_m x_2$) the

Riccati-Bessel/Hankel functions can be asymptotically expanded [91] and one finds the resonance condition of a planar SPP defined by equation (II.5):

$$\varepsilon_m(\omega_{sp}) + \varepsilon_d = 0$$

While for the dipole mode ($\ell = 1$) the expansion of equation (III.17) yields the condition [82]:

$$(2n-1)\pi = 2k_d L \tag{IV.1}$$

where we label the multiple roots of equation (III.17) with a band index $n \geq 0$. This places a geometric condition (the width of the dielectric shell L) on the frequency of the SPP dipole resonance for $n \geq 1$. By enforcing that both equations (II.5) and (IV.1) be fulfilled for the $n = 1$ band we obtain the needed dielectric shell width for a flat dispersion band:

$$L \approx \lambda_{sp}/4\sqrt{\varepsilon_d}, \quad \text{where} \lambda_{sp} = 2\pi c/\omega_{sp} \tag{IV.2}$$

Strongly Coupled ISP-ESP Dispersion

We will now use the existence of this flat band to create a *transparency* in similarly designed particles by strongly coupling the additional ESP modes to the flat MDm dispersion band. As will be shown in detail below, this can be accomplished through reducing the outer shell thickness below the skin depth ($T < \delta$).

Using the eigenmode equations described in chapter III we obtain the eigenfrequencies of the three systems shown in figure 4.1: an Md geometry with metal sphere

of radius $r_3 = 582\,\text{nm}$ embedded in a nonabsorbing dielectric host, an infinite MDm with metal core radius $r_1 = 500\,\text{nm}$ and dielectric shell with width $L = 54\,\text{nm}$, and an MDMd with the same r_1, r_2 as the infinite MDm and total radius (r_3) of the Md sphere (an outer metal shell of thickness $T = 28\,\text{nm}$). The embedding dielectric of both the metal sphere and MDMd is vacuum ($\varepsilon_M = 1$). The thickness of the dielectric shell follows from the near-resonance condition for flat dispersion, equation (IV.2). In particular, we chose a silver-like Drude metal such as described in chapter II, with $\varepsilon_m(\omega) = \varepsilon_\infty - \omega_p^2(\omega^2 + i\gamma\omega)^{-1}$ and $\varepsilon_\infty = 5.1$, $\hbar\omega_p = 9.1\,\text{eV}$, and $\hbar\gamma = 0.021\,\text{eV}$. The dielectric shell is weakly-dispersive amorphous titania ($\varepsilon_d \approx 5.76$) [98]. The choice of high-index dielectric shell ensures large separation between ω_p and ω_{sp}, an important result for resolving the effects discussed below.

In figure 4.3(b) we plot the eigenfrequencies for the TM modes of the three geometries described above as well as two other MDMd particles with different outer shell thickness (7nm and 70nm). The dashed line labeled ESP denotes the first band ($n = 0$) of eigenfrequencies of the solid metal sphere obtained from equation (III.12). The horizontal dashed line labeled ISP denotes the second band modes ($n = 1$) of the infinite MDm (equation (III.17)). This flat band is obtained at the expected frequency [82] $\omega_{sp}/\omega_p = (\varepsilon_\infty + \varepsilon_d)^{-1/2} \approx 0.3$. The first three bands of solutions to equation (III.18) describing the MDMd microsphere are also plotted, and denoted by the filled red circles. These bands correspond to the $n = 0$, $n = 1$, and $n = 2$ solutions. The $n = 0$ band of the MDMd (the lowest frequency band shown) is at

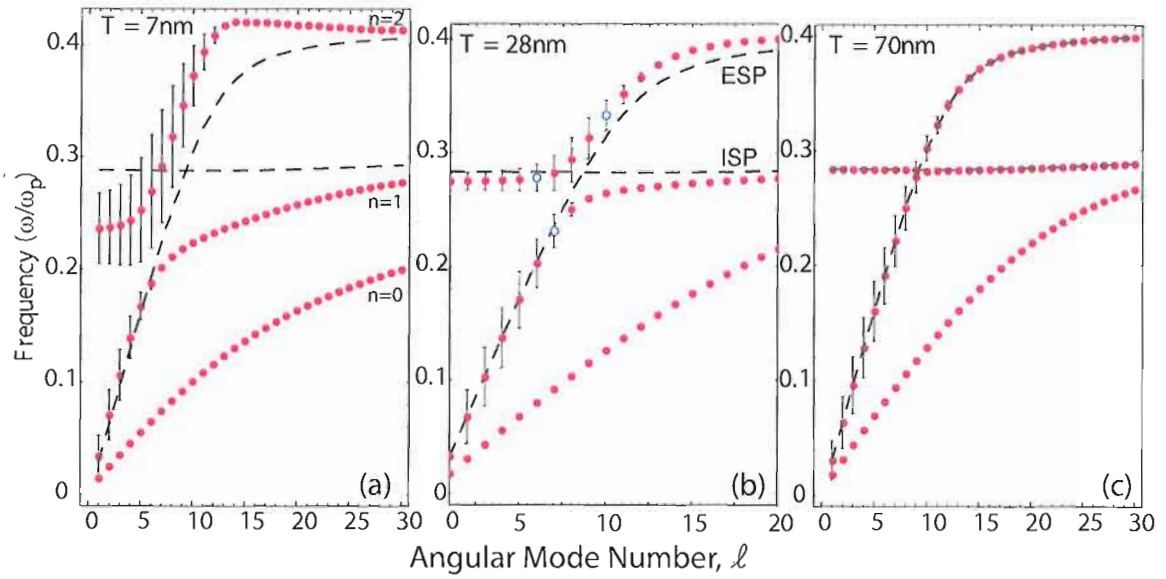

Figure 4.3. Angular mode dispersions of $(MD)_x$ microspheres. The MDMd spheres differ in their outer shell thicknesses (a) $T = 7\,\text{nm}$, (b) $T = 28\,\text{nm}$, and (c) $T = 70\,\text{nm}$. Also plotted are bands of Md ($n = 0$) and MDm ($n = 1$) particles respectively labeled as ISP and ESP. The mode distributions at the locations denoted by the open, blue circles will be discussed further below. Their mode energy distributions will be used to define interior and exterior plasmon modes.

significantly lower frequencies with respect to the other bands, and hence does not couple to the higher order solutions. Because these are radiating SPPs the eigenfrequencies are complex numbers. The width of each resonance is given by a vertical bar, equal in magnitude to twice the imaginary part of the eigenvalue, and the central frequency, marked by the red data points, denotes its real part. The TE modes are all of frequencies greater than $\omega/\omega_p = 0.4$ and are therefore not plotted here. A well-resolved avoided-crossing is observed at $\omega/\omega_p = 0.284$, a result of coherent coupling between the solid metal sphere and the infinite MDm.

Figures 4.4(a)-(c) show grayscale plots of the time averaged near-field energy den-

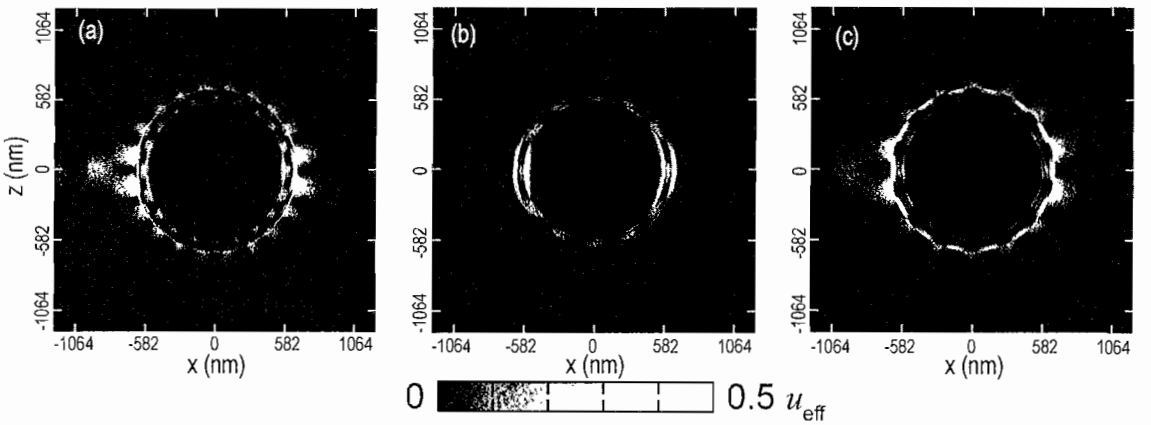

Figure 4.4. Near-field energy density plots for the modes indicated by the open blue circles in figure 4.3, at (a) ($\omega/\omega_p = 0.336$, $\ell = 10$), (b) ($\omega/\omega_p = 0.294$, $\ell = 6$) and (c) ($\omega/\omega_p = 0.233$, $\ell = 7$).

sities corresponding to the three different frequencies in figure 4.3(b) denoted with open blue circles. The time averaged near-field energy density for a time-harmonic field in the presence of an absorbing medium with permitivity $\varepsilon = \varepsilon' + i\varepsilon''$, is given by [99]:

$$u_{\text{eff}} = \frac{\varepsilon_0}{4}\left(\varepsilon' + \frac{2\omega\varepsilon''}{\gamma}\right)|\vec{E}|^2$$

In figures 4.4(a) and 4.4(c) we observe that the near-field energies of the low and high frequency modes are concentrated at the outer metal shells, forming the *external surface plasmon* (ESP) modes noted above. For an intermediate frequency value, close to $\omega/\omega_p = 0.284$ figure 4.4(b) shows the field energy is concentrated at the interior shells' interfaces, thus belonging to an *inner surface plasmon* (ISP) branch. The ISP modes are the spherical analogs to the planar gap plasmons discussed in chapters I and II. These ESP and ISP branches coincide with the uncoupled solutions

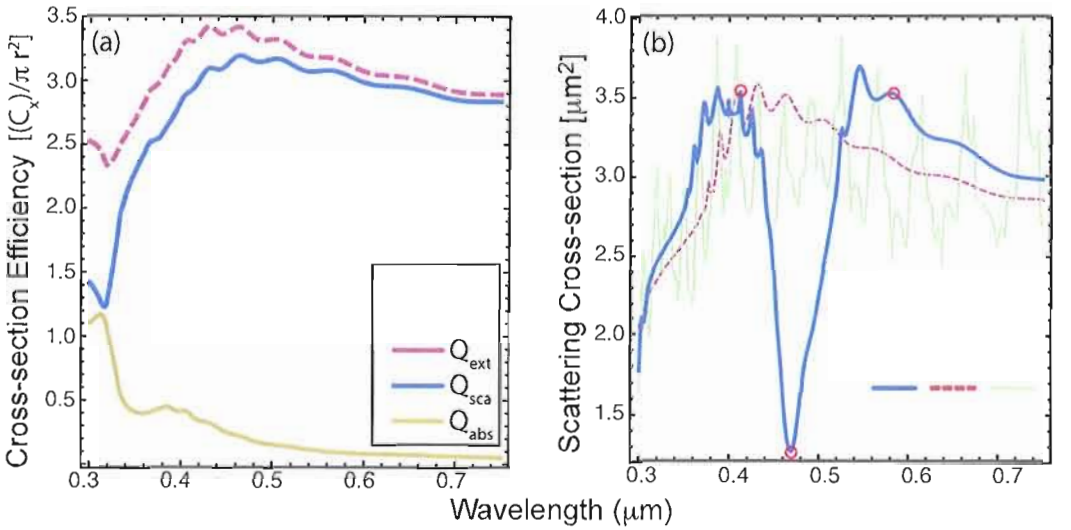

Figure 4.5. (a) (Ext)inction, (sca)ttering and (abs)orption cross-section efficiencies for a solid metal sphere with $r_3 = 584\,\text{nm}$. (b) Scattering cross-section for a MDMd plasmonic particle as compared to two other constituent geometries (Md and DMd) described in the text. The figures in the plot legend are drawn to scale.

to the solid metal sphere and infinite MDm, respectively, accurately depicting the EM energy distributions in these systems. As we show below, suppression of the ESP in favor of excitation of the ISP results in a dramatic reduction of the MDMd forward–scattering cross section.

Plasmon Induced Transparency

In figure 4.5(a) we plot the scattering cross-section of the large metal sphere of figure 4.1(a). (As calculated with equations (III.11) and (III.13).) As can be seen, the extinction cross-sections of the large metal sphere is dominated by its scattering. Recall that absorption dominated the EM interactions of small particles, and that

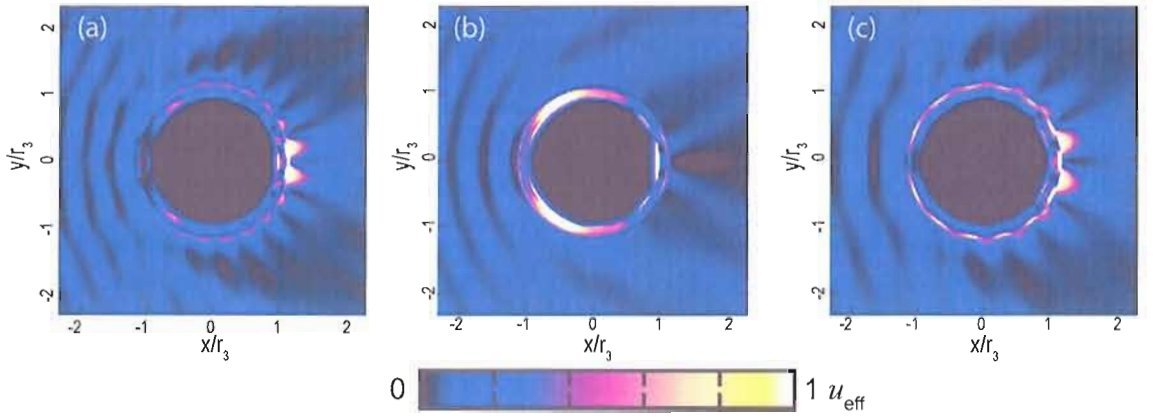

Figure 4.6. Total near-field energy densities for $\lambda_0 =$ (c) 407 nm ($\omega/\omega_p = 0.336$), (b) 463 nm ($\omega/\omega_p = 0.294$), (c) 586 nm ($\omega/\omega_p = 0.233$). All incident fields are described by plane-waves with k-vector $k = 2\pi/\lambda_0$ impinging from the left.

plasmon hybridization primarily resulted in the alteration of these *absorption* characteristics. In figure 4.5(b) we plot the scattering cross section, C_{sca}, for the MDMd described above. For comparison we also plot C_{sca} of the solid metal sphere in figure 4.5(a) and the scattering cross-section of a DMd particle. The latter consists of a titania sphere surrounded by a Drude-silver shell, and embedded in a vacuum [82, 95]. (It is not possible to compute C_{sca} for the infinite MDm since it does not support outward propagating solutions.) A large dip in C_{sca} is observed at a wavelength of $\lambda = 463$ nm, corresponding to strong suppression of the forward–scattered fields.

Energy densities of the scattered fields are shown in in figures 4.6(a)-(c), corresponding to the circled wavelength values in figure 4.5(b). As expected, in figure 4.6(b) we observe strong suppression of the scattered field at $\lambda = 463$ nm ($\omega/\omega_p = 0.294$) and the ISP nature of the fields is apparent. This suppression is reminiscent

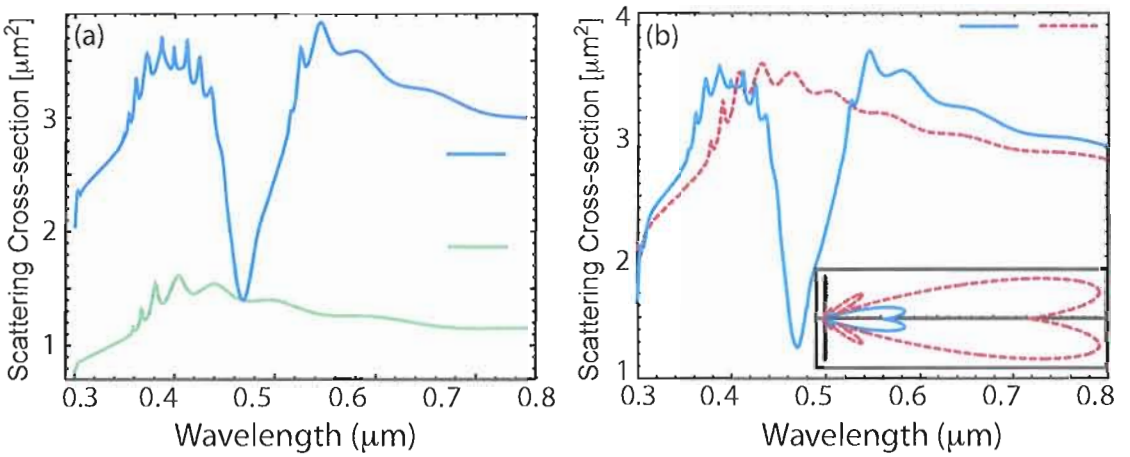

Figure 4.7. (a) Comparison of the scattering cross-sections of a MDMd particle and a Md sphere with equivalent scattering area at 463 nm. (b) Comparison of the angle resolved scattering (inset) between a MDMd particle and a solid Md sphere with the same total radius.

of coupled-resonator electromagnetically induced transparency (EIT) [100]. Here too we see a transparency associated with large group delay, though in the MDMd it is *azimuthal*. Excitation of the ISP also suggests that EIT-like dynamical damping is responsible for the transparency. At higher and lower energies, where ESP excitations prevail, the forward-scattered fields are significant, as seen in figures 4.6(a) and 4.6(c).

The effective scattering cross section at $\lambda = 463\,\text{nm}$ is equivalent to that of a silver sphere with $r_3 = 360\,\text{nm}$. Thus, adding one dielectric-metal nanoshell sequence onto a $1\,\mu\text{m}$ diameter silver sphere reduces its EM footprint to that of a significantly smaller particle. This is illustrated in figure 4.7(a), where we have plotted the scattering cross-section of a Drude-silver sphere with a radius of 360 nm. In figure 4.7(b) we

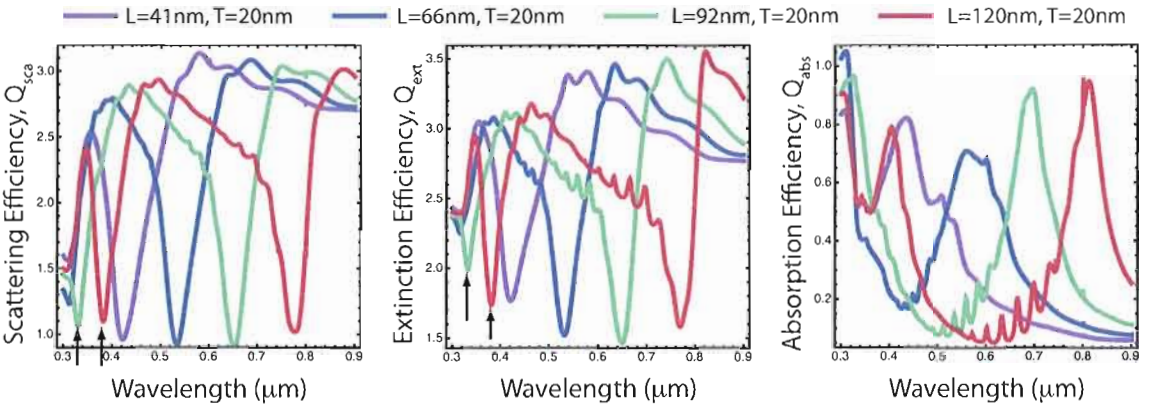

Figure 4.8. Tuning the (a) scattering, and (b) extinction transparency window with dielectric shell width, L. Second order transparencies indicated with black arrows. (c) Tuning of absorption resonance accompanying the change of L.

show the angle resolved scattering of the MDMd sphere in comparison with the solid $r_3 = 584\,\text{nm}$ sphere. This shows that the scattering of the MDMd sphere is reduced in all directions.

We further find that the scattering transparency may be tuned by adjusting the thickness of the dielectric shell. This is illustrated in figure 4.8(a), where we plot the scattering efficiency ($Q_{sca} \equiv C_{sca}/\pi r_3^2$) for several values of L. We use experimentally tabulated values for silver [82] and amorphous titania [98] to model a $r_1 = 500\,\text{nm}$ silver core with a metal shell of fixed thickness $T = 20\,\text{nm}$. By varying the dielectric shell thickness, L the transparency is tuned across the entire visible spectrum. Figure 4.8(a) also shows the second–order transparency window of these spheres, arising from mode coupling in higher bands.

We note that the significant quantity typically measured in the far-field is the extinction cross-section, describing the total energy removed from an incident plane

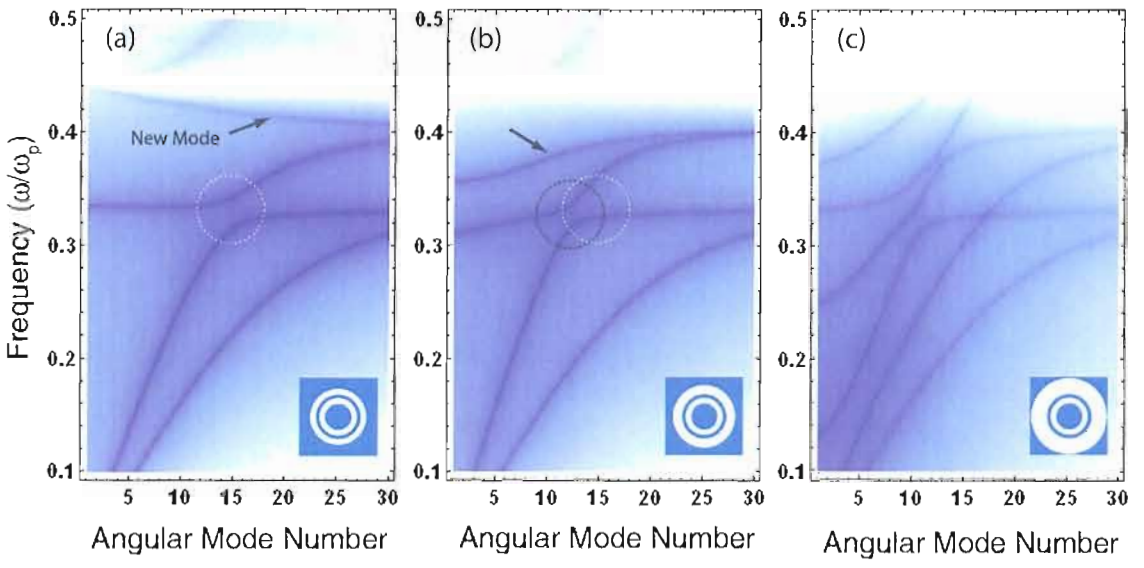

Figure 4.9. Dispersion diagrams for several MDMDm silver/titania plasmonic cavities. The dark lines form the solutions to the eigenmode equation extended from equation (III.18). For each diagram $r_1 = 500\,\text{nm}$, $L_1 = 54\,\text{nm}$, $T_1 = 20\,\text{nm}$, and (a) $L_2 = 135\,\text{nm}$, (b) $L_2 = 100\,\text{nm}$, (c) $L_2 = 500\,\text{nm}$.

wave due to scattering *and* absorption [83]. For the MDMd discussed here we have verified that the absorption peak is always offset in frequency from the transparency window. This is shown in figure 4.8(c), where we plot the absorption cross-section for the same geometric parameters as plotted in figure 4.8(a) and (b). Thus, as shown in figure 4.8(b) our calculated scattering minima also result in true extinction transparencies in the composite particle's far-field scattering.

Multiple Shells: M(DM)_x

Both our analytical formalism and our computational approach are extendable to

the addition of more than just a single DM shell. In this section we examine the effect of additional shells on the $M(DM)_x$ mode structure and far-field scattering cross-section spectra. The addition of more shells to the original MDM allows for the coupling of new mode bands associated with the new DM interfaces. This is shown in figure 4.9 where we have plotted the angular mode dispersion diagrams of several MDMDm structures. They are formed from the same material components as above (titania and silver) and have the same r_1, r_2 and r_3. The additional dielectric layer has a varied thickness of 50 nm, 100 nm, and 500 nm. The use of a metal embedding medium means that eigenfrequencies real numbers and directly plottable with Mathematica via the extended determinates based on equation (III.18). The use of a metal embedding medium also focuses attention on the coupling between the allowed modes of the dielectric gaps without introducing additional complications from coupling to radiating ESP modes present in a MDMDMd particle. It is obvious from figure 4.9(a) that a new mode has been generated with the addition of the new DM layer. As the outermost dielectric shell increases in width we see that additional modes are allowed, and begin to couple to the exiting MDM modes. Thus they serve to further alter the original MDM anti-crossing central frequency and width. This further strengthens our analogy between our spherical flat band mode and the flat band mode found in planar systems. Dionne et al. have shown that below a critical dielectric gap width all modes (except a single symmetric SPP mode) are cut off and

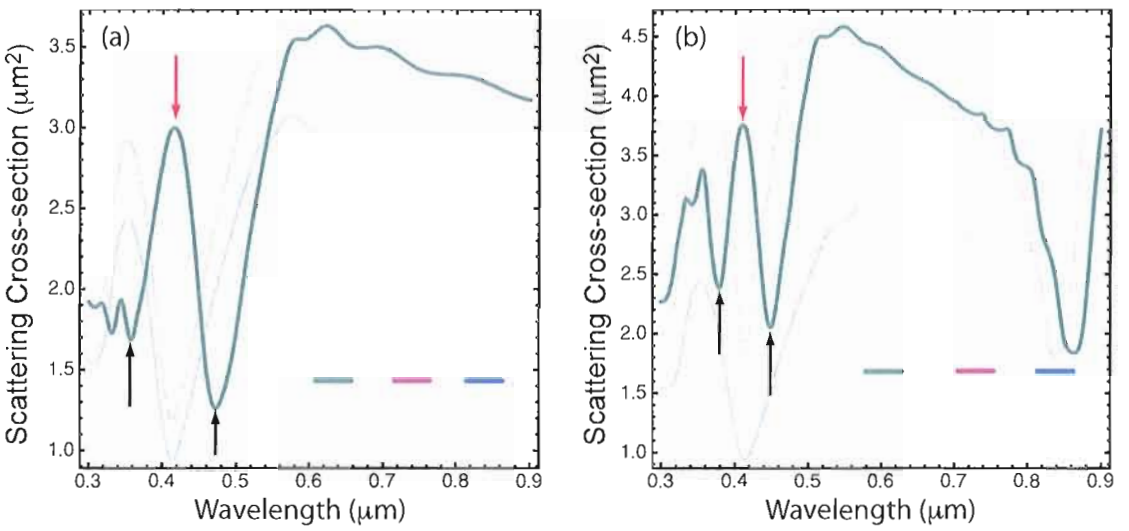

Figure 4.10. Scattering cross-sections of multilayered MDMDMd particles. (a) Overlap of two forward scattering transparencies from a double DM shell. (b) Overlap of the first order and second order scattering transparencies from an asymmetric double DM layered particle. Black arrows indicate the created split transparency windows, and red arrows indicate the destructive interference of the original particles' level coupled resonator induced transparency.

excluded from propagation along the planar SPP waveguide [23]. Here too, we see the same behavior for the flat band found in $M(DM)_x$ systems.

In figure 4.10 we plot the scattering cross-sections of two MDMDMd particles. These indicate a possible result of the additional shell plasmon mode coupling on a plasmonic multishell particles far-field scattering. In figure 4.10(a) we have plotted the scattering cross-section of a double shell $M(DM)_2d$ particle. It has the same titania/silver composition as above with the same core radius, $r_1 = 500\,\text{nm}$. The shell thicknesses are given as $L_1 = 39\,\text{nm}, T_1 = 20\,\text{nm}, L_2 = 39\,\text{nm}, T_2 = 20\,\text{nm}$. The overlap of the two resonant splitting transparencies has lead to an additional level

splitting of the original avoided-crossing in the band structure of the MDMd particle. This results in a destructive interference effect of the ISP-ESP coupling at the original anti-crossing wavelength (414 nm). The result is the emergence of a scattering peak with two transparency regions to either side. In figure 4.10(b) we show the the same resonance level splitting by overlapping a first order transparency formed in a $r_1 = 500\,\text{nm}$, $L_1 = 39\,\text{nm}$, $T_1 = 20\,\text{nm}$ MDMd with the second order transparency formed in a $r_1 = 500\,\text{nm}$, $L_1 = 135\,\text{nm}$, $T_1 = 20\,\text{nm}$ MDMd particle through the construction of a $r_1 = 500\,\text{nm}$, $L_1 = 39\,\text{nm}$, $T_1 = 20\,\text{nm}$, $L_2 = 135\,\text{nm}$, $T_2 = 20\,\text{nm}$ MDMDMd particle.

Conclusions

In summary, we have shown that coupling of interior and exterior surface plasmon modes in MDM microspheres leads to resonant level splitting. This can result in the strong suppression of the forward–scattering cross section, to values as small as the geometric cross section of the particle. It can also result in an enhanced particle absorption cross-section. We have shown that the important quantity delineating between the optimization of the two phenomena is the strength of the ISP-EPS coupling. This coupling strength is governed by the width of the outer metal shell and characterized by the skin depth of the constituent metal. Additionally, these transparency and absorption properties are spectrally tunable via the dielectric shell parameters. Finally, we have also shown results of extending the formalism developed in chapter III

to additional DM shells, can create new scattering properties through the coherent coupling of additional angular SPP bands. In short, subwavelength metal-dielectric coatings may be utilized to significantly alter the EM footprint of *large*, non-planar metallic objects and to tune their absorption and scattering properties.

CHAPTER V

FINITE ELEMENT ANALYSIS OF PERIODIC MDM SURFACES

Introduction

In this chapter we demonstrate the tailoring of SPP dispersion bands through the manipulation of the geometric parameters of a large amplitude grating formed from the hemi-cylindrical modulation of an MDM film. The geometry of our periodic plasmonic structure is shown in figure 5.1. It consists of an array of silica rods of diameter a, coated with a silver-silica-silver conformal coating. The layers are characterized by their material composition and thicknesses (S, L and T). Using the finite element method (FEM) we calculate the dispersion of, and model the transmission and reflection from, the periodic MDM illuminated with a transverse magnetic (TM) or p-polarized plane-wave with free space plane-wave $k_0 = \omega/c$.

As discussed in chapter 2, the presence of the periodic modulation allows for the diffraction of propagating light into SPP modes via the addition of extra momentum in integer multiples of the grating wave-vector. With the incident plane-wave perpendicular to the cylindrical modulation, SPP grating coupling occurs (in the simplest approximation) when the SPP wave-vector matches the sum of the free propagating

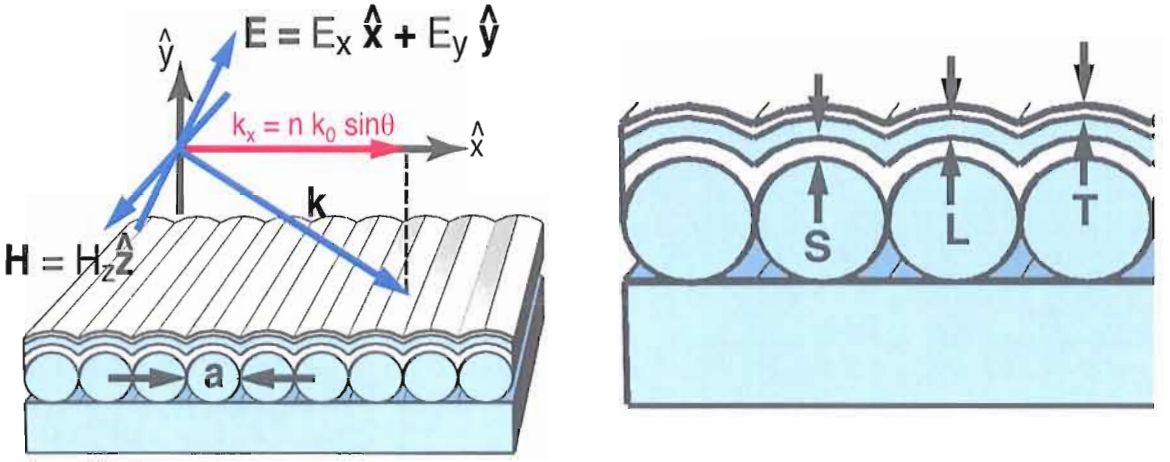

Figure 5.1. Sketch of the cylindrically modulated MDM geometry: (top) coordinate system of a TM (p-polarized) plane-wave scattering from the infinite MDM grating with the plane of incidence oriented perpendicular to the grating plane-wave $\Lambda = 2\pi/a$.(bottom) Geometric parameters of the MDM coating, $S = 30$nm, $L = 100$nm, $T = 15$nm. The colors blue (silica) and gray (silver) indicate the material composition.

plane-wave in-plane component and the grating wave-vector, $G = 2\pi/a$:

$$\mathbf{k}_{SPP} = (\sqrt{\varepsilon_M} k_0 \sin\theta + m\frac{2\pi}{a})\hat{\mathbf{x}} \quad m = (1, 2, 3, ...) \tag{V.1}$$

where a is the first order period of the modulation, m is an integer, $\sqrt{\varepsilon_M} \equiv n_M = 1$ is the index of refraction of the medium from which the plane-wave is incident, and $\mathbf{K}_{\mathrm{SPP}}$ is defined in equation (II.2)

The periodicity results in the folding of the SPP dispersion relation back upon itself across the first Brillouin zone of the grating reciprocal lattice. Manipulation of the shape and periodicity of the the modulation leads to a rich tapestry of possible interactions between the now crossing SPP dispersion branches. We are drawn to

study the plasmonic bands of the folded dispersion diagram (and the interactions between bands) to further our fundamental understanding of the alteration of SPP excitations in the subwavelength dielectric gap of metal-dielectric-metal structures.

By specifying that the layers are silver, silica and silver we form a uniquely modulated MDM geometry simultaneously supporting the three distinctive electromagnetic eigenmodes shown in figures 5.2(a)-(c). These modes can be placed into three familiar classes: exterior surface plasmons (EPS) associated with excitations along the top silver-air interface and the substrate silica-air interface, interior surface plasmons (ISP) confined to the dielectric layer between the adjacent metal films and associated with the coupled plasmons of the two interior silver-silica interfaces, and localized surface plasmon (LSP) modes associated with the excitation of plasmons at the cusps formed by the intersections of rods or layers.

Through our FEM simulations, we have found that these conformal MDM coatings can support radiatively coupled interior surface plasmon (ISP) modes similar to those found in the previous chapter. The details of the FEM simulation can be found in appendix C. There are four ISP induced effects which will be discussed in this chapter: self-interaction of even and odd parity ISPs at the boundary of the Brillouin zone, ISP-ESP hybridization similar to that found in the $M(DM)_x$ spherical shells of chapter IV, interaction of ISP modes with the plasmon enhanced transparency of Ebbesen et al. [19], and ISP coupling to localized surface plasmon resonances (LSPR).

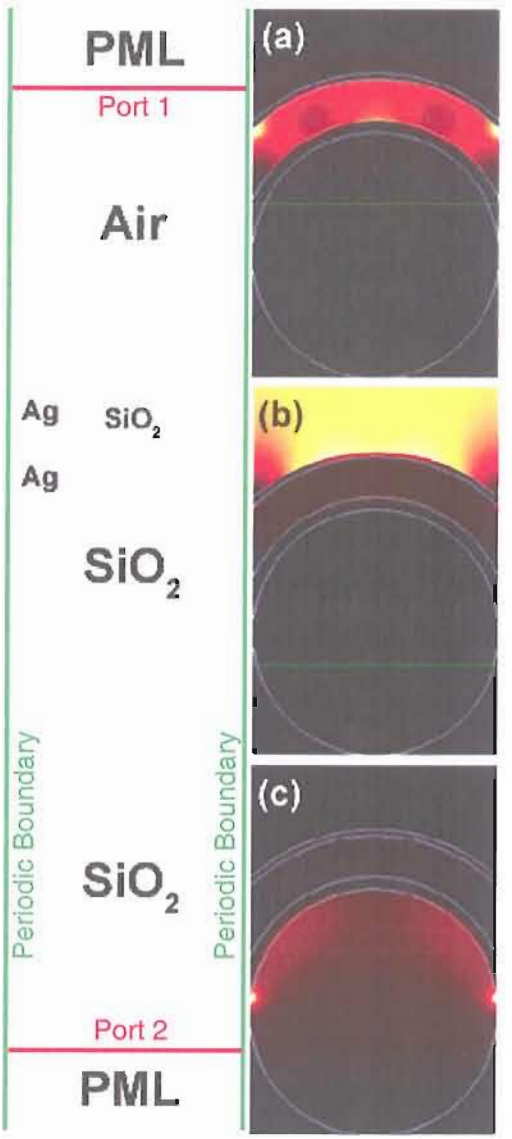

Figure 5.2. (left) Geometry and free mesh of the computational domain used in this study. (right) Total energy density plots of (a) an interior surface plasmon mode ($k_x = 0$, $\omega = 1.54$PHz). (b) an external surface plasmon mode ($k_x = 0.5$, $\omega = 1.57$PHz). (c) a localized substrate plasmon mode($k_x = 0$, $\omega = 1.97$PHz).

ISP Mode Parity

We begin examining the results of our FEM simulations by examining the plasmon band-edge splitting induced by the MDM coating periodicity. In figure 5.3(left) we have plotted the dispersion relation and plane-wave absorbance for the MDM geometry of figure 5.2. The absorbance, $A \equiv \log(1-(\mathcal{T}+\mathcal{R}))$, is for a TM polarized plane-wave incident from the air side of the MDM coating. The plane-wave is defined as $E_0 e^{-in_m \mathbf{k}\cdot\mathbf{r}+i\omega t}$ and originates at port 1, $\mathbf{k} = n_m k_0(\sin\theta\hat{x}+\cos\theta\hat{y}) \equiv k_x\hat{x}+k_y\hat{y}$, and the input field strength is given by $E_0 = 1V/m$. $\mathcal{R}$ is the reflectance calculated from the normalized power flux through to port 1 (as defined in figure 5.2) in the direction $k_{\mathrm{R}} = -k_x\hat{x}+k_y\hat{y}$. Correspondingly, $\mathcal{T}$ is the transmittance calculated via the power flux flowing through port 2 in the direction $k_{\mathrm{T}} = \mathbf{k} = k_x\hat{x}+k_y\hat{y}$.

The presence of periodicity allows the definition of even and odd parity ISP modes. The parity of the modes is indicated in figure 5.3 with the line colors gray (odd) and black (even). Having lifted the degeneracy at the Brillouin zone boundaries a large self interacting ISP band gap is formed. We have found that this splitting is very large for the cylindrically modulated MDM. The band edge gap formed at $\omega_c = 1.5$PHz is characterized by the normalized gap size ($\Delta\omega/\omega_c = 0.06$). It is clearly shown in 5.3(left) and (c) that excitation of the upper band is not possible at $k_x = 0$. Under this normal illumination, only even parity modes may be excited due to the constant phase of the transverse electric field E_x [101]. Examination of the mode symmetry

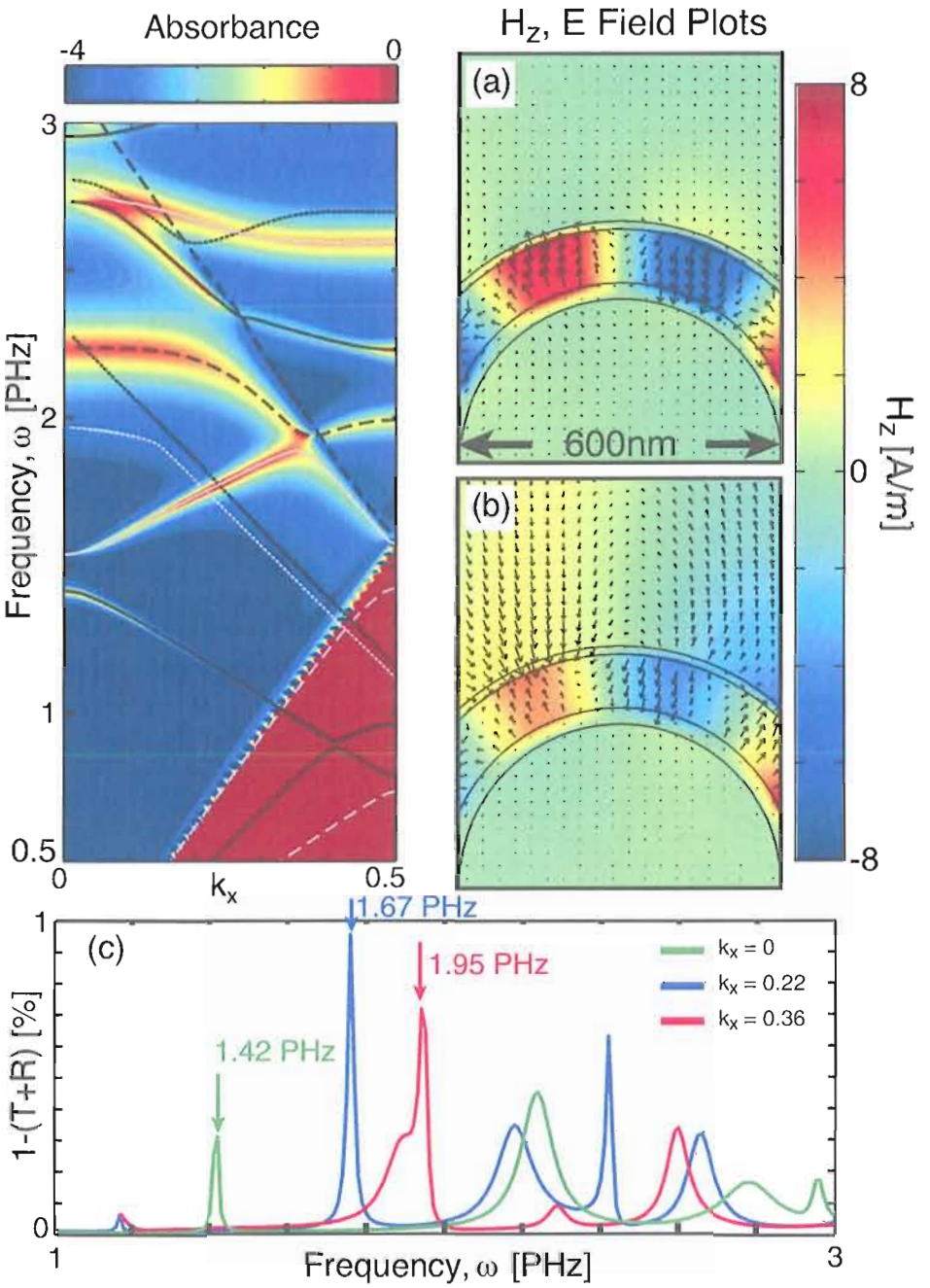

Figure 5.3. (left) Band diagram overlaid upon normal absorption ($\log(1-(\mathcal{T}+\mathcal{R}))$) of the periodic MDM coating of figure 5.2. The line style indicates the dominant mode character at $k_x = 0$: ISP (solid), ESP (dashed), SSP (dotted) and its color indicates parity: black (even) and gray (odd). (c) Absorbance vs. frequency cross-section plots at three values of k_x indicating the strong excitation of ISP ($k_x = 0.22$) and ESP-ISP hybridized ($k_x = 0.36$) modes.

reveals that the upper mode possesses odd parity and the corresponding lower even mode couples to the free propagating plane-wave under normal illumination. This is also true of the even parity ESP mode found at ($k_x = 0, \omega = 2.2$ PHz)). As we move away from normal incidence the phase variation along the x-direction allows the excitation of the odd parity ISP branch.

ISP-ESP Coupling in Modulated MDM Layers

Next we discuss the results of strong coupling between this odd parity ISP band and an overlapping ESP mode. Similar to the results of previous chapters, the SPP-SPP coupling of an ISP and an ESP mode at the point ($k_x = 0.36, \omega = 1.9$ PHz) results in an avoided crossing and hybridization of the energy levels. As we have previously shown in chapter IV, the strength of this coupling, and thus the width $\Delta\omega = 0.12$PHz, is controlled through the thickness, L, of the top silver layer.

The hybridization of the ISP mode allows for the strong excitation of the gap plasmon with a freely propagating plane-wave. The absorbance cross-section plot (figure 5.3(c)) along $k_x = 0.36$ shows the strong absorbance of the incident plane-wave energy at $\omega = 1.9$ PHz. The spatial field distribution (figure 5.3(b)) shows that the energy is concentrated in the silica gap and on the top surface of the MDM coating.

Next, in the cross-section plot of figure 5.3(c) we note the exceptionally high plane-wave ISP coupling efficiency (~96%) at ($k_x = 0.22, \omega = 1.76$ PHz). Examination of

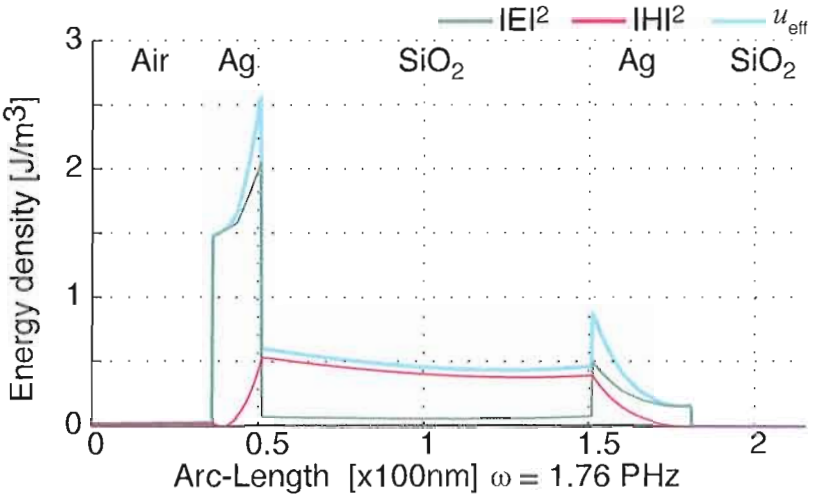

Figure 5.4. Cross-sectional plot of the electric field energy density through an MDM coating at the position of 96% efficiency ISP generation ($k_x = 0.22$, $\omega = 1.76$PHz)

the TM eigenmode field distribution (figure 5.3(a)) confirms this is a highly confined ISP with minimal surface plasmon excitation above or below the MDM coating. In figure 5.4 we plot a cross-section of the time averaged energy density distribution of this ISP mode. The cross-section plot shows the weak excitation of SPPs associated with the external silver interfaces. In figure 5.4 we further break the time averaged total energy density into the electric and magnetic components. It is clear that while the electric field energy is highly concentrated in the surrounding silver films, the magnetic field energy lies mainly in the silica gap. This magnetic resonance character is typical of ISP excitations explored in planar MDM systems [102].

The characteristic, high confinement and narrow spectral width of these ISP modes

makes them a useful candidate for future applications in nanoscale device fabrication. The maximum field energy density generated in the silica gap by the excited ISP mode ($u_{\text{gap}} \sim 0.5$ J/m^3) is enhanced by three orders of magnitude over the average energy density of the incident $\omega = 1.76$ PHz plane-wave ($u_{\text{pw}} = 0.0056$ J/m^3). This could prove very useful for applications in which large field enhancements in nano-scale volumes play a critical role such as SERS [52]. Additionally the narrow resonance of the ISP mode creates the opportunity for high sensitivity sensors. As an example, in figure 5.5, we plot the change in the ISP central resonance frequency, ω_c as a function of interior dielectric constant n_d. We see that a change of refractive index of $\sim 1\%$ is sufficient to shift ω_c by its full width half maximum. This corresponds to

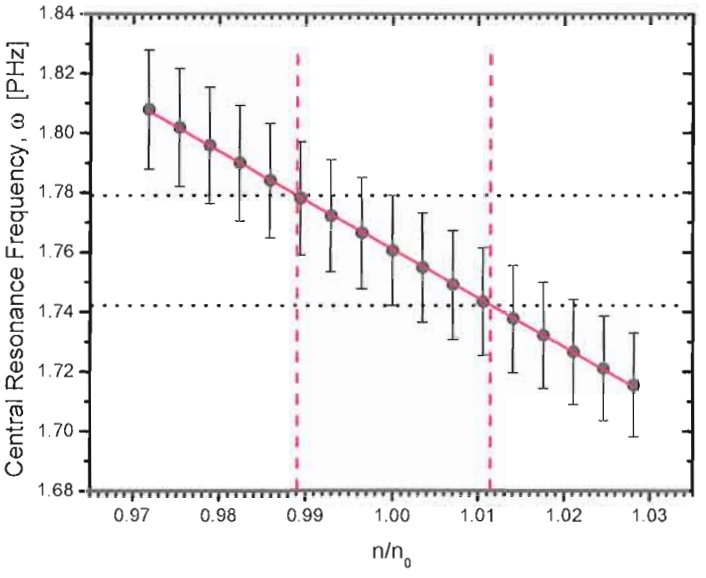

Figure 5.5. Change in central resonance frequency of $k_x = 0.22$ ISP resonance as a function of $\Delta n = n/n_0$, where $n_0 = 1.42$. Error bars indicate the resonance full width half maximum (FWHM). A one percent change in the index of refraction is sufficient to shift the central frequency by the resonance FWHM.

$\Delta\omega/\Delta n$ = 2PHz per refractive index unit or $1.2^{\mu m}/_{RIU}$. This is two times the value of the state of the art grating based SPR sensors. For comparison, the best value for grating based surface plasmon biosensors is given by Homola et al. as $0.63^{\mu m}/_{RIU}$ [16].

ISP Control of SPP Enhanced Transmission

It has been shown that periodic modulation of a metal film leads to enhanced transmission through the metal due to the excitation of SPPs on both sides of the film (cf. [19, 103] and references therein). To compare the transmission through an MDM to this SPP enhanced transmission, we have simulated the transmission through a modified MDM coating with the top silver layer removed (a DM coating). This creates a symmetric (silica-silver-silica) system capable of SPP enhanced transmission. In figure 5.6 we show the transmission through the modulated DM and MDM coatings. As can be seen in figure 5.6(b) the enhanced transmission through the the DM coating is very broad, and exists in the regions between the branching modes of the air and substrate SPPs. In contrast, the transmission through the MDM structure, figure 5.6(a), is tightly bound to the excitation of the ISP modes. The maximum transmittance through the MDM structure is comparable in magnitude to the DM structure, but now its angular emission characteristics have been shaped by the ISP mode dispersion.

To gain insight into this ISP transmission masking we examine the energy density

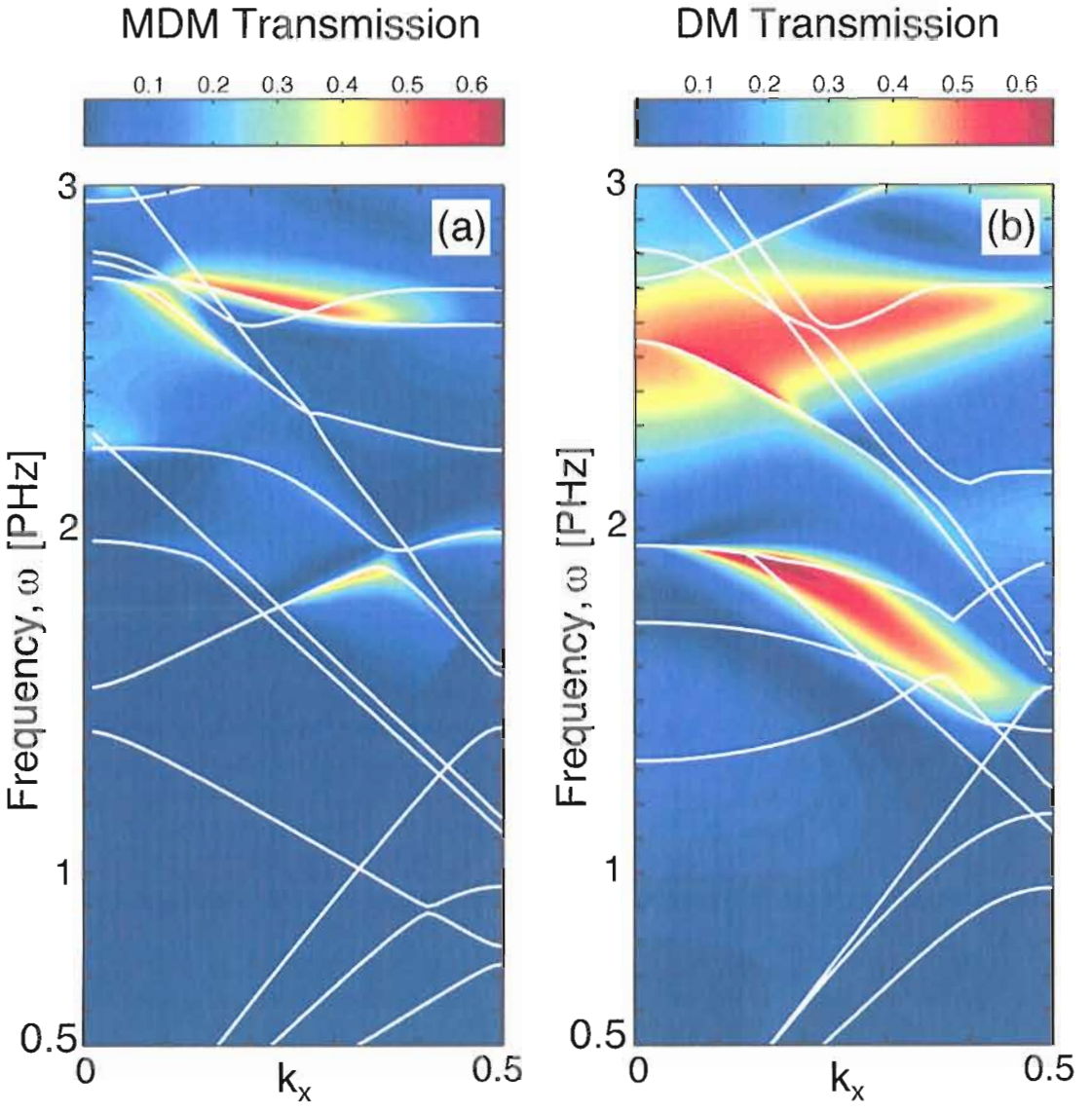

Figure 5.6. Transmission through (a) the MDM silver-silica-silver of figure 5.2 and (b) silica-silver (DM) coating coating created by removing the top silver layer from the geometry shown in figure 5.2.

distributions created from an incident plane-wave around the MDM enhanced transmission point ($k_x = 0.23, \omega = 2.67$PHz). In figure 5.7 energy density cross-sections at varied incident angles around the maximum transmission angle of $k_x = 0.23 = 11°$ are plotted. This shows that maximum transmission does not happen at the location of most efficient ISP generation ($k_x = 0.19$), but rather when the ISP is most efficiently coupled to the symmetric SPP mode of the silver-silica interface. When this condition is met, the electromagnetic field is strongest exiting the MDM film and maximum transmission is found. When the ISP does not generate the strong symmetric bottom film SPP, enhanced transmission is prohibited.

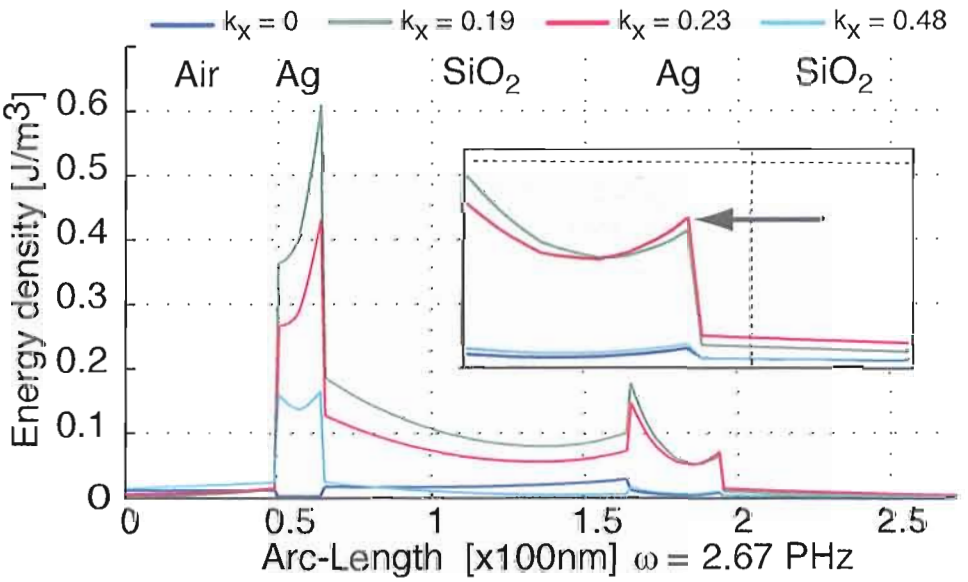

Figure 5.7. Cross-sectional plots of the electric field energy density through an MDM coating for varied incident angles around ISP enhanced transmission maxima ($k_x = 0.23$, $\omega = 2.67$PHz).

Coupling of ISPs to Localized Cusp Modes

We end this discussion of ISP mode coupling with the an examination of the ISP coupling to the last dominant mode type mentioned in the introduction: the cusp localized surface plasmon mode. The intersection of two cylinders or shells creates nano-scale points (or cusps). In this simulation the cusps are formed by rounding off the geometric points formed at the intersections of the layers and rods with the artificial computation boundaries. This is done with radius=2.5nm spheres. Cusp modes are characterized by very large ($\sim 10^2$) field enhancements and flat dispersion [104, 105]. By changing the periodicity (that is, the cylinder radius) of our MDM structure to 300nm we show the development of such a nearly flat band at $\omega = 3.2$PHz, (figure 5.8). We have additionally shrunk the dielectric spacer thickness to 60 nm to maintain the high confinement condition $\lambda_0/10$, as above.

In figure 5.8 we plot the dispersion relation and normal absorption of a 300nm silica cylinder with a 30nm-60nm-15nm silver-silica-silver MDM coating. Again, the dispersion relation is overlaid upon the film absorbance. As above, the absorbance was calculated by simulating a plane-wave incident from the air side of the MDM with wave-vector $\mathbf{k} = k_0(\sin\theta\hat{x} + \cos\theta\hat{y})$. At $\omega = 3.2\,\mathrm{PHz}$ a flat band extends from $k_x = 0$ to $k_x = 0.34$. At $k_x = 0.34$ interaction with other modes reduces the excitation of the LSP. The mode structures of the localized mode at $k_x = 0$ and the hybridized LSP/ISP/ESP mode formed at $k = 0.40$ are shown in figure 5.8(b). In figure 5.8(a)

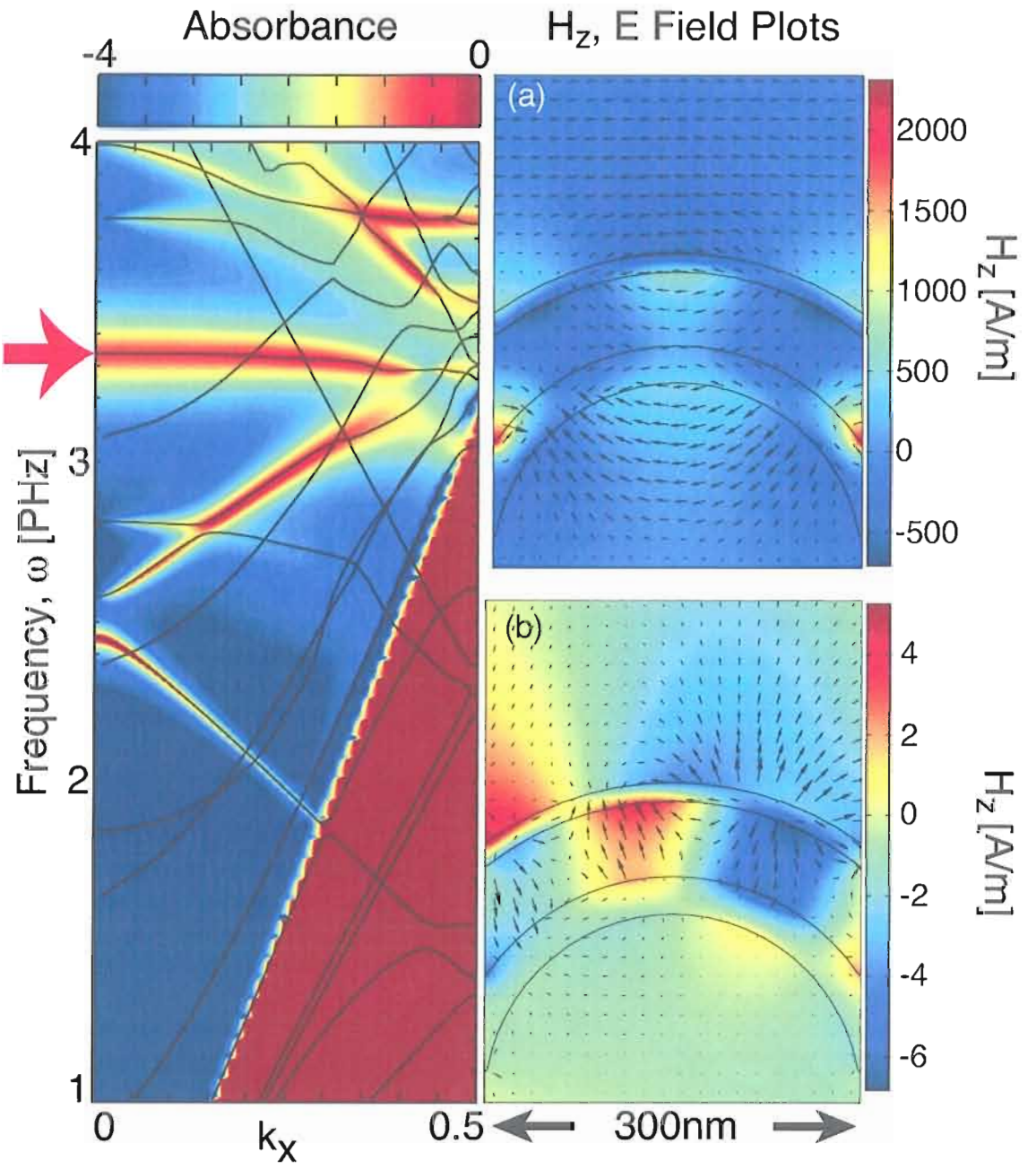

Figure 5.8. (left) Band diagram overlaid upon normal absorption of a $a = 300$nm MDM coating. This geometry supports a localized, dispersionless plasmon cusp mode near $\omega = 3.37$PHz (560nm). (right) Magnetic and Electric field distributions of (a) the localized cusp mode at ($k_x = 0$, $\omega_k = 3.37$PHz) and (b) the LSP/EPS/ISP hybrid mode at ($k_x = 0.40$, $\omega = 3.3$ PHz). The filled contour plot is the H_z magnitude, and the arrows are proportional to $\mathbf{E} = E_x\hat{x} + E_y\hat{y}$.

we plot the H_z and $\mathbf{E}$ fields of the cusp mode. In addition to the significantly small field volume, it shows the large ($\sim 10^3$) enhancements of the cusp mode H_z amplitude with respect to the hybridized mode of figure 5.8(b).

Conclusions

Using FEM calculations we have demonstrated that it is possible to directly couple freely propagating modes to ISP (gap plasmon polaritons) using the grating coupling method. Narrow resonance ($\Delta\omega/\omega = 0.02$) and high coupling efficiency (96%) is possible under tunable excitation conditions. This can be done even with very thin (15 and 30nm) silver films, providing very low absorption loss while maintaining high spatial confinement ($\lambda/10$). We have additionally shown the effect of the existence of the interior plasmon mode on the surface plasmon enhanced transmission. The interior plasmon mode can be use to tailor the enhanced transmission characteristics of the modulated metal film with minimal impact on the overall transmission efficiency. Lastly the plane-wave excitation of localized cusp modes has been demonstrated and we have shown the large field enhancements associated with the excitation.

CHAPTER VI

FABRICATION OF PERIODIC MDM COATINGS

Introduction

In this chapter we manufacture and analyze a novel 2D plasmonic surface which is to be used in studying coupled ISP excitations in open Bragg resonators. Using evaporative self-assembly we deposit monolayers of hexagonal close packed (HCP) silica spheres to act as a hemispherically modulated substrate for conformally coated silver-polystyrene-silver MDM trilayers. We use surface analytical tools such as scanning electron microscopy and atomic force microscopy to characterize the quality of the prepared samples.

Monodisperse Silica Spheres

A crucial ingredient in creating HCP silica sphere monolayers (also referred to as monolayer opals) is the synthesis of monodisperse silica spheres with radii in the 200-500nm range. We accomplish this using the well published Stöber method [106]. In our work, the Stöber reaction is the hydrolysis of tetraethylorthosilicate (TEOS) in ethanol. In a base-catalyzed environment, nucleation of silica nanoparticles grow to

form monodisperse ensembles of micron-scale spheres. The standard deviation of the sphere size is the most important parameter in growing high quality ordered crystals. Thus, following the work of Gieche [107, 108], we have grown batches of silica spheres based on the recipes shown in table 6.1.

Chemical Reaction Method

All glassware was pre-cleaned with hydrofluoric acid and subsequently dried at 80° for at least 6 hours before use. This prevented contamination by parasitic water and dust particles; the former is a reactant and the latter facilitates uncontrolled nucleation of silica particles. Random nucleation destroys the monodispersity of the silica sphere ensemble, and thus must be avoided. Typical 200ml reactions were prepared by combing all reactants except the TEOS in 500ml round bottom flasks under vigorous stirring. TEOS was distilled at 165° just prior to use and mixed 1:1 with ethanol (EtOH) before rapid injection into the round bottom flask. The most monodisperse reactions were obtained when the TEOS/EtOH mixture was quickly

Table 6.1. Stöber reaction constituent molarities for synthesizing monodisperse silica spheres in ethanol. The resulting sphere average diameters and standard deviations are also given. $(\cdot)^{\dagger}$ indicates active cooling.

S-Rxn	TEOS	H_2O	NH_4OH	EtOH (mL)	Temp ($^{\circ}C$)	R	σ_R
3	0.2	13	4.2	70	$30^{\dagger}$	235	15.6
5	0.18	13	4.2	140	20	285	12.4
6	0.1	13	4.2	144	$10^{\dagger}$	250	13.5
8	0.18	13	4.2	140	$20^{\dagger}$	200	9.5
9	0.18	13	4.2	133	20	250	9.6
10	0.2	13	4.2	128	20	258	10.2

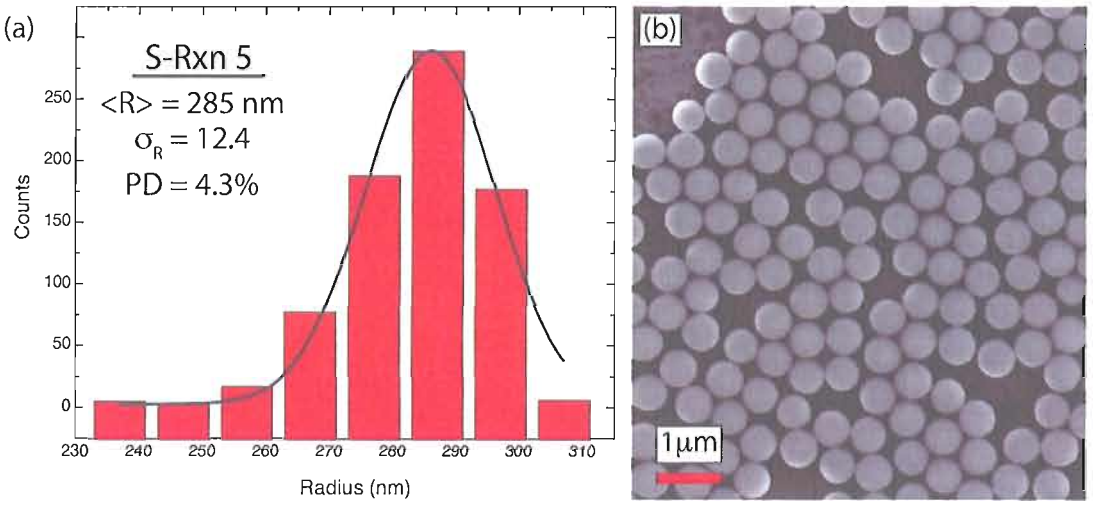

Figure 6.1. (a) Measured size distribution and (b) SEM image of Stöber reaction 5.

and smoothly added below the solution surface with two extra-long wide-bore needles on 5ml syringes. The reactions were allowed to proceed for at least 6 hours before centrifugation cleaning in EtOH. The resulting monodisperse spheres were stored in EtOH until needed for deposition.

Sphere Distribution Characterization

Small amounts of the Stöber spheres were dispersed on copper-Formvar transmission electron microscope (TEM) grids for sizing with our Hugh transform analysis algorithm [109]. Sizing results for the spheres used in this work can be found in figures 6.1 and 6.2. A summary of batch polydispersities ($\equiv \sigma_R / < R >$) can be found in table 6.1. Despite contrary reports [110], it was found that post growth

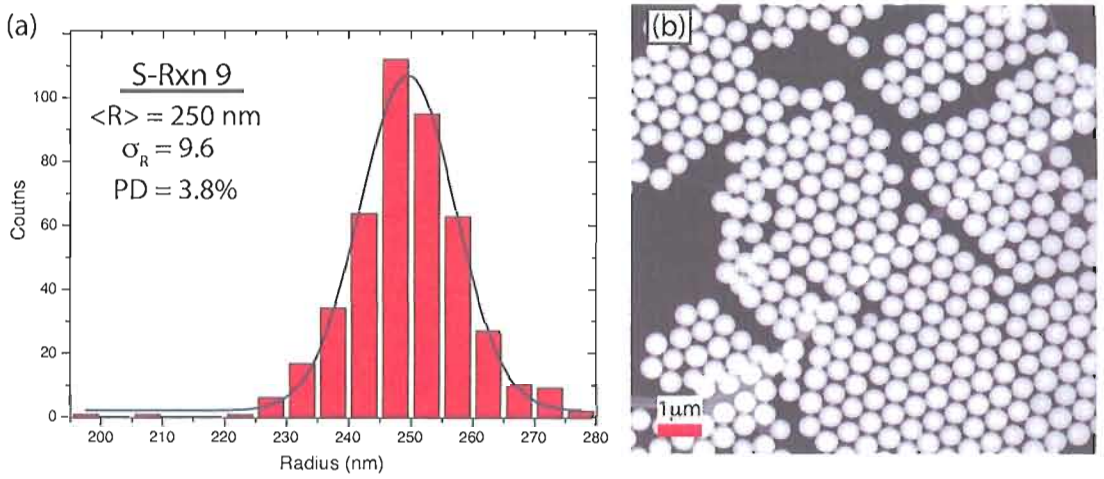

Figure 6.2. (a) Measured size distribution and (b) TEM image of Stöber reaction 9.

sedimentation filtering had minimal impact on the overall sphere size polydispersity. This is most likely due to the fact that a seeded growth process was not used to initialize the Stöber reaction. This results in a monodisperse distribution of sphere diameters rather than a bimodal distribution, making sedimentation filtering much less effective. Using the above procedure, typical polydispersities of 4% were obtained with deviations between 3% and 5%.

This was deemed acceptable for HCP crystallization, as polydispersities below 6% have been shown to produce high quality ordered crystal structures [111]. Despite this, it should be noted that smaller polydispersities result in opal monolayers with fewer point and line defects. Wong, et al. have shown that very large ($> 10^4 \mu m^2$) single domains are possible if the sphere polydispersity $< 2\%$ [110].

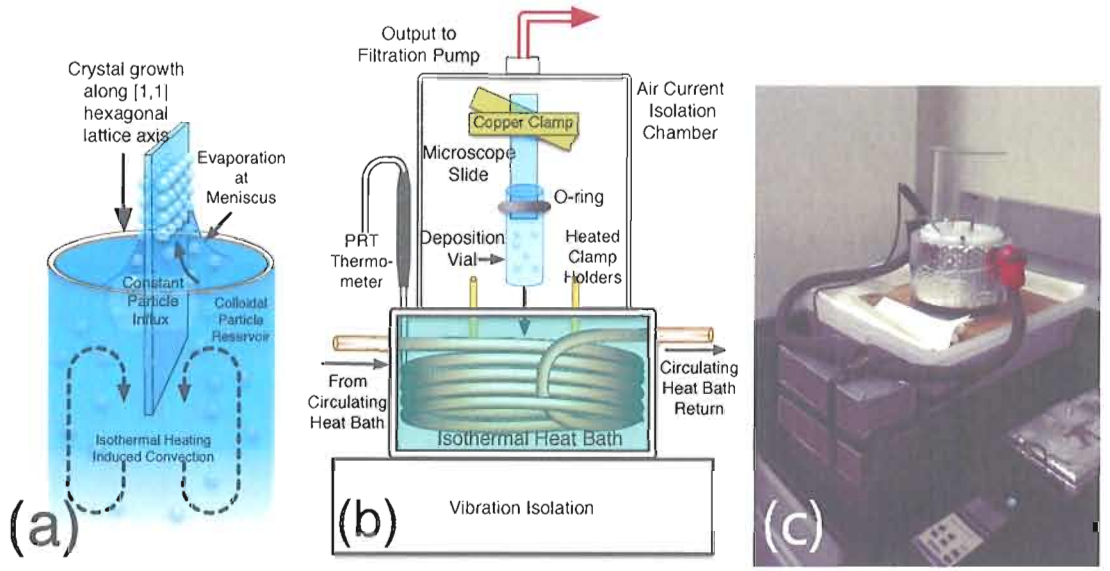

Figure 6.3. Diagrams of (a) evaporative self-assembly process and (b) the isothermal-heating evaporative self-assembly (IHESA) chamber built to grow vertically deposited opal monolayers. (c) A picture of the IHESA chamber, before the addition of the evaporation filtration pump.

Isothermal Monolayer Self-Assembly

The crystal growth process is conducted with vertical deposition evaporative self-assembly. Illustrated in figure 6.3, evaporative self-assembly works through the surface-tension aided deposition of colloidal particles at the meniscus of an evaporating solvent. This process is notoriously susceptible to environmental conditions and can result in enormous variability in the quality of the crystals produced.

To overcome these difficulties, we follow the work of Wong, et al. in engineering a crystal-growth chamber (figure 6.3) to uniformly deposit ordered monolayers over large areas with high reliability and repeatability. The control of the crystal growth

process is based on isothermal heating, evaporative self-assembly (IHESA). The IHESA method relies on the immersion of the solvent-particle (EtOH-silica sphere) slurry into a strictly controlled temperature bath. By maintaining the heat bath at a temperature slightly above the boiling point of the evaporating solvent, uniform convection of the evaporating solvent stirs the slurry without disturbing the deposition meniscus. The convective flow ensures a constant uniform concentration of spheres at the meniscus during the deposition process. In addition to the approach outlined in [110], we have added the continuous, constant removal of the evaporating solvent vapor (KNF Lab N811KV Filter Pump) and total isolation from external air currents. This has improved the repeatability of the deposition process by eliminating solvent re-condensation within the evaporation chamber. The isothermal bath chamber is machined from a solid block of polyethylene and filled with ~ 1 liter of ethylene glycol. The temperature of the bath is maintained by a NESLAB RTE 111 circulating temperature controller, and monitored with a platinum resistance thermometer. The heat of the circulating fluid is transfered to the ethylene glycol through copper tubbing inside the iso-bath chamber. We have found that this setup reliably produces large area synthetic opals with a tunable number of layers for of sphere sizes in the range $r = 200\,\text{nm} - r = 380\,\text{nm}$.

The concentrations of silica spheres used to create a sphere monolayer were established by starting with a high concentration of sphere ($> 2\%$ by weight) and successively halving the concentration until a monolayer was obtained. Typical deposition

concentrations can found in table 6.2. It should be noted that the temperature of the evaporating solvent must be controlled to a very high tolerance during the deposition ($\pm 0.05^{\circ}$ typical). Additionally, the temperature of the IHSEA isothermal bath *must* be slightly above the boiling point of the solvent (cf. table 6.2). It was found that the most critical parameter for successful deposition is the temperature of the evaporating solvent. The solution temperature must be at (or slightly above) the solvent boiling point. In our depositions, we found that a solvent temperature of $78.9 \pm 0.5^{\circ}$ was adequate for successful ordered growth. The temperature of the evaporating solvent will change as a function of the surface area exposed to atmosphere. As a result, careful control experiments were conducted to establish the correct isothermal bath temperature for situations where the deposition vial geometry was changed.

When used as evaporation vessels, large (25ml) scintillation vials with an aspect ratio of 3:1 (length:width) were eventually found to produce the best results. The large volume of these containers ensured a large reservoir of sphere solution and provided a nearly constant concentration of spheres during deposition. The deposition vials (

Table 6.2. Typical deposition parameters for crystallization of opal monolayers. Vacuum levels were held at 6.25" Hg for all reactions, and "S Rxn" cross-references the table 6.1 reaction numbers. The deposition time is given in hr:mins.

Sample	Chiller ($^{\circ}C$)	Iso-Bath ($^{\circ}C$)	Radius (nm)	S Rxn	% weight	Time
57	86.45	84.03	285	5	2.6	3:20
60	86.35	84.05	285	5	2.6	2:55
84	86.35	83.90	250	9	0.3	-
86	86.35	83.92	250	9	0.3	3:00
87	86.35	83.73	300	8	0.67	3:00

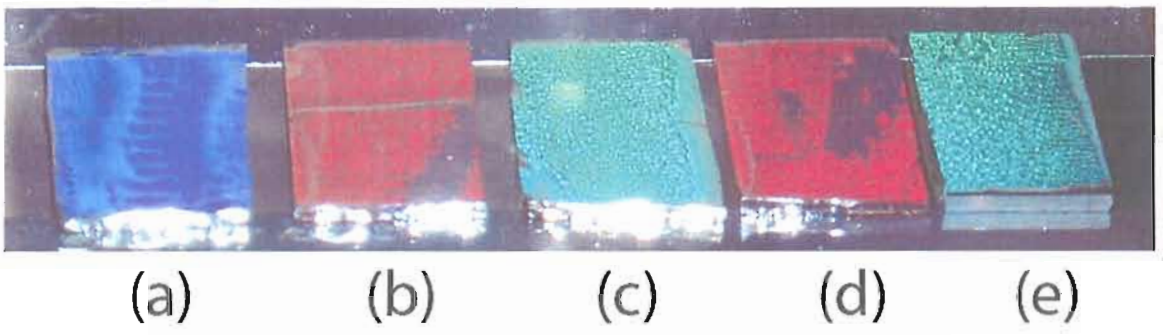

Figure 6.4. Examples of silver coated opal monolayers with a variety of sphere radii: (a) 200 nm (b) 250 nm (c) 285 nm (d) 250 nm (e) 285 nm. The glass substrates are cut to $5/8'' \times 3/4''$. Second layer striping manifests as darker regions and speckle.

and the cut $3/4'' \times 3''$ microscope slides on which the deposition takes place) were pre-cleaned with fresh piranha (3:1 H_2SO_4 : H_2O_2) solution for at least one-half hour before deposition. After cleaning, the slides and vial were rinsed with ultra-pure water and then rinsed with copious amounts of EtOH. In addition to removing the residue and dust disruptive to the crystallization, it is important that no micro-porous contaminants be in the vial during deposition. Because the temperature of the solvent is so close to boiling, *any* air pockets or microscale sharp points can lead to micro-heating. This causes the solution to boil and destroys the crystallization process.

Cut microscope slides (Corning 2947) were cleaned and suspended in the evaporating solvent with heated copper clamps (thermally attached to the isothermal bath) to prevent solvent recondensation and dripping. Typical depositions took 3-3.5 hours, indicating a linear evaporation rate of $\sim$ 1.5cm/hr. This most commonly resulted in

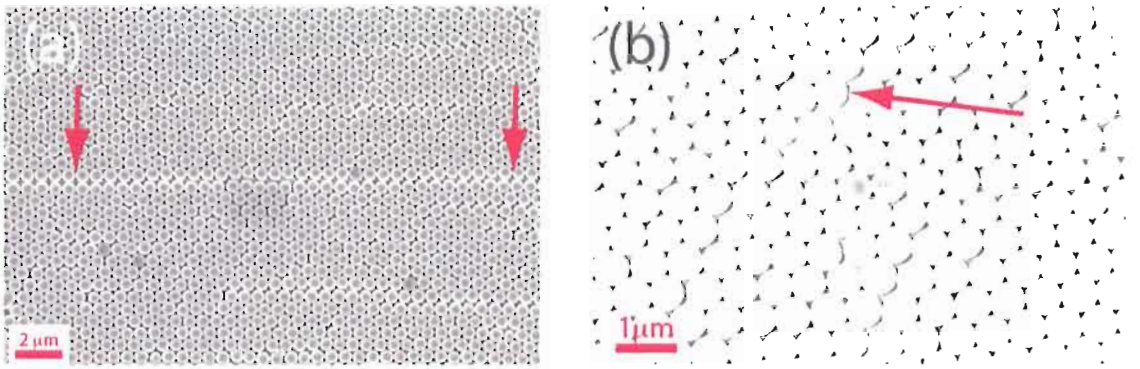

Figure 6.5. (a) An SEM images of silver coated opals taken at 5 kV. (a) showing a typical line defect across its length. Note that the dark spots are imaging artifacts due to surface charging, and not crystal defects. (b) a high magnification image of a typical point defect from a small sphere. Both opals are coated with 50 nm of silver.

an evenly coated $1'' - 1.5'' \times 3/4''$ area of uniform ordered-monolayer deposition with second layer striping on both sides of the microscope slide. Several examples of silver-evaporated monolayer opals are shown in figure 6.4. The monolayer opals were then carefully removed from one side of the slide by wiping with acetone and lens tissues. The resulting single sided samples were then allowed to dry overnight before further processing.

MDM Layer Deposition

High Vacuum Silver Deposition

After drying, monolayer opals were coated with an optically thick silver layer using high vacuum (HV) evaporation. A Key high vacuum metal evaporator was used to deposit a 50nm thick layer of silver at a slow deposition rate of $0.3 - 0.5\mathring{A}/s$. The

results of such a deposition can be seen in figure 6.5. A polystyrene polymer layer is then applied and an additional top 20nm thick layer of silver is evaporated on top of the monolayer opal, forming an MDM structure. In addition, one opal monolayer was coated with 70nm of silver and no polystyrene interstitial layer, to be used as a control sample.

Spin Coating of Polystyrene Conformal Layers

Following the results of Hall, et al. we have used high molecular weight polystyrene (Alfa Aesar, #41936, MW:200,000) dissolved in toluene to conformally coat the monolayer opals [112]. Huang, et al. have shown that spin coating can produce thin ($\sim$ 100nm) conformal PMMA layers on a sinusoidally-modulated surface with high (1:1) aspect ratios [113]. We have applied this same method to generate uniform polystyrene layers of controlled thickness (from 120–160nm) over the surface of coated opal substrates.

To calibrate the thickness of the polystyrene films, glass cover-slips were prepared with piranha solution cleaning. One-half of the cover-slips were then coated with 50 nm of silver, using the same HV evaporation deposition as above. Following Hall, et al. 4% by weight, polystyrene and toluene solutions were prepared and stirred in a VWR vortex stirring machine for at least one-half hour before spin coating. Calibration graphs for spin settings vs. layer thickness were then produced for speeds between 2000 rpm and 6000 rpm. The samples were completely covered with the

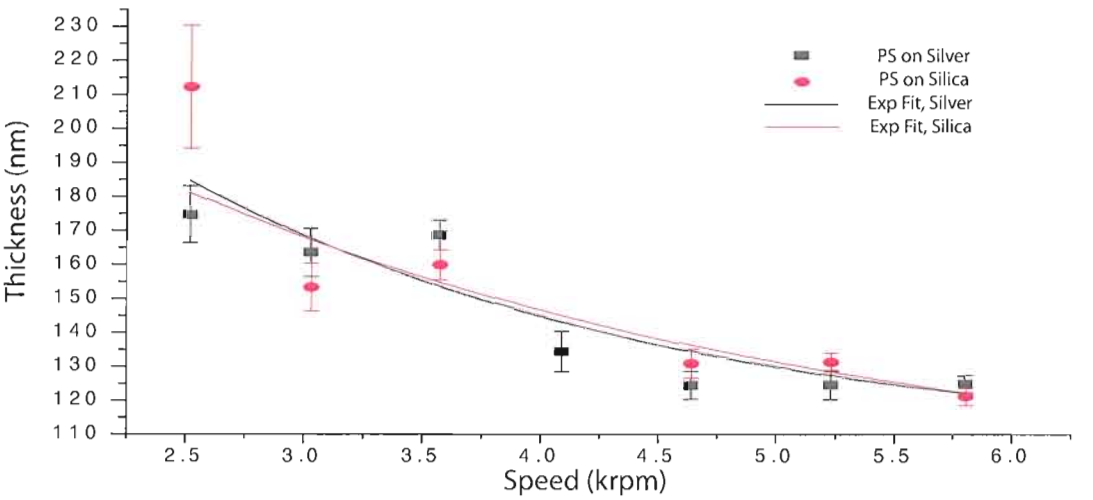

Figure 6.6. Calibration of spin coat rotation speed vs. polystyrene layer thickness. The layer thickness and standard deviation are shown for two substrates (silver and silica) using 4% by weight polystyrene in toluene. Least squared fits to exponential functions are also shown.

coating solution and then spun for 60 seconds and allowed to dry overnight. After scoring the sample with a razor blade, a Dektak 6 surface profiler was used to asses the height and uniformity of the polystyrene film. Up to ten independent 5 μm long scans were taken for each sample, and used to plot the average thickness and standard deviation of the film (see figure 6.6). Conformal polystyrene coatings were then applied to silver-covered opal monolayers with spin conditions selected to create polystyrene layers with thickness from 125nm to 160nm.

MDM Layer Characterization

The quality of the opal crystal domains and the uniformity of the polystyrene and silver layers were assessed using scanning electron microscopy (SEM) and atomic force microscopy (AFM). AFM images of silver coated and silver–polystyrene coated mono-layered opals can be found in figure 6.7. These images demonstrate the retention of uniformly modulated hemispheric surfaces throughout the deposition process and spin-coating. The $\sim$ 50 nm reduction in the absolute magnitude of the silver-polystyrene coated AFM image (as shown in figure 6.7(a)) indicates that the polystyrene layer is preventing the AFM probe tip from penetrating as far into the gaps between the spheres as its geometry allows. We surmise that polystyrene layer is uniformly capping the silver coated opal. This is further confirmed below with SEM images of MDM coatings

To assess the long range uniformity of the MDM layers and mono-layered opals, SEM (Zeiss Ultra FEG) images were taken when conductive surfaces were available (after silver evaporation). Figures 6.9(a) and (b) show the uniformity of opal monolayers over long distances. In figure 6.8 we show detailed results of spin coating an ordered monolayer with a layer of polystyrene. We note that, after polystyrene coating, the defect locations of the monolayer opal are highly enhanced in the SEM images. This is due to charging of the sample surface at the location of the holes in the applied polystyrene layer. We have discovered that the polystyrene spin coating

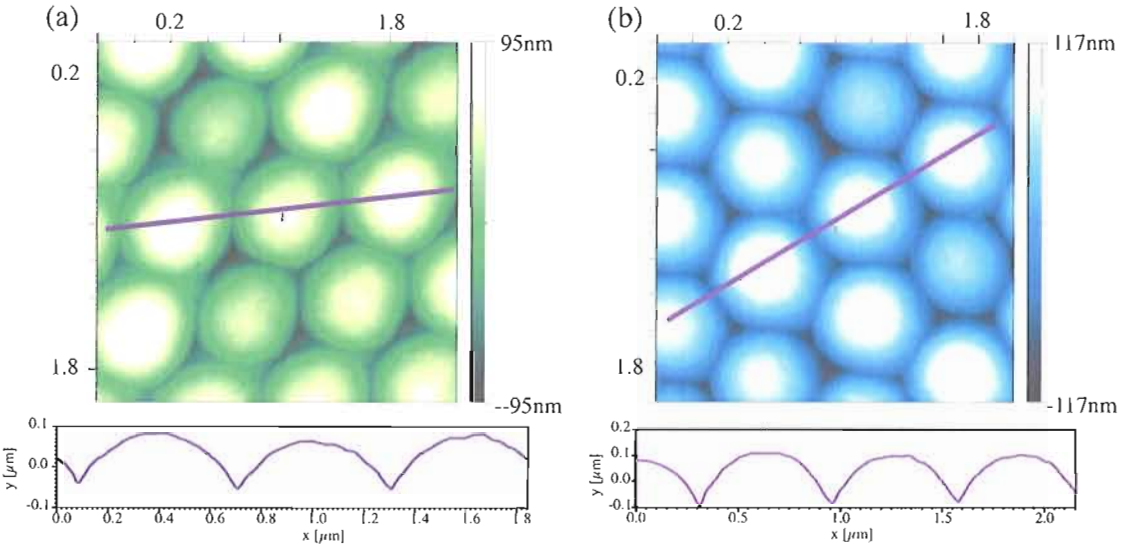

Figure 6.7. AFM images of (a) silver-polystyrene, and (b) silver coated monolayer opals. Inset are line profiles of the highlighted paths in the above images.

process fails at the location of point defects (missing spheres) and line defects (crystals domain boundaries) but is otherwise uniformly applied over large areas of the monolayer opal.

The sensitivity of SPPs to surface features makes the high defect density a point of concern. However, we will show in the next chapter that these defects do not eliminate the signature of MDM ISP excitation. Further refinement of the sample growth process should lead to improvements in crystal quality and domain size. Specifically, the reduction in the polydispersity of the monodisperse silica spheres, either through seeded growth [107] and/or more refined sedimentation filtration, would seem to be the most important factor [110].

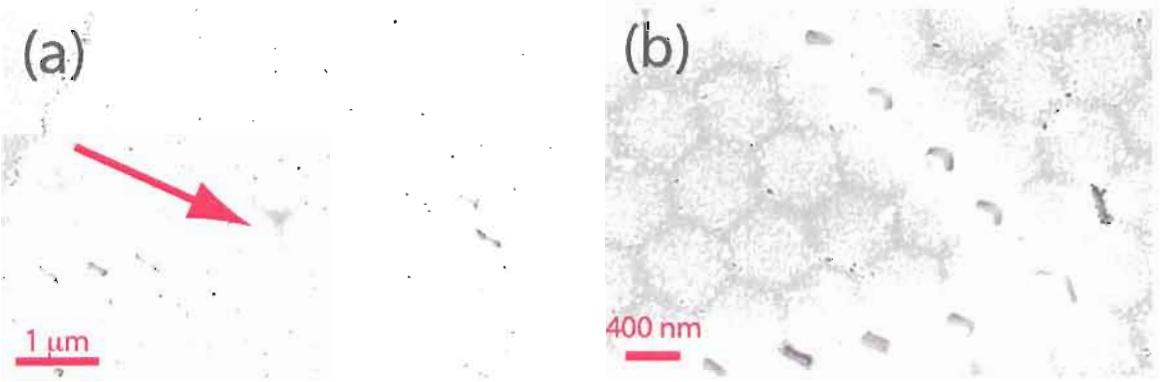

Figure 6.8. SEM images of silver-polystyrene-silver coated opal monolayers. (a) An MDM layer near an open area in the HCP monolayer, with the red arrow indicating the crystal growth direction. (b) High magnification image of a break in the MDM layer caused by an underlying line defect terminating in a missing sphere point defect. (b) also shows the suspended nature of the polystyrene layer over the silver coated opal. The polystyrene does not fill the interstitial voids of the crystal monolayer.

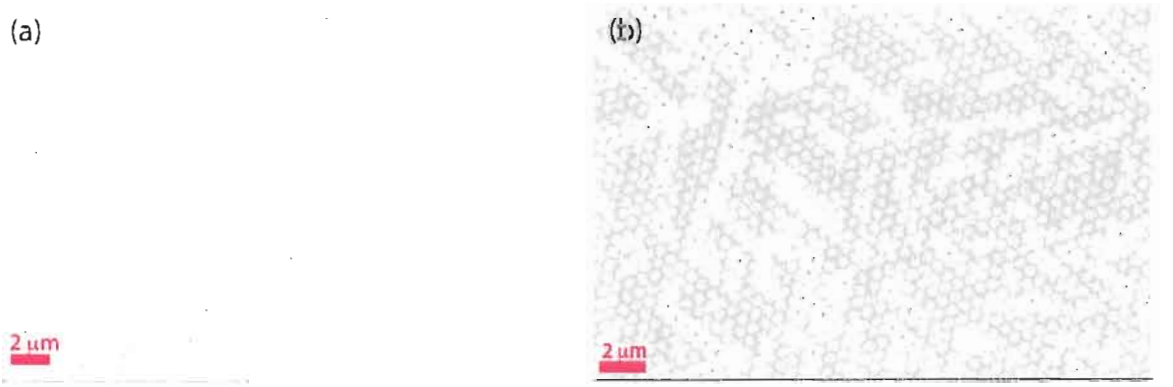

Figure 6.9. SEM images of the long range order of the HCP monolayers. Silver-polystyrene-silver coatings are shown capping the opal monolayer. The polystyrene layer is seen to fail at defect sites in the underlying crystal.

The use of more advanced methods for deposition of the dielectric spacer (chemical vapor deposition or pulsed laser ablation deposition) may produce better results for thinner layers. However, we find that, away from the crystal defect areas, spin coating of ~100nm thick polystyrene layers proves to produce adequate conformal layers suitable for creating plasmonic MDM layers.

CHAPTER VII

ANGLE RESOLVED SPECTROSCOPY OF MDM COATINGS

Introduction

A defining quantity of SPPs are their unique dispersion relations. In chapters II and III we have shown that MDM layers and shells can be used to tailor the dispersion relation of plasmonic surfaces. In this chapter we design an experiment to measure the dispersion characteristics of the periodic silver-polystyrene-silver trilayers engineered in the previous chapter. By measuring the far-field transmission spectra of our periodic MDM surfaces at a variety of incident angles we are able to trace out their dispersion relations. Using this angle resolved (AR) scattering spectroscopy, we will find evidence that the manufactured MDM substrates support ISP modes, and that these modes alter the SPP enhanced transmission found in sub-wavelength hole arrays. We will end this chapter with the observation of a new phenomenon, angularly asymmetric SPP enhanced transmission through silver coated opal monolayers.

Design and Alignment of an Angle Resolved Spectrometer

AR Spectrometer Overview

To investigate AR transmission and reflection we have built a spectroscopy system capable of independently altering the collection angle while automatically controlling the incident angle and wavelength. The setup is shown schematically in figure 7.1. The AR spectrometer has a 0.8° angular resolution, 1nm spectral resolution and a pointing accuracy of 40 μrad. By using high sensitivity detectors we can utilize a collimated incandescent light source while maintaining reasonable acquisition times. Acquisition speeds vary with sample extinction, but typical scan times for the samples studied here are between two three hours with 2° and 2 nm resolution.

To produce a small sample area at the sample, light from an incandescent source

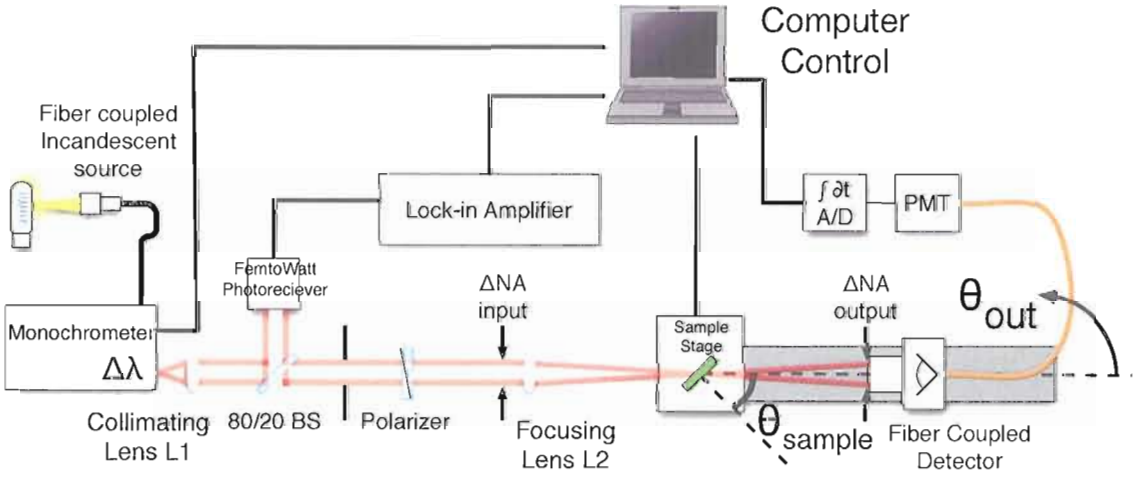

Figure 7.1.. Schematic layout of angle resolved spectroscopy system.

is coupled to a 200 μm core diameter multimode optical fiber (Thorlabs M254L02) with an aspheric fiber collimator (Thorlabs F220FC-B) optimized for the 600-1050 nm range. This provides a pseudo-point source which can be directly coupled into a short focal length spectrometer (Acton Research SpectraPro 2300i). This provides us with a tunable spectral source with 1 nm resolution. The use of a pseudo point source at the entrance of the spectrometer allows us to create a highly collimated output beam. We use an achromatic 100 mm lens (L1) to collimate the output beam before splitting it with a 20/80 non-polarizing beamsplitter. The 20% exit beam is directed into a fiber-coupled, femtowatt photoreceiver (New Focus 2151). This measurement is used for realtime normalization of the input signal. The beam is chopped at a frequency of 650 Hz and the resulting output signal is recorded with a Stanford Research lock-in amplifier (SR830). The remainder of the input beam is directed to the sample ($\sim$ 1.5 m down-beam) passing through a Glan-Thompson polarizer (Newport 10GT04AR.16) set to select p-polarized light with respect to the vertical rotation plane of the sample (cf. figure 7.3).

The collimated beam is focused onto the sample with a 250 mm achromatic lens. The input beam NA is adjustable from 0.04 to 0.008. After the sample, the transmitted–reflected light is collected at a variable collection angle (manually adjusted) with a combination achromatic lens ($f = 75.6$ mm) and fiber collimator (Thorlabs F220FC-B) system. The collection NA is adjustable with a calibrated iris between the collec-

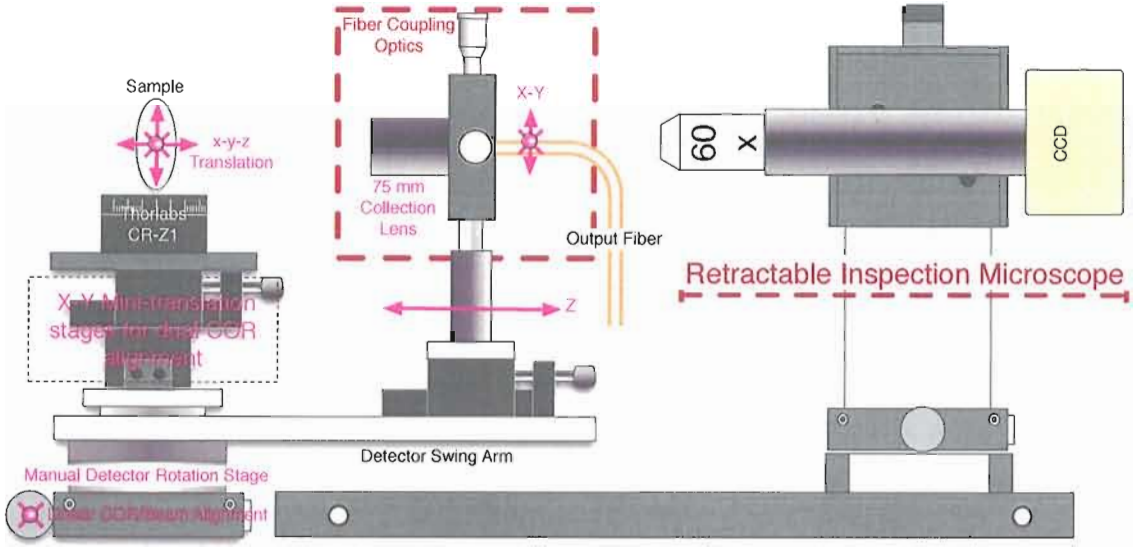

Figure 7.2. Detailed illustration of the angle resolved sample holder, the fiber-coupled collection optics, and the sample inspection microscope.

tion lens and the fiber collimator. The NA is adjustable from 0.11 to 0.013 providing a collection resolution range of $6° - 0.8°$.

The collected light is coupled into a $65\,\mu$m multimode optical fiber (Thorlabs M14L02). We have measured collection efficiencies equal to 65% at633 nm. The use of a fiber coupled detector allows the detection angle to be varied from $-30°$ to $150°$ without beam realignment. The details of the sample and detector optomechanics can be found in figure 7.2, and a detailed illustration of the sample coordinate systems can be found in figure 7.3. The fiber collected light is then detected with a thermoelectrically cooled photomultiplier tube (Hamamatsu 633) set at maximum gain (1500V). The output of the PMT is digitized with a 20bit analog to digital converter (Acton SpectraHub) and collected with our custom Labview acquisition software. The fem-

towatt photoreceiver normalization signal is simultaneously collected and recorded using the SR830 internal data buffer. With the high sensitivity and large dynamic range of the PMT detector and the 20bit converter we have established that our current spectroscopy setup has a noise equivalent power of 10^{-5} at 650 nm (in normalized units).

The sample stage consists of an automated rotation stage (Thorlabs CR-Z6) mounted on linear x-y translation stage. The translation stage aligns the automated rotation stage center of rotation with the manual rotation stage supporting the fiber coupled detector. The sample automated stage and the spectrometer are also automated and controlled with custom Labview software. This allows for the automatic acquisition of spectrally resolved data from a sample, as the sample is rotated about a fixed point in space. As the input beam is held fixed, the sample rotation is equivalent to changing the incident angle. In this study, the detector fixed at $\theta_{out} = 0°$. Thus, as we rotate the sample we record the zero-order extinction of our MDM coated opal monolayers.

Center of Rotation Alignment

The AR spectroscopy system has two alignment tools incorporated into its design: a common path HeNe laser and a home built, retractible, 60x inspection microscope. We use the HeNe laser to mark the sample stage center of rotation and to select highly ordered sample locations. When centered on a highly ordered location the crystal structure of the substrate results in well defined diffraction with characteristic

6 fold symmetry. The alignment microscope is used to inspect the sample surface, set its z-axis position to the focal plane of the lens L2, and to initially align the sample stage center of rotation (see figure 7.2) .

The primary alignment task needed in the AR system is locating the sample stage center of rotation in the $\hat{x} - \hat{z}$ plane. This is accomplished by first placing a thin film 40 μm pinhole in the sample holder. Next, the pinhole is translated to the stage center of rotation by iteratively imaging it with the alignment microscope at the 0° and 180° stage positions until the two locations overlap at the center of the microscope field of view. This can be accomplished with a replacement accuracy of approximately $\pm 5\,\mu$m. The small depth of field of the 60x objective ($< 1\mu m$) further aligns the pinhole location along the $\hat{z}$-axis with the sample stage center of rotation.

The fiber coupled detector is aligned by reversed coupling of the HeNe laser backwards through the collection optics. Independent $\hat{x} - \hat{z}$ linear translation stages are used to align the pine-hole marked center of rotation of the sample stage with the focused laser beam emanating from the collection optics. This procedure aligns the center of rotation of the detector with the center of rotation of the independent dove tail swing arm supporting the collection optics.

With the location of the sample stage center of rotation established, the HeNe alignment laser is focused on the the location of the pine hole with the manipulation of L2 along $\hat{z}$ and with an independent linear translation stage along $\hat{x}$. Additionally, the laser beam passes through a fixed beam pick-off optic after the focusing lens. The

sampled beam is used to align a fixed pinhole, now matched to mark the center of rotation of the sample stage in 3-dimensions. Subsequent alignment of the samples can now be accomplished by illumination with the HeNe alignment laser ($\hat{x}, \hat{y}, \theta = 0, \phi = 0$) and bringing the sample surface into the focal plane of the alignment microscope ($\hat{z}$).

AR Spectrometer Calibration

Chromatic Correction

To overcome the inherent variability of our incandescent light source on the time scale of an AR scan ($\sim$ 2 hours) we have incorporated the real time signal normalization mentioned above. Because the two detectors used are not identical, we must

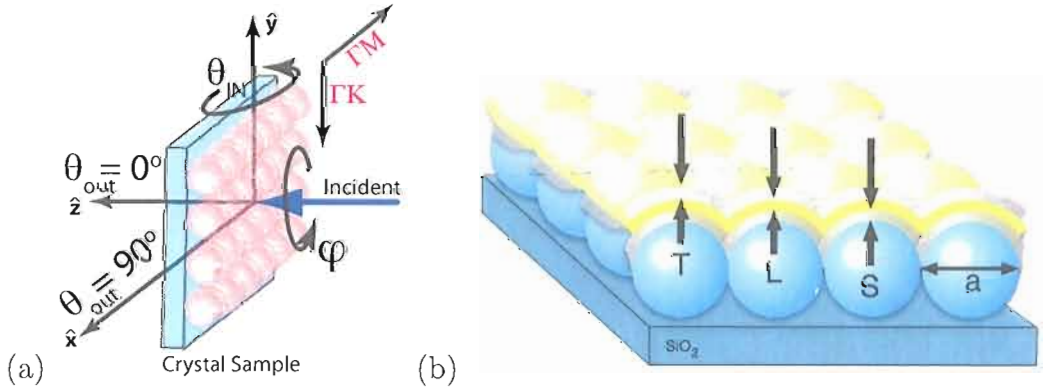

Figure 7.3. (a) Coordinate system of an oriented sample in the AR spectrometer. (b) Geometry of a periodic MDM based on a self-assembled monolayer of silica spheres. Blue is silica, gray is silver, and yellow is polystyrene. The system is embedded in air.

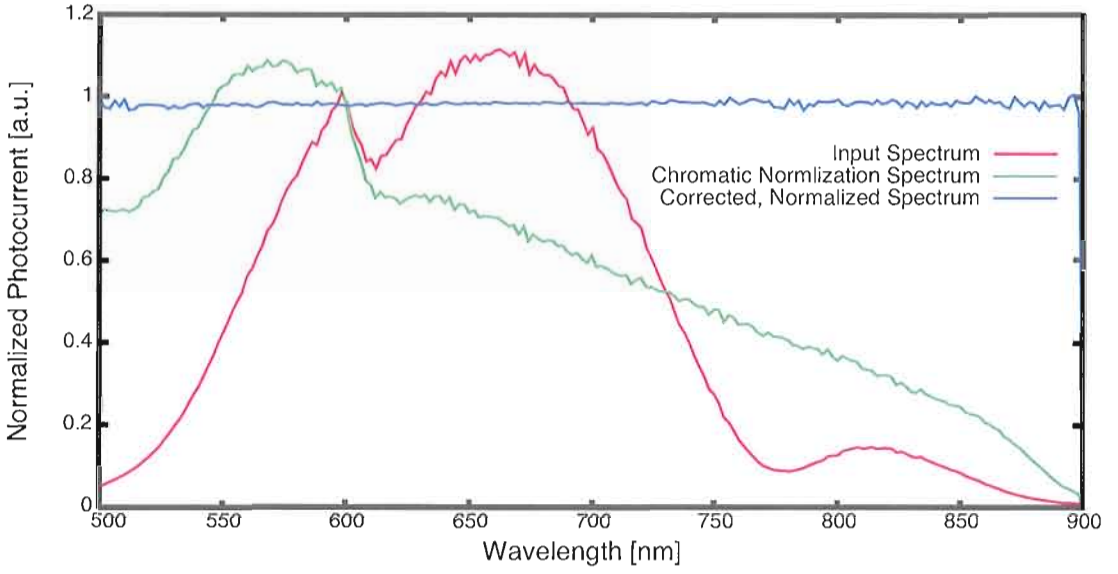

Figure 7.4. Normalization of input signal, and chromatic correction for non-identical detectors. The resulting signal has a noise level of less than 0.005 at 650 nm.

account for their individual spectral responsivities. We do this by collecting spectra without a sample in place. Division of the signal with this bright-field correction calibrates the chromatic differences between the PMT and the femtowatt photoreceiver. Such a chromatic correction spectrum can be seen in figure 7.4, along with a raw input spectrum and the resulting normalized signal.

AR Spectrometer Validation

Before beginning our discussion of zero-order AR transmission through periodic MDM coatings, we discuss several test cases. These are used to check the performance and alignment of the spectroscopy system. In figure 7.5(left) we plot the transmission through a 50 nm thick high-vacuum-deposited silver film. The plotted result demon-

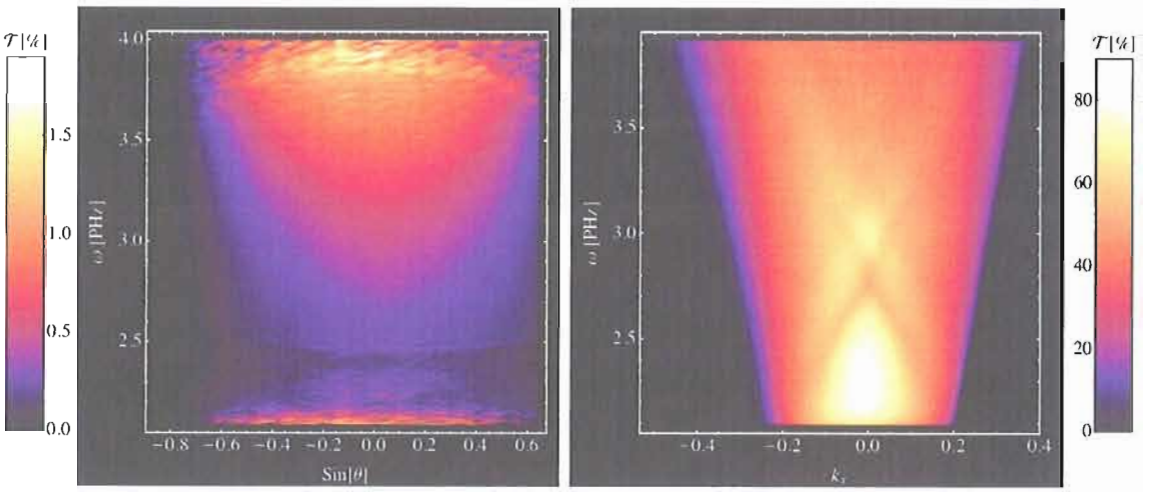

Figure 7.5. (left) Zero-order AR transmission through a flat 50 nm thick silver film. (right) Zero-order AR transmission through uncoated opal 83 ($< R > = 285$ nm).

strates the symmetry of the AR collection about the rotation origin of zero degrees (normal incidence). As shown in figure 7.3, negative and positive rotations respectively correspond to clockwise and counter-clockwise rotation of the sample stage. We can also see the low ($\mathcal{T} \sim 1.9\%$) transmission through this 50 nm think film. Below we will see, that the periodic MDM and DM structures we have manufactured in the previous chapter exhibit transmission enhancements on the order of 10 - 20 at 750 nm. The ripple structure in figure 7.5(left) is a result of noise from the low input intensities at the ends of our collection spectrum ($\sim$ 480 nm and 900 nm) and the high extinction of the flat film. The large variation in the noise level is due to the large variation of the input spectrum (cf. figure 7.4).

The left hand side of figure 7.5 shows the AR, zero-order transmission through an uncoated opal monolayer self-assembled from $r = 285$ nm silica spheres. The figure

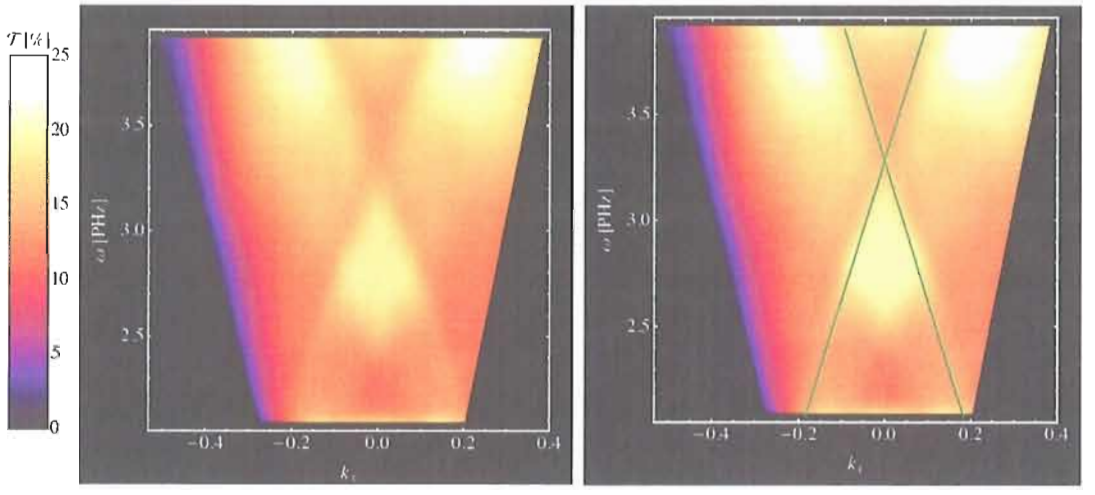

Figure 7.6. (left) Zero-order AR transmission through a polystyrene and silver coated monolayer opal 83 ($L = 100\,\text{nm}$, $T = 20\,\text{nm}$), (right) overlaid with the anomalous diffraction from the air-silver interface (green line).

shows the same rotational symmetry of the transmitted light as seen in the flat film case. A weak diffraction dip can also be seen centered at $\sim 2.8\,\text{PHz}$. This is the result of a highly ordered monolayer, and proves that we can use our system to investigate the angle resolved scattering from structures built from our self-assembled crystals.

In figure 7.6 we plot the collected zero-order transmission from an opal with a polystyrene and silver coating. The polystyrene coating is $\sim 100\,\text{nm}$ thick, and applied with the spin coating method discussed in chapter VI. The coating was spun from a 3% by weight, polystyrene-toluene solution at 5.2 krpm for 60s arriving at the estimated 100nm thick coating [112]. A 20 nm thick silver film was then evaporated on top of the polystyrene layer, under high vacuum. The results, plotted in figure 7.6, have one dominant feature. The symmetric "X" centered at 3.3 PHz (570 nm). This extinction feature is due to anomalous diffraction from the periodic, 2D, silver grat-

ing we have created. This so called, anomalous diffraction, occurs when a diffraction order (the first order in this case) reaches the grazing output angle of 90° [114]. This condition can be approximated from the grating equation, as the solution of:

$$\sin\theta_{in} = \frac{n_{out}}{n_{in}} - m\frac{\lambda_0}{n_{in}a} \quad m = (1, 2, 3, ...) \tag{VII.1}$$

where θ_{in} is the input angle, n_{in} (n_{out}) is the refractive index on the input (output) side of the grating, λ_0 is the free space wave length, and $a = 570\,\text{nm}$ is the first order periodicity of the grating (equal to the sphere diameter in this case). In the right-hand side of figure 7.6 we have potted the overlapping solution to equation (VII.1) on top of the transmitted spectra's extinction dip. Despite the crude approximation of the simple grating equation, it is obvious that the solution of (VII.1) coincides with the extinction dip, identifying it as anomalous diffraction.

Scattering from Silver Coated Opal Monolayers

We begin our discussion of MDM coated opal monolayers by first looking at the normal ($\theta_{in} = 0°$) transmission through a silver coated opal monolayer ($S = 70\,\text{nm}$). The zero-order ($\theta_{out} = 0°$) transmission for such a sample is shown in figure 7.7. As compared to the data taken from a 50 nm thick high vacuum evaporated silver film, there is a large transmission enhancement at 750 nm. From the spectral shape of the transmission, its spectral location of 750 nm, and the lack of a similar feature in the normal transmission through an uncoated opal monolayer (also plotted in figure 7.7)

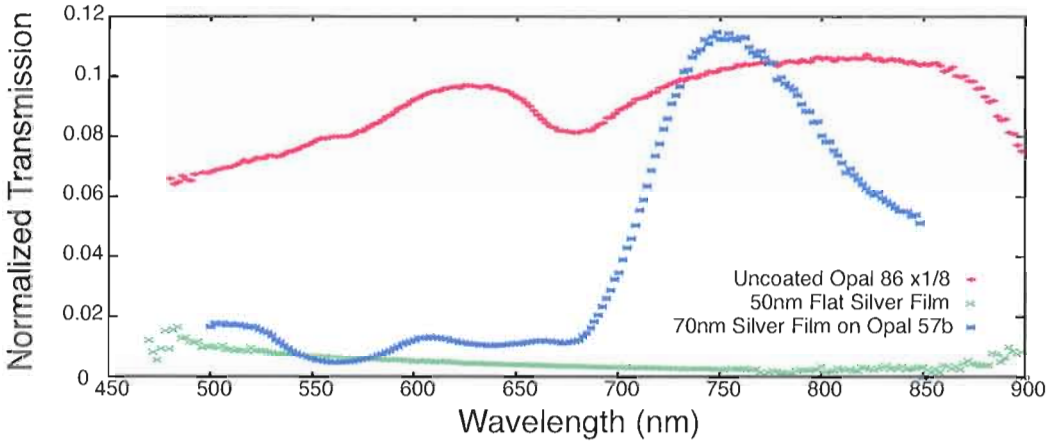

Figure 7.7. SPP enhanced zero-order transmission at 750 nm (2.51 PHz) from a silver coated ($S = 70$ nm) opal monolayer as described in the text. This is compared to an uncoated opal monolayer, and the transmission through a flat,50 nm thick, silver film. All spectra were taken with our AR spectrometer at normal incidence.

we conclude that this enhancement is the SPP enhanced transmission also found in subwavelength nano-hole arrays [19].

The existence of SPP enhanced transmission is a very reassuring sign that our manufacturing process supports the delocalized SPP modes. Enhanced transmission depends on the long range structure of a periodic array to coherently couple SPPs to radiating modes on both sides of the metal film. Our observation of enhanced transmission implies that our self-assembled monolayers are of sufficient ordered quality to support the coupling of the delocalized SPPs needed to generate SPP enhanced transmission through the subwavelength holes formed from the gaps between the spheres of the close-packed monolayer.

In figure 7.8, we present the AR, zero-order transmission from this silver coated

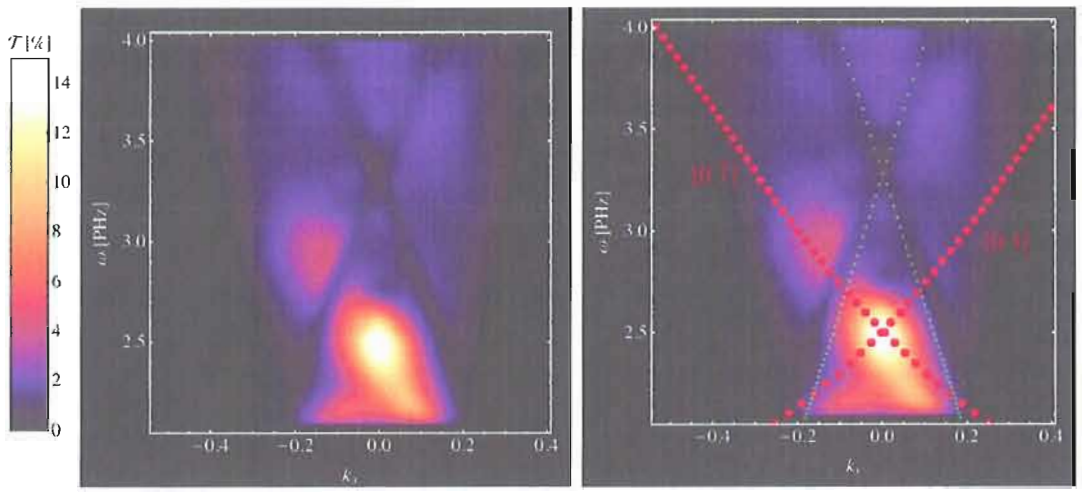

Figure 7.8. (left) AR zero-order transmission of opal 57B. A $S = 70\,\text{nm}$ silver coated opal. (right) The zero-order transmission with anomalous diffraction (green) and [0 1] silver-silica grating SPP dispersion (red) overlays.

opal monolayer. This figure shows the broad SPP enhanced transmission centered at 2.5 PHz (750 nm). In the right hand panel of figure 7.8 have plotted the same anomalous diffraction resonance as above. This accounts for the dark bands in the center of the transmission spectrum. In addition, we have plotted the first order dispersion band for a grating coupled SPP. As discussed in chapter II, the grating coupling method yields the following coupling condition for exciting SPPs on a hexagonal lattice (equation (II.7)):

$$\vec{k}_{spp} = \vec{k_{//}} + m_1\vec{G}_{\Gamma K} + m_2\vec{G}_{\Gamma M} \quad m_1, m_2 = (1, 2, 3...)$$

with $k_{//} = n_d k_0 \sin\theta_{in}$, $n_d = \sqrt{\varepsilon_d}$ is the index of refraction for the particular (air $n_d = 1$, silica $n_d = 1.45$, or polystyrene, $n_d = 1.59$) dielectric medium adjacent to the metal surface, $G_{\Gamma K} = 4\pi/3a$ and $G_{\Gamma M} = 2\pi/\sqrt{3}a$. The band plotted in figure 7.8(b)

is the first order ($m_2 = 1$) dispersion for the [0 1] ($\vec{G}_{\Gamma M}$) silver-silica SPP mode. As shown in figure 2.4, vertically-deposited, self-assembled crystals grow along the [1 1] real-space direction. Thus, as we rotate the crystal about the growth direction axis, $\hat{y}$ by an angle θ_{in}, we span the Γ–M high symmetry reciprocal lattice vector, $G_{\Gamma M}$. In figure 7.8(b) we see that the SPP enhanced transmission is broadly correlated with the Γ–M SPP band associated with the silver–silica interface plotted with the filled red circles. One may also observe that there is a strong asymmetry in the collected data with respect to the normal incidence (θ_{in}=0) mirror symmetry axis. This will be addressed in a later section.

MDM Coated Opal Monolayers

Having established that our crystal monolayers are of sufficient quality to support the grating coupling to SPPs, we now examine the effect of adding MDM layers to the surface of the ordered monolayer. Using the method discussed in chapter VI, we have created several MDM coatings with a variety of dielectric layer thicknesses. The details of the sample preparation can be found in table 7.1. The MDM layers have thickness of 125 nm, 140 nm, and 160 nm.

On the left hand side of figures 7.9, 7.10, and 7.11 we have plotted the zero-order AR transmission through the three MDM films. In the right hand panels we have

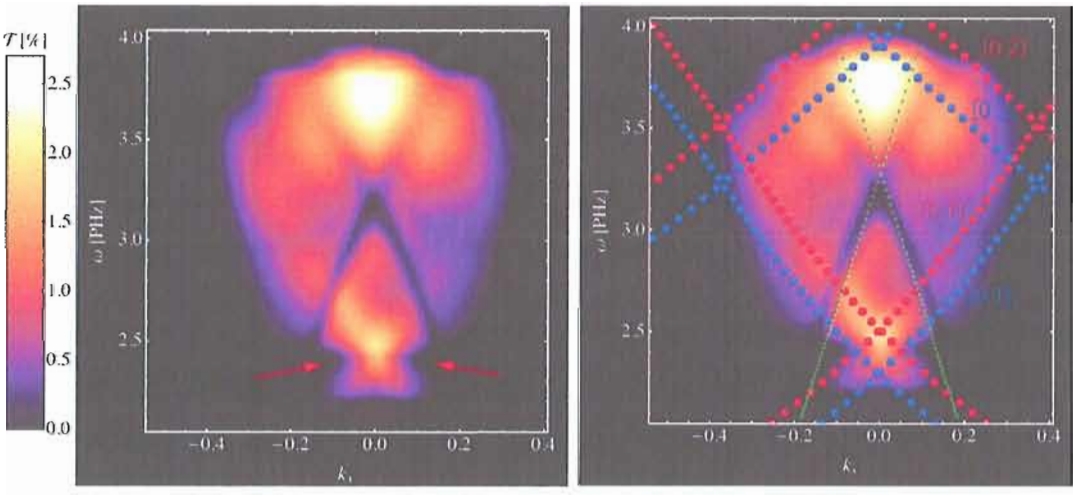

Figure 7.9. (left) AR zero-order transmission of opal 57A. An MDM coated opal with $L = 140$ nm. Red arrows indicate ISP extinction. (right) The zero-order transmission with [0 1] and [0 2] grating SPP dispersion bands for a silver-silica (red) and a silver-polystyrene interface (blue). The silver-air anomalous diffraction is plotted with green dots.

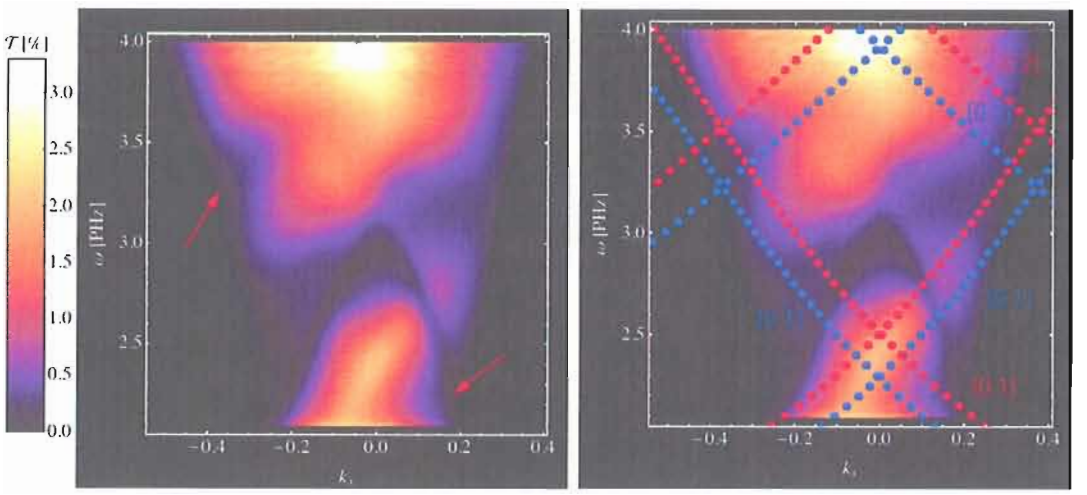

Figure 7.10. (left) AR zero-order transmission of opal 60. An MDM coated opal with $L = 160\,\text{nm}$. Red arrows indicate ISP extinction. (right) The zero-order transmission with [0 1] and [0 2] grating SPP dispersion bands for a silver-silica (red) and a silver-polystyrene interface (blue).

overlaid the first [0 1] and second order [0 2] dispersion bands for the silver-silica and silver-polystyrene interfaces. The ISP modes so heavily discussed in previous chapters roughly correspond to the excitation of SPPs on the polystyrene side of a periodically modulated silver-polystyrene film. From our work on MDM coated cylinders in chapter V, we know that a major effect found in our FEM simulations was the alteration of the SPP enhanced transmission due to the prerequisite excitation of ISP modes. Keeping this in mind, we note three features that suggest the excitation of ISP modes in figures 7.9, 7.10, and 7.11 .

The most obvious change from the single silver coating of figure 7.8 is the shift in the distribution of SPP enhanced transmission to include a broad branch centered at ($\omega = 3.7\,\text{PHz}$ (510 nm), $k_x = 0$). The over-plots of the [0 2] dispersion bands

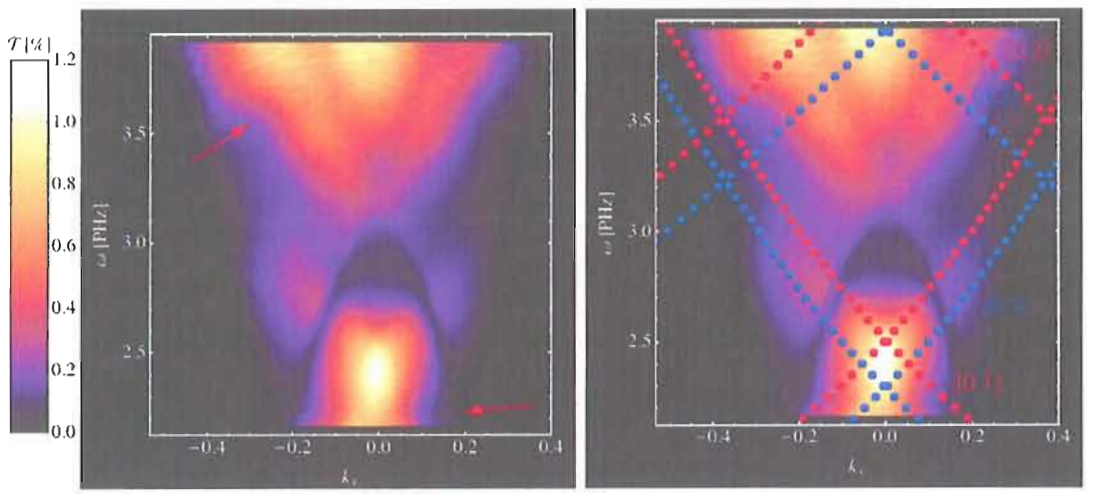

Figure 7.11. (left) AR zero-order transmission of opal 64. An MDM coated opal with $L = 125\,\text{nm}$. Red arrows indicate ISP extinction. (right) The zero-order transmission with [0 1] and [0 2] grating SPP dispersion bands for a silver-silica (red) and a silver-polystyrene interface (blue).

imply that this is due to the excitation of a second order ISP mode (the dotted blue line). This silver-polystyrene interface mode exists neither in figure 7.8, when there is no polystyrene layer, nor in figure 7.6, when there is only a single silver interface. We therefore conclude that the broad SPP enhanced transmission found centered at ($\omega = 3.7\,\text{PHz}$, $k_x = 0$) in all three MDM layers is due to the excitation of ISP modes in the polystyrene gap between the two silver films.

A second characteristic change, induced by the application of the second metal interface of the MDM coating, is the slight (but consistent) red-shift of the original SPP enhanced transmission centered at ($\omega = 2.5\,\text{PHz}$, $k_x = 0$). In figure 7.8 it is clear that this enhanced transmission overlaps with the first order [0 1] dispersion band of the silver-silica interface. In all of the MDM coated samples we see that the new

maximum of the SPP enhanced transmission has been red-shifted towards the first order silver-polystyrene [0 1] dispersion band. This is consistent with our simulations of chapter V. In those results, we found that the overlap of ISP bands with the SPP enhanced transmission redirected the transmission along (but blue shifted from) the ISP dispersion bands.

Finally, in figures 7.9, 7.10 (and weakly in figure 7.11) we note that, in addition to the apparent shifting of the SPP enhanced transmission, we see the increased extinction of the transmitted light corresponding to the [0 1] and [0 2] dispersion bands. (These are marked with red arrows.) Because of the strong correlation between the dispersion bands and the increased extinction, we conclude that they correspond to the excitation of ISP modes which are absorbing/scattering additional light out of beam. This is the most obvious in figure 7.9 with $L = 140\,\text{nm}$ and figure 7.10 with $L = 160\,\text{nm}$ becomes less pronounced in the thin dielectric spacer layer with $L = 125\,\text{nm}$ (figure 7.11). This suggests a change in the dispersion relation of the

Table 7.1. Geometry of opals presented in this study. The thicknesses L are estimates based on the calibration curve in figure 6.6.

Opal #	$< R >$ (nm)	S (nm)	L (nm)	T (nm)	% w.t. PS	Spin (krpm)
57A	285	50	140	20	4	0
57B	285	70	-	-	-	-
60	285	50	160	20	4	3.05
64	285	50	125	20	4	4.55
84	250	30	100	20	3	5.23
86	250	30	-	-	-	-

ISP with the dielectric layer thickness, and strong coherent coupling between the two metal interfaces.

Asymmetric Transmission

We now move onto a newly observed phenomenon. We have found, that for some silver-coated, self-assembled monolayers, the SPP enhanced transmission is asymmetric with respect to the mirror plane defined by the plane of normal incidence ($\theta_{in} = 0$). This was noted earlier in reference to figure 7.8. To test that this observation is an inherent property of our samples (and not an artifact of our AR spectroscopy system) we have measured the zero-order transmission with the sample in its original orientation ($\phi = 0$) and with the sample rotated 180° about the surface normal axis (cf. figure 7.3). This was done for two independent points on the sample, and with two different samples noted to have asymmetric SPP enhanced transmission. The results can be seen in figures 7.12 and 7.13.

In figures 7.12(a) and (b) we have plotted the asymmetric transmission of the previously examined silver coated opal from figure 7.8. The mirror symmetry between the $\phi = 0$ and $\phi = 180°$ in figures 7.12(a) and (b) is obvious when plotted they are plotted side-by-side. The mirrored SPP enhanced transmission happens, while the anomalous diffraction band remains symmetric. We conclude that the sample has inherent asymmetric transmission and that it is not a artifact of the measurement

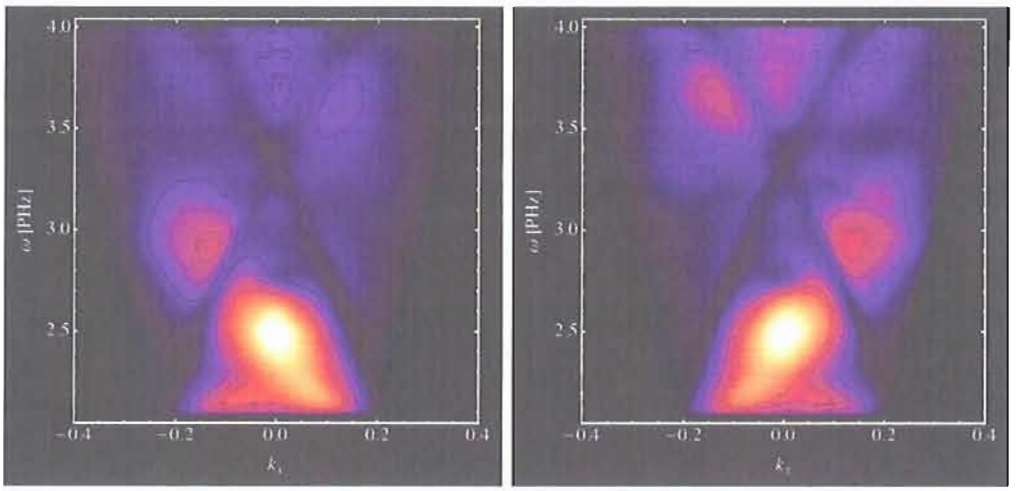

Figure 7.12. Asymmetric zero-order transmission from silver coated opal 57B. (left) $\phi = 0°$, (right) $\phi = 180°$. Both graphs are plotted on the same scale as figure 7.8.

process. The points measured were selected based on the visibility of their diffraction patterns with the alignment HeNe laser, but were otherwise independent. The selection of two independent points for these measurements proves the robustness of the observed asymmetric transmission. It implies that our samples are highly uniform and that the cause of the asymmetry likely originates from some systematic, global variation in the structure of the coated opal monolayer.

In figures 7.13(b) and (c) we show asymmetric SPP enhanced transmission through a second sample. This is an MDM coated opal monolayer with a new sphere size diameter ($a = 500\,\text{nm}$, $S = 30\,\text{nm}$, $L = 100\,\text{nm}$, $T = 20\,\text{nm}$: silver/polystyrene/silver). In figure 7.13(a) we the plot zero-order, AR transmission of a separately coated, silver opal monolayer ($a = 500\,\text{nm}$, $S = 30\,\text{nm}$). This new periodicity has moved the location of the SPP enhanced transmission to3.4 PHz. In comparison with figure 7.13(a),

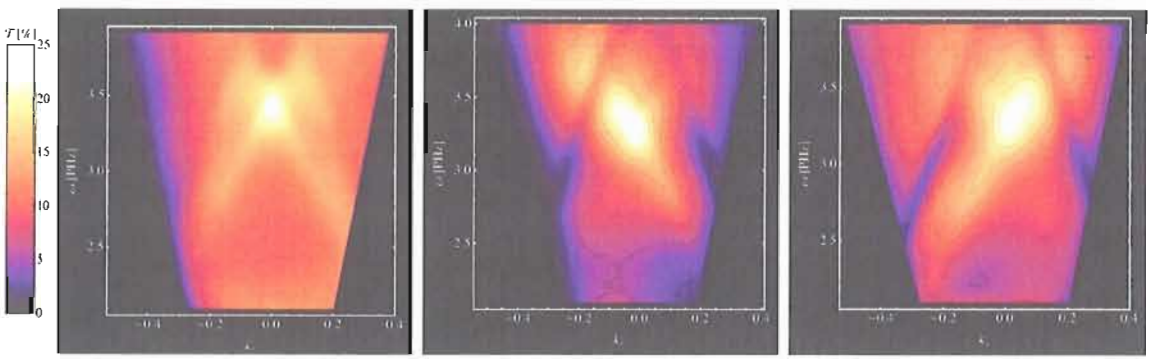

Figure 7.13. (a) Symmetric zero-order transmission through silver coated opal 86. Also plotted is the asymmetric zero-order transmission from MDM opal 84 for (b) $\phi = 0°$, and (c) $\phi = 180°$. The color scales of (b) and (c) are magnified by a factor of 5 with respect to (a).

the MDM coating has concentrated the SPP enhanced transmission along a broad dispersion band, and is highly asymmetric with respect to $\theta_{in} = 0$.

This asymmetric transmission is a highly intriguing observation. As far as we know, this directionally sensitive transmission effect has not been previously reported in relation to subwavelength hole arrays or other systems exhibiting SPP enhanced transmission. We do not know the exact origin of this effect, but given the spectra we have shown in this chapter we can intelligently speculate on its origins. Firstly, the spectra taken of uncoated and silver-polystyrene opals are symmetric with respect to the normal incidence plane, figures 7.5 and 7.6. This and the symmetric transmission through the flat silver film shows that neither the AR spectrometer, nor the uncoated opal monolayers induce an artificial asymmetry. Secondly, we have shown with figures 7.12 and 7.13(a) that the application of a high-vacuum-deposited silver film is a necessary, but insufficient condition for observing asymmetric transmission.

Lastly, we have shown that MDM layers can also exhibit this type of asymmetric transmission.

This evidence points a global, systematic structural asymmetry developing in some samples with the evaporation of silver onto the *bare* opal monolayer. We hypothesize that shadowing of the interstitial gaps of the close-packed monolayer is responsible for the observed asymmetric transmission

It is well known that SPP excitations are highly sensitive to the shape and orientation of nano-particles. Haes et al. have exploited this in their extremely sensitive biosensors [57, 115] by using nano-sphere lithography to create nano-particle arrays. Nanosphere lithography is the use of ordered spherical monolayers to mask the deposition of evaporated metal, creating periodic nano-particle arrays. Thus, it is the first two steps of our process, followed by the subsequent removal of the masking spheres. The shadowing properties of nano-sphere lithography have been extensively studied for the manipulation of the nano-particle geometry [116]. It has been shown that the shape and size of the resulting nano-particle arrays are sensitive to the orientation of the ordered sphere mask during the metal deposition step [117, 118].

The asymmetry that we observe occurs in some, but not all of our high-vacuum-deposited silver coatings. Due to the limitations of the Key high vacuum evaporator, the orientation of the monolayer substrates was not strictly controlled during the deposition process. The angle of the substrate with respect to the crystal growth direction was aligned by eye, and could have estimated errors on the order of 10°.

Since we have correlated the existence of the asymmetric transmission with the first silver film deposition process, and it is known that shadowing of the interstitial monolayer regions can cause changes to the size and shape of the nano-particles formed in the gaps, we conclude that it is this shadowing and the continued presence of the silver coated sphere monolayer that combine to result in the observed asymmetric transmission.

Conclusions

In this chapter we have brought together many of the ideas and results of the previous chapters. Using our understanding of ISP excitations developed in chapters III, IV and V we have interpreted the angle dependent transmission properties of the unique plasmonic surfaces engineered in chapter VI. With our home built, angle resolved spectroscopy system we have demonstrated the excitation of delocalized SPPs on opal monolayers, and found strong evidence of the free-space excitation of ISP modes in our MDM samples. Finally, we have reported the discovery of directionally asymmetric surface plasmon enhanced transmission. While the origin of the asymmetry is currently unknown, we have hypothesized that it is the result of angle based shadowing during the silver deposition onto a bare opal monolayer. This hypothesis can be verified through future quantitative study of angle controlled silver deposition.

CHAPTER VIII

CONCLUSIONS

In this thesis we have demonstrated how one can use far-field light scattering techniques combined with theoretical and computational analysis to investigate the near-field coherent coupling between surface plasmon polariton (SPP) excitations on spherical metal-dielectric-metal (MDM) interfaces separated by sub-wavelength distances. We were motivated to begin these investigations by asking how radiating SPPs coherently couple to other SPP modes on concentric metal shells. By developing the theoretical tools of chapter III we have answered this question and shown how SPPs on spherical metal shells separated by interior dielectric shell gaps couple to the external, radiating SPP modes. We have found how this near-field coupling leads to resonant level splitting, and how this band splitting impacts the far-field scattering of these multi-shelled metallodielectric particles. Through the process of answering the above question, we found several new questions to ask: Why does the level splitting found sometimes result in enhanced particle absorption and sometimes result in reduced particle scattering? Can the concepts of SPP-SPP resonant level splitting be applied to layered Bragg resonators, if those resonators are built from curvilinear components? Can we manufacture physical realizations of either multi-

layer spheres or multilayer plasmonic Bragg resonators? If so, how do we probe the far-field scattering of such systems in a logical and consistent manner?

In this work, we have endeavored to also answer these new questions. To accomplish this, we have developed new computational tools to calculate the electromagnetic field interaction with particles of arbitrary size and composition. This was a significant accomplishment, not because we developed any fundamentally new algorithms for the computation of scattering from a spherical particle, but because, at the time of its inception, no complete algorithm existed that was valid in our parameter range of large, absorbing, multi-shelled particles. Through careful selection from the work of several authors we developed our own framework for computing scattering from exactly these types of large, absorbing, multi-shelled particles. The speed and robustness of our algorithm has been essential in our investigations. It has allowed us to go beyond our original goal of simply computing the extinction-cross sections of multilayer plasmonic particles. It has prompted our investigation of the hybridized nature of coupled SPP field distributions, and facilitated answering some of the additional questions mentioned above.

Using these scattering computations, we have shown that coupling between SPP modes in MDM microspheres leads to resonant level splitting in their angular dispersion band diagrams. Additionally, by developing an analytical formulation for mode coupling between basic plasmonic elements (spheres and cavities) we have demonstrated how to mathematically isolate the important geometric parameters that con-

trol the interior-exterior surface plasmon coupling strength. Further, we have shown that, based on the strength of this coupling, we can tailor the extinction cross-sections of plasmonic particles with diameters comparable to the scattered wavelength. We found that, strong coupling to radiating modes leads to plasmonic-particle, forward scattering transparencies, and thus, demonstrated the reduction in the electromagnetic cross-sectional area of plasmonic particles by $\sim 50\%$. We also found that, weak coupling can be used to greatly enhance the particle's electromagnetic absorption. Because we are coupling SPP resonances, these transparency and absorption properties are spectrally tunable via the shells' geometric and material parameters. This allows the further spectral manipulation of the transparency window, and we have demonstrated tuning its central wavelength across the visible/NIR spectral region.

We've attempted to generalize some of the observations of MDM interior surface plasmon modes by looking at conformally-coated, periodically-modulated MDM nano-layers with finite element modeling (FEM) and experimental scattering spectroscopy. From our work with FEM simulations we found that interior surface plasmon analogs exist in periodically-modulated MDM surfaces, and that it is possible to couple directly to them with freely propagating waves. This was shown to potentially yield a new type of refractive index based sensor platform with a sensitivity twice as large as that found in modulated single interface sensors. Using these models we have also looked for analogies to the enhanced transmission properties of the above MDM spherical resonators. We have computationally explored the SPP enhanced

transmission effect found in modulated single metal films, and compared this to our MDM conformal nano-layers. Our simulations have shown that the excitation of the narrow-band interior surface plasmon mode becomes prerequisite for enhanced transmission, and thus, the interior surface plasmon modes supported by the coupled SPP modes of MDM surfaces serve to shape the response of SPP enhanced transmission.

To explore these findings experimentally we have developed a manufacturing process to create periodically-modulated MDM nano-layers from silica, silver and polymer components. Using the tools of evaporative self-assembly, high vacuum metal evaporation, and polymer film spin-coating, we've successfully developed plasmonic substrates similar to those studied computationally. Our method is simple, cheap (compared to comparable resolution methods such as e-beam lithography) and compatible with other planar manufacturing methods. SEM and AFM analysis shows that this produces high quality metal-dielectric-metal conformal coatings on top of a hexagonal-close-packed sphere substrate. The conformal, polystyrene layer, spin-coating method suffers from high sensitivity to point and line defects in the underlying crystal, but otherwise produces uniform layers with thicknesses in the $\sim 100\,\mathrm{nm}$ range. As investigated with angle-resolved spectroscopy, our silver-polystyrene-silver substrates appear to be of sufficient quality, to allow coupling to delocalized SPPs with the grating coupling method.

To test the plasmonic properties of these novel MDM substrates we have designed and built an angle-resolved spectroscopy system. The results of this work have demon-

strate strong evidence that interior surface plasmon modes in our engineered MDM substrates are excited by direct, free-space illumination. It has been also shown that the excitation of these interior surface plasmon modes significantly alters the SPP enhanced transmission. The demonstration of SPP enhanced transmission using monolayer opals as a substrate is new in-and-of itself, but we have further shown that, following the construction method in this work can result in samples with angularly asymmetric SPP enhanced transmission. This is a completely novel effect, not previously reported in the SPP enhanced transmission literature.

Future Work

As is the case for any well conducted line of research, in addition to answering questions, our investigations have inevitably resulted in generating new questions about SPPs and nano-structured metal surfaces. Among these, we put forth that, the most interesting future investigations should entail some or all of the following research directions.

In our work we briefly looked at the effect of adding more DM layers on the MDM particle scaffolding. Since our algorithm supports an arbitrary number of shells, further detailed investigations of many-shelled particles would be intriguing, and should generate interesting results. As an example we refer to the work of Smolyaninov et al. [48]. In this work they have used gold-PMMA concentric cylindrical shells to form

2D plasmonic cloaks for non-radiating SPP modes. It would be highly interesting to extend these ideas to 3D particles interacting with freely-propagating waves.

One of the questions that was asked above was, "is it possible to experimentally observe the plasmon enhanced transmission and absorption effects theoretically predicted in concentric spherical shells?" The technology has been developed to coat both silica and silver spheres with metal or dielectric coatings. However, it has not yet been used to generate the types of multiple concentric shells in the size ranges investigated in our work ($\sim 1\,\mu$m). Thus, from a materials science/surface chemistry point of view, synthesizing real world MDMd particles would be a very attractive line of research.

Additional experimental investigations should obviously include further study of MDM interior surface plasmon mediated transmission and the asymmetric SPP enhanced transmission. First, we have already demonstrated the strong effect that sphere periodicity has on the location of the SPP enhanced transmission. A systematic study of the ordered monolayer sphere size would be interesting in order to establish the relation between substrate periodicity and the central wavelength of the SPP enhanced transmission. Second, a quantitative study of asymmetric SPP enhanced transmission is needed. As mentioned in chapter VII, a systematic study of asymmetric transmission as a function the opal monolayer orientation during silver deposition is the most logical experiment to conduct.

There are also several improvements for our current MDM manufacturing process

that should be pursued in order to optimize the resulting substrates. The reduction of the ordered monolayer defect density is the single most important step. As outline in chapter VI, the creation of silica spheres with polydispersities less than two percent is most likely the needed ingredient for producing higher quality crystals with the IHSEA method we have developed.

Concluding Remarks

In summary, we have used many tools (theoretical, computational, experimental) from many different disciplines (physics, computer science, chemistry, material science) to study the interaction of light with sub-wavelength metallic features. We produced new computational tools that, in addition to being used here, will be of great utility to future investigations of multilayer plasmonic particles. Expanding on previous ideas of plasmon hybridization, we've developed an analytical formulation of SPP-SPP coupling that is applicable to spherical metal-dielectric interfaces of any size. We've developed a method for growing silica photonic crystals and engineering them into novel plasmonic substrates with the deposition of metal and polymer nano-scale layers. Finally, we've designed and built an angle-resolved spectroscopy system for optically studying the SPP-SPP coupling inherent in our periodic MDM layers, as proven with analogous 2D finite element simulations. We've used this spectrometer to study our manufactured hexagonally-patterned MDM nano-layers. This has lead

to the confirmation of some observations made with our finite element modeling and the discovery of angularly asymmetric SPP enhanced transmission.

To the author, this seems like quite a lot to accomplish in a few short years. However, it is dwarfed by the potential investigations that may be carried out in the future using the systems developed in this work. I have mentioned a few of them in the above section. But, this is by no means a complete list of potential research directions, and the possible applications of the plasmonic systems studied here were barely mentioned. Having reached the end of this work I cannot help but feel that, I am stopping just as many years of work are beginning to produce significant results. However, I believe that, this simply illustrates the large breadth of possibilities involved in exploring an essentially new field. I have every confidence that the tools we have developed here will continue to generate interesting and significant contributions to the fundamental understanding of subwavelength optics and plasmonics.

APPENDIX A

CALCULATION OF MULTILAYERED SPHERICAL PARTICLES

In this appendix we show how the modes equations of multi-shell spherical particles can be broken down into the coupled mode equations of the basic (sphere and cavity) elements that constitute its single interfaces. We start by solving Maxwell's Equations in curvilinear coordinates for a single, spherical scatterer. This is then expanded to multiple shells. The mode equations are then broken down into the mode equations derived during the expansion.

Single Spherical Scatter

We start with the solution to Maxwell's equations expanded in spherical harmonics. The interested reader can consult Bohren and Huffman for the initial separation of variable steps, and expansion of a plane wave in spherical coordinates [83].

Incident Field

The incident electric ($\vec{E}_i$) and magnetic $\vec{H}_i$ fields of a plane wave can be expanded in terms of spherical harmonics with the following result:

$$\begin{aligned} \vec{E}_i &= \vec{E}_o \sum_{n=1}^{\infty} i^n \frac{2n+1}{n(n+1)} \left(\vec{M}_{\mathrm{o1n}}{}^{(1)} - i\vec{N}_{\mathrm{e1n}}{}^{(1)} \right) \\ \vec{H}_i &= \vec{H}_o \sum_{n=1}^{\infty} i^n \frac{2n+1}{n(n+1)} \left(\vec{M}_{\mathrm{e1n}}{}^{(1)} + i\vec{N}_{\mathrm{o1n}}{}^{(1)} \right) \end{aligned} \tag{A.1}$$

This constitutes our input field that will be scattered from the single interface scatterer. E_0 is the incident field amplitude and $H_0 = -\frac{k_M}{\omega\mu_M}E_0$ is the strength o the incident magnetic field. The vector spherical harmonics, $N^{(j)}_{xxx}$, and $M^{(j)}_{xxx}$ in the above equations are defined by:

$$\begin{aligned}
\vec{M}^{(i)}_{\mathrm{o1n}} &= [0, \cos[\varphi]\pi_n(x)z_n^{(i)}(\rho), -\sin[\varphi]\tau_n(x)z_n^{(i)}(\rho)] \\
\vec{M}^{(i)}_{\mathrm{e1n}} &= [0, -\sin[\varphi]\pi_n(x)z_n^{(i)}(\rho), -\cos[\varphi]\tau_n(x)z_n^{(i)}(\rho)] \\
\vec{N}^{(i)}_{\mathrm{o1n}} &= [n(n+1)\sin[\varphi]\sin[\theta]\pi_n(x)\frac{z_n^{(i)}(\rho)}{\rho}, \sin[\varphi]\tau_n(x)\frac{\left[\rho z_n^{(i)}(\rho)\right]'}{\rho}, \cos[\varphi]\pi_n(x)\frac{\left[\rho z_n^{(i)}(\rho)\right]'}{\rho}] \\
\vec{N}^{(i)}_{\mathrm{e1n}} &= [n(n+1)\cos[\varphi]\sin[\theta]\pi_n(x)\frac{z_n^{(i)}(\rho)}{\rho}, \cos[\varphi]\tau_n(x)\frac{\left[\rho z_n^{(i)}(\rho)\right]'}{\rho}, -\sin[\varphi]\pi_n(x)\frac{\left[\rho z_n^{(i)}(\rho)\right]'}{\rho}]
\end{aligned} \tag{A.2}$$

with $x \equiv \cos[\theta]$, $\rho \equiv k_j \cdot r_i$, is the so called size parameter in the medium with permitivity ε_j bounded by the radius r_j the radial dependence is given by:

$$z_n^{(i)}(x) \equiv \begin{cases} j(x), & i = 1 \quad \text{Bessel function of the first kind} \\ h^{(1)}(x), & i = 3 \quad \text{Hankel function of the first kind} \end{cases}$$

Scattered Field

The resulting field after interacting with the particle can be separated into two pieces. The scattered field outside the particle, in the medium with permitivity ε_M, given by:

$$\begin{aligned}
\vec{E}_M &= \sum_{n=1}^{\infty} \vec{E}_n \frac{2n+1}{n(n+1)} \left((-b_n)\, \vec{M}_{\mathrm{o1n}}{}^{(3)} + a_n i \vec{N}_{\mathrm{e1n}}{}^{(3)} \right) \\
\vec{H}_M &= \sum_{n=1}^{\infty} \vec{H}_n \frac{2n+1}{n(n+1)} \left(a_n \vec{M}_{\mathrm{e1n}}{}^{(3)} + i b_n \vec{N}_{\mathrm{o1n}}{}^{(3)} \right)
\end{aligned} \tag{A.3}$$

The field inside the particle where the is permitivity ε_M, and its fields are given by:

$$\begin{aligned}\vec{E}_1 &= \sum_{n=1}^{\infty} \vec{E}_n \frac{2n+1}{n(n+1)} \left(c_n \vec{M}_{\mathrm{o1n}}{}^{(1)} - d_n i \vec{N}_{\mathrm{e1n}}{}^{(1)} \right) \\ \vec{H}_1 &= \sum_{n=1}^{\infty} \vec{H}_n \frac{2n+1}{n(n+1)} \left(a_n \vec{M}_{\mathrm{e1n}}{}^{(1)} + i b_n \vec{N}_{\mathrm{o1n}}{}^{(1)} \right)\end{aligned} \tag{A.4}$$

$$\begin{aligned}E_n &= E_0 i^n \frac{2n+1}{n(n+1)} \\ H_n &= -\frac{k_j}{\omega \mu_j} E_n\end{aligned} \tag{A.5}$$

with μ_j equal to the permeability in the jth medium

Boundary Conditions for Single Sphere

Continuity of the tangential fields produces the following boundary conditions evaluated at $r = r_1$:

$$\begin{aligned} E_{\mathrm{i}\theta} + E_{\mathrm{M}\theta} = E_{1\theta} \quad E_{\mathrm{i}\varphi} + E_{\mathrm{M}\varphi} = E_{1\varphi} \\ H_{\mathrm{i}\theta} + H_{\mathrm{M}\theta} = H_{1\theta} \quad H_{\mathrm{i}\theta} + H_{\mathrm{M}\theta} = H_{1\theta} \end{aligned} \tag{A.6}$$

These boundary conditions are calculated through the explicit expansion of the angular field components:

$$\begin{aligned} &E_{\mathrm{i}\theta} + E_{\mathrm{M}\theta} = E_{1\theta} \Rightarrow \\ &\hat{\theta} \cdot \sum_{n=1}^{\infty} E_n \left(\vec{M}_{\mathrm{o1n}}{}^{(1)} - i \vec{N}_{\mathrm{e1n}}{}^{(1)} - b_n \vec{M}_{\mathrm{o1n}}{}^{(3)} + a_n i \vec{N}_{\mathrm{e1n}}{}^{(3)} - c_n \vec{M}_{\mathrm{o1n}}{}^{(1)} + d_n i \vec{N}_{\mathrm{e1n}}{}^{(1)} \right) = 0 \end{aligned} \tag{A.7}$$

$$\begin{aligned} &H_{\mathrm{i}\theta} + H_{\mathrm{M}\theta} = H_{1\theta} \Rightarrow \\ &\hat{\theta} \cdot \sum_{n=1}^{\infty} E_n \left(-\frac{k_M}{\omega \mu} \left\{ \vec{M}_{\mathrm{e1n}}{}^{(1)} - i \vec{N}_{\mathrm{o1n}}{}^{(1)} \right\} \right. \\ &\left. + \frac{k_M}{\omega \mu} \left\{ a_n \vec{M}_{\mathrm{e1n}}{}^{(3)} + b_n i \vec{N}_{\mathrm{o1n}}{}^{(3)} \right\} + \frac{k_1}{\omega \mu} \left\{ d_n \vec{M}_{\mathrm{e1n}}{}^{(1)} + c_n i \vec{N}_{\mathrm{o1n}}{}^{(1)} \right\} \right) = 0 \end{aligned} \tag{A.8}$$

Using the identity $\sum_{n=1}^{\infty} A_n + B_n = 0 \Rightarrow A_n + B_n = 0 \; \forall \; n$, and the orthogonality of the vector spherical harmonics, we equate their coefficients we have the the following set of four linear equations for the field expansion coefficients a_n, $b_n, c_n,$ and d_n:

$$\begin{aligned}
0 = & -\frac{[k_M r_1 j_n(k_M r_1)]'}{k_M r_1} + a_n \frac{[k_M r_1 h_n{}^{(1)}(k_M r_1)]'}{k_M a} + d_n \frac{[k_1 r_1 j_n(k_1 r_1)]'}{k_1 r_1} \\
0 = & -\frac{k_M}{\omega\mu} j_n(k_M r_1) + \frac{k_M}{\omega\mu} a_n h_n{}^{(1)}(k_M r_1) + \frac{k_1}{\omega\mu_1} d_n j_n(k_1 r_1) \\
0 = & \; j_n(k_M r_1) - b_n h_n{}^{(1)}(k_M r_1) - c_n j_n(k_1 r_1) \\
0 = & \; \frac{-\frac{k_M}{\omega\mu}[k_M r_1 j_n(k_M r_1)]'}{k_M r_1} + \frac{k_M}{\omega\mu} \frac{b_n [k_M r_1 h_n{}^{(1)}(k_M r_1)]'}{k_M r_1} + \frac{k_1}{\omega\mu_1} \frac{c_n [k_1 r_1 j_n(k_1 r_1)]'}{k_1 r_1}
\end{aligned} \tag{A.9}$$

With redundant results for the $\hat{\varphi}$ equations. The above are two independent sets of equations. One equation for the transverse magnetic (TM) and one for the transverse electric (TE) solutions. The TM solution is given by:

$$\begin{aligned}
a_n \left[k_M r_1 h_n{}^{(1)}(k_M r_1)\right]' \frac{1}{k_M} + d_n [k_1 r_1 j_n(k_1 r_1)]' \frac{1}{k_1} &= [k_M r_1 j_n(k_M r_1)]' \frac{1}{k_M} \\
a_n \frac{k_M}{\mu} h_n{}^{(1)}(k_M r_1) + d_n \frac{k_1}{\mu_1} j_n(k_1 r_1) &= \frac{k_M}{\mu} j_n(k_M r_1)
\end{aligned} \tag{A.10}$$

which has the corresponding adjunct matrix:

$$\left(\begin{array}{cc|c}
h_n{}^{(1)}(k_M r_1) & \frac{\mu\, k_1}{\mu_1 k_M} j_n(k_1 r_1) & j_n(k_M r_1) \\
\left[k_M r_1 h_n{}^{(1)}(k_M r_1)\right]' \frac{k_1}{k_M} & [k_1 r_1 j_n(k_1 r_1)]' & [k_M r_1 j_n(k_M r_1)]'
\end{array}\right) \tag{A.11}$$

Which can be rewritten with the definitions of the Riccati-Bessel $\psi_n(x) \equiv x j_n(x)$ and Riccati-Hankel $\xi_n(x) \equiv x h_n^{(1)}(x)$ functions:

$$\left(\begin{array}{cc|c}
h_n{}^{(1)}(k_M r_1) & \frac{\mu\, k_1}{\mu_1 k_M} j_n(k_1 r_1) & j_n(k_M r_1) \\
\xi_n'(k_M r_1) \frac{k_1}{k_M} & \psi_n'(k_1 r_1) & \psi_n'(k_M r_1)
\end{array}\right) \tag{A.12}$$

The equivalent TE equations are given by:

$$\begin{aligned} b_n \frac{1}{\mu}\left[kr_1 {h_n}^{(1)}(k_M r_1)\right]' + c_n \frac{1}{\mu_1}\left[k_1 r_1 j_n(k_1 r_1)\right]' &= \frac{1}{\mu}\left[k_M r_1 j_n(k_M r_1)\right]' \\ b_n {h_n}^{(1)}(k_M r_1) + c_n j_n(k_1 r_1) &= j_n(k_M r_1) \end{aligned} \tag{A.13}$$

$$\left(\begin{array}{cc|c} {h_n}^{(1)}(k_M r_1) & \frac{\mu\, k_1}{\mu_1 k_M} j_n(k_1 r_1) & j_n(k_M r_1) \\ \mu\left[k_M r_1 {h_n}^{(1)}(k_M r_1)\right]' & \mu_1\left[k_M r_1 j_n(k_1 r_1)\right]' & \mu\left[k_M r_1 j_n(k_M r_1)\right]' \end{array}\right) \tag{A.14}$$

$$\left(\begin{array}{cc|c} {h_n}^{(1)}(k_M r_1) & \frac{\mu\, k_1}{\mu_1 k_M} j_n(k_1 r_1) & j_n(k_M r_1) \\ \mu\xi_n'(k_M r_1) & \mu_1 \psi_n'(k_1 r_1) & \mu\psi_n'(k_M r_1) \end{array}\right) \tag{A.15}$$

Using Cramer's Rule for solving systems of linear equations we can write down the solutions for the expansion coefficients for the scattered a_n, b_n and, internal c_n, d_n fields in terms of determinants:

$$a_n = \frac{\begin{vmatrix} j_n(k_M r_1) & \frac{\mu\, k_1}{\mu_1 k_M} j_n(k_1 r_1) \\ \left[k_M r_1 j_n(k_M r_1)\right]' & \left[k_1 r_1 j_n(k_1 r_1)\right] \end{vmatrix}}{\begin{vmatrix} {h_n}^{(1)}(k_M r_1) & \frac{\mu\, k_1}{\mu_1 k_M} j_n(k_1 r_1) \\ \left[k_M r_1 {h_n}^{(1)}(k_M r_1)\right]' \frac{k_1}{k_M} & \left[k_1 r_1 j_n(k_1 r_1)\right]' \end{vmatrix}} \tag{A.16}$$

$$d_n = \frac{\begin{vmatrix} {h_n}^{(1)}(k_M r_1) & j_n(k_M r_1) \\ \left[k_M r_1 {h_n}^{(1)}(k_M r_1)\right]' \frac{k_1}{k_M} & \left[k_M r_1 j_n(k_M r_1)\right]' \end{vmatrix}}{\begin{vmatrix} {h_n}^{(1)}(k_M r_1) & \frac{\mu\, k_1}{\mu_1 k_M} j_n(k_1 r_1) \\ \left[k_M r_1 {h_n}^{(1)}(k_M r_1)\right]' \frac{k_1}{k_M} & \left[k_1 r_1 j_n(k_1 r_1)\right]' \end{vmatrix}} \tag{A.17}$$

$$b_n = \frac{\begin{vmatrix} j_n(k_M r_1) & \frac{\mu\, k_1}{\mu_1 k_M} j_n(k_1 r_1) \\ \mu\left[k_M r_1 j_n(k_M r_1)\right]' & \mu_1\left[k_1 r_1 j_n(k_1 r_1)\right]' \end{vmatrix}}{\begin{vmatrix} h_n^{(1)}(k_M r_1) & \frac{\mu\, k_1}{\mu_1 k_M} j_n(k_1 r_1) \\ \mu\left[k_M r_1 h_n^{(1)}(k_M r_1)\right]' & \mu_1\left[k_1 r_1 j_n(k_1 r_1)\right]' \end{vmatrix}} \tag{A.18}$$

$$c_n = \frac{\begin{vmatrix} h_n^{(1)}(k_M r_1) & j_n(k_M r_1) \\ \mu\left[k_M r_1 h_n^{(1)}(k_M r_1)\right]' & \mu\left[k_M r_1 j_n(k_M r_1)\right]' \end{vmatrix}}{\begin{vmatrix} h_n^{(1)}(k_M r_1) & \frac{\mu\, k_1}{\mu_1 k_M} j_n(k_1 r_1) \\ \mu\left[k_M r_1 h_n^{(1)}(k_M r_1)\right]' & \mu_1\left[k_1 r_1 j_n(k_1 r_1)\right]' \end{vmatrix}} \tag{A.19}$$

The particle posses a resonance when the denominators of equations (A.16–A.19) go to zero. For the TM case (a_n, d_n) we define the mode equation for resonant excitation as given by the determinant:

$$\det[U_{\mathrm{Md}}] \equiv \begin{vmatrix} h_n^{(1)}(k_M r_1) & \frac{k_1}{k_M} j_n(k_1 r_1) \\ \left[k_M r_1 h_n^{(1)}(k_M r_1)\right]' \frac{k_1}{k_M} & \left[k_1 r_1 j_n(k_1 r_1)\right]' \end{vmatrix} \tag{A.20}$$

which can be rewritten as:

$$det[U_{\mathrm{Md}}] = \begin{vmatrix} h_n^{(1)}(k_M r_1)\, k_M & j_n(k_1 r_1)\, k_1 \\ \xi_n'(k_M r_1)/k_M & \psi_n'(k_1 r_1)/k_1 \end{vmatrix} \tag{A.21}$$

MDm Cavities and DMd Core-Shell Particles

When we introduce an extra interface to form an MDm cavity or a DMd core-shell particle and additional set of boundary conditions is introduced into the problem. This is the only change. This change is accounted for by introducing an additional set of fields with in ward and outward propagating waves, given by:

$$\vec{E}_2 = \sum_{n=1}^{\infty} \vec{E}_n \frac{2n+1}{n(n+1)} \left((-g_n) \vec{M}_{\mathrm{o1n}}{}^{(3)} + f_n i \vec{N}_{\mathrm{e1n}}{}^{(3)} \right) \tag{A.22}$$

$$\vec{H}_2 = \sum_{n=1}^{\infty} \vec{H}_n \frac{2n+1}{n(n+1)} \left(f_n \vec{M}_{\mathrm{e1n}}{}^{(3)} + i g_n \vec{N}_{\mathrm{o1n}}{}^{(3)} \right) \tag{A.23}$$

Continuity of the tangential fields produces the previous boundary conditions evaluated at $r = r_2$:

$$\begin{aligned} E_{\mathrm{i}\theta} + E_{\mathrm{M}\theta} &= E_{2\theta} \\ E_{\mathrm{i}\varphi} + E_{\mathrm{M}\varphi} &= E_{2\varphi} \\ H_{\mathrm{i}\theta} + H_{\mathrm{M}\theta} &= H_{2\theta} \\ H_{\mathrm{i}\varphi} + H_{\mathrm{M}\varphi} &= H_{2\varphi} \end{aligned} \tag{A.24}$$

and continuity of the tangential fields produces the new boundary conditions evaluated at $r = r_1$:

$$\begin{aligned} E_{2\theta} &= E_{1\theta} \\ E_{2\varphi} &= E_{1\varphi} \\ H_{2\theta} &= H_{1\theta} \\ H_{2\varphi} &= H_{1\varphi} \end{aligned} \tag{A.25}$$

Thought the same separation of variables as above, we once again arrive at two orthogonal, TM and TE solutions. In the context of SPPs we are only interested in the TM resonant modes. The adjunct matrix for the TM solutions is given by:

$$\left(\begin{array}{cccc|c} {h_n}^{(1)}(k_M r_2)\,k_M & j_n(k_2 r_2)\,k_2 & h_n(k_2 r_2)\,k_M & 0 & j_n(k_M r_2)\,k_M \\ \xi_n'(k_M r_2)/k_M & \psi_n'(k_2 r_2)/k_2 & \xi_n'(k_2 r_2)/k_2 & 0 & \psi_n'(k_M r_2)/k_M \\ 0 & {h_n}^{(1)}(k_2 r_1)\,k_2 & j_n(k_2 r_1)\,k_2 & j_n(k_1 r_1)\,k_1 & 0 \\ 0 & \xi_n'(k_2 r_1)/k_2 & \psi_n'(k_2 r_1)/k_2 & \psi_n'(k_1 r_1)/k_1 & 0 \end{array}\right) \tag{A.26}$$

From which we can once again extract the mode equation for TM mode excitation using Cramer's Rule:

$$\det[U_{\mathrm{MDm}}] \equiv \left|\begin{array}{cccc} {h_n}^{(1)}(k_M r_2)\,k_M & j_n(k_2 r_2)\,k_2 & h_n(k_2 r_2)\,k_M & 0 \\ \xi_n'(k_M r_2)/k_M & \psi_n'(k_2 r_2)/k_2 & \xi_n'(k_2 r_2)/k_2 & 0 \\ 0 & {h_n}^{(1)}(k_2 r_1)\,k_2 & j_n(k_2 r_1)\,k_2 & j_n(k_1 r_1)\,k_1 \\ 0 & \xi_n'(k_2 r_1)/k_2 & \psi_n'(k_2 r_1)/k_2 & \psi_n'(k_1 r_1)/k_1 \end{array}\right| \tag{A.27}$$

MDMd TM Mode Equation

If you are astute you can extract the changes from equation (A.21) to equation (A.27)

and simply write down the mode equation for the addition of another interface. The mode equation for the MDMd case is given by:

$$\det[U_{\mathrm{MDMd}}] \equiv$$

$$\begin{vmatrix}
h_n{}^{(1)}(k_M r_3)\,k_M & j_n(k_3 r_3)\,k_3 & h_n{}^{(1)}(k_3 r_3)\,k_3 & 0 & 0 & 0 \\
\xi_n'(k_M r_3)/k_M & \psi_n'(k_3 r_3)/k_3 & \xi_n'(k_3 r_3)/k_3 & 0 & 0 & 0 \\
0 & j_n(k_3 r_2)\,k_3 & h_n{}^{(1)}(k_3 r_2)\,k_3 & j_n(k_2 r_2)\,k_2 & h_n(k_2 r_2)\,k_M & 0 \\
0 & \psi_n'(k_3 r_2)/k_3 & \xi_n'(k_3 r_2)/k_3 & \psi_n'(k_2 r_2)/k_2 & \xi_n'(k_2 r_2)/k_2 & 0 \\
0 & 0 & 0 & h_n{}^{(1)}(k_2 r_1)\,k_2 & j_n(k_2 r_1)\,k_2 & j_n(k_1 r_1)\,k_1 \\
0 & 0 & 0 & \xi_n'(k_2 r_1)/k_2 & \psi_n'(k_2 r_1)/k_2 & \psi_n'(k_1 r_1)/k_1
\end{vmatrix} \tag{A.28}$$

Equation (A.28) can be expanded to reveal the component coupling in the following manner. We start by evaluating (A.28) by minors:

$$U_{\mathrm{MDMd}} = \xi_n'(k_M r_3)\,\mathbb{A} - h_n{}^{(1)}(k_M r_3)\,\mathbb{B} \tag{A.29}$$

where

$$\mathbb{A} \equiv \begin{vmatrix}
j_n(k_3 r_3)\,k_3 & h_n{}^{(1)}(k_3 r_3)\,k_3 & 0 & 0 & 0 \\
j_n(k_3 r_2)\,k_3 & h_n{}^{(1)}(k_3 r_2)\,k_3 & j_n(k_2 r_2)\,k_2 & h_n(k_2 r_2)\,k_M & 0 \\
\psi_n'(k_3 r_2)/k_3 & \xi_n'(k_3 r_2)/k_3 & \psi_n'(k_2 r_2)/k_2 & \xi_n'(k_2 r_2)/k_2 & 0 \\
0 & 0 & h_n{}^{(1)}(k_2 r_1)\,k_2 & j_n(k_2 r_1)\,k_2 & j_n(k_1 r_1)\,k_1 \\
0 & 0 & \xi_n'(k_2 r_1)/k_2 & \psi_n'(k_2 r_1)/k_2 & \psi_n'(k_1 r_1)/k_1
\end{vmatrix} \tag{A.30}$$

and

$$\mathbb{B} \equiv \begin{vmatrix} \psi_n'(k_3 r_3)/k_3 & \xi_n'(k_3 r_3)/k_3 & 0 & 0 & 0 \\ j_n(k_3 r_2)\, k_3 & h_n{}^{(1)}(k_3 r_2)\, k_3 & j_n(k_2 r_2)\, k_2 & h_n(k_2 r_2)\, k_M & 0 \\ \psi_n'(k_3 r_2)/k_3 & \xi_n'(k_3 r_2)/k_3 & \psi_n'(k_2 r_2)/k_2 & \xi_n'(k_2 r_2)/k_2 & 0 \\ 0 & 0 & h_n{}^{(1)}(k_2 r_1)\, k_2 & j_n(k_2 r_1)\, k_2 & j_n(k_1 r_1)\, k_1 \\ 0 & 0 & \xi_n'(k_2 r_1)/k_2 & \psi_n'(k_2 r_1)/k_2 & \psi_n'(k_1 r_1)/k_1 \end{vmatrix} \tag{A.31}$$

A second evaluation by minors gives us the equations:

$$\mathbb{A} = j_n(k_3 r_3)\, k_3 \mathbb{C} - h_n{}^{(1)}(k_3 r_3)\, k_3 \mathbb{D} \tag{A.32}$$

$$\mathbb{B} = \psi_n'(k_3 r_3)/k_3 \mathbb{C} - \xi_n'(k_3 r_3)/k_3 \mathbb{D} \tag{A.33}$$

where

$$\mathbb{C} = \begin{vmatrix} h_n{}^{(1)}(k_3 r_2)\, k_3 & j_n(k_2 r_2)\, k_2 & h_n(k_2 r_2)\, k_M & 0 \\ \xi_n'(k_3 r_2)/k_3 & \psi_n'(k_2 r_2)/k_2 & \xi_n'(k_2 r_2)/k_2 & 0 \\ 0 & h_n{}^{(1)}(k_2 r_1)\, k_2 & j_n(k_2 r_1)\, k_2 & j_n(k_1 r_1)\, k_1 \\ 0 & \xi_n'(k_2 r_1)/k_2 & \psi_n'(k_2 r_1)/k_2 & \psi_n'(k_1 r_1)/k_1 \end{vmatrix} \tag{A.34}$$

and

$$\mathbb{D} = \begin{vmatrix} j_n(k_3 r_2)\, k_3 & j_n(k_2 r_2)\, k_2 & h_n(k_2 r_2)\, k_M & 0 \\ \psi_n'(k_3 r_2)/k_3 & \psi_n'(k_2 r_2)/k_2 & \xi_n'(k_2 r_2)/k_2 & 0 \\ 0 & h_n{}^{(1)}(k_2 r_1)\, k_2 & j_n(k_2 r_1)\, k_2 & j_n(k_1 r_1)\, k_1 \\ 0 & \xi_n'(k_2 r_1)/k_2 & \psi_n'(k_2 r_1)/k_2 & \psi_n'(k_1 r_1)/k_1 \end{vmatrix} \tag{A.35}$$

Thus, equation (A.28) can be written out as:

$$\begin{aligned}\det[U_{\mathrm{MDMd}}] = & \\ & \xi_n'(k_M r_3)\left[j_n(k_3 r_3)\,k_3\mathbb{C} - {h_n}^{(1)}(k_3 r_3)\,k_3\mathbb{D}\right] \\ & -{h_n}^{(1)}(k_M r_3)\left[\psi_n'(k_3 r_3)/k_3\mathbb{C} - \xi_n'(k_3 r_3)/k_3\mathbb{D}\right] \\ & = \left[\xi_n'(k_M r_3)\,j_n(k_3 r_3)\,k_3 - {h_n}^{(1)}(k_M r_3)\,\psi_n'(k_3 r_3)/k_3\right]\mathbb{C} - \\ & \left[\xi_n'(k_M r_3)\,{h_n}^{(1)}(k_3 r_3)\,k_3 - {h_n}^{(1)}(k_M r_3)\,\xi_n'(k_3 r_3)/k_3\right]\mathbb{D}\end{aligned} \tag{A.36}$$

This equation can be written as the following determinate:

$$\det[U_{\mathrm{MDMd}}] = \left|\begin{array}{cc} \left|\begin{array}{cc} \xi_n'(k_M r_3) & {h_n}^{(1)}(k_M r_3) \\ \psi_n'(k_3 r_3)/k_3 & j_n(k_3 r_3)\,k_3 \end{array}\right| & \left|\begin{array}{cc} \xi_n'(k_M r_3) & {h_n}^{(1)}(k_M r_3) \\ {h_n}^{(1)}(k_3 r_3)\,k_3 & \xi_n'(k_3 r_3)/k_3 \end{array}\right| \\ \mathbb{D} & \mathbb{C} \end{array}\right| \tag{A.37}$$

And at this point we recognize that, from equation (A.21):

$$\det[U_{\mathrm{Md}}] = \left|\begin{array}{cc} \xi_n'(k_M r_3) & {h_n}^{(1)}(k_M r_3) \\ \psi_n'(k_3 r_3)/k_3 & j_n(k_3 r_3)\,k_3 \end{array}\right| \tag{A.38}$$

and that from equation equation (A.27):

$$\det[U_{\mathrm{MDm}}] = \mathbb{C} = \left|\begin{array}{cccc} {h_n}^{(1)}(k_3 r_2)\,k_3 & j_n(k_2 r_2)\,k_2 & h_n(k_2 r_2)\,k_M & 0 \\ \xi_n'(k_3 r_2)/k_3 & \psi_n'(k_2 r_2)/k_2 & \xi_n'(k_2 r_2)/k_2 & 0 \\ 0 & {h_n}^{(1)}(k_2 r_1)\,k_2 & j_n(k_2 r_1)\,k_2 & j_n(k_1 r_1)\,k_1 \\ 0 & \xi_n'(k_2 r_1)/k_2 & \psi_n'(k_2 r_1)/k_2 & \psi_n'(k_1 r_1)/k_1 \end{array}\right| \tag{A.39}$$

with the definitions:

$$\det[V_{\mathrm{Md}}] \equiv \left|\begin{array}{cc} \xi_n'(k_M r_3) & {h_n}^{(1)}(k_M r_3) \\ {h_n}^{(1)}(k_3 r_3)\,k_3 & \xi_n'(k_3 r_3)/k_3 \end{array}\right| \tag{A.40}$$

and

$$\det[W_{\mathrm{MDm}}] \equiv \mathbb{D} = \begin{vmatrix} j_n(k_3 r_2)\, k_3 & j_n(k_2 r_2)\, k_2 & h_n(k_2 r_2)\, k_M & 0 \\ \psi_n'(k_3 r_2)/k_3 & \psi_n'(k_2 r_2)/k_2 & \xi_n'(k_2 r_2)/k_2 & 0 \\ 0 & h_n{}^{(1)}(k_2 r_1)\, k_2 & j_n(k_2 r_1)\, k_2 & j_n(k_1 r_1)\, k_1 \\ 0 & \xi_n'(k_2 r_1)/k_2 & \psi_n'(k_2 r_1)/k_2 & \psi_n'(k_1 r_1)/k_1 \end{vmatrix} \tag{A.41}$$

We can finally rewrite equation (A.28) as:

$$\det[U_{\mathrm{MDMd}}] = \begin{vmatrix} |U_{\mathrm{Md}}| & |V_{\mathrm{Md}}| \\ |W_{\mathrm{MDm}}| & |U_{\mathrm{MDm}}| \end{vmatrix} \tag{A.42}$$

This shows that the on-diagonal elements are the uncoupled modes of the single sphere (U_{Md}) and the MDm cavity (U_{MDm}) coupled through the off-diagonal elements V_{MDm} and V_{Md}.

Asymptotic Expansion of V_{Md}

$$\det[V_{\mathrm{Md}}] \equiv \begin{vmatrix} \eta_m \xi'(k_d r_3) & h_n{}^{(1)}(k_m r_3) \\ h_n{}^{(1)}(k_d r_3) & \xi'(k_m r_3) \end{vmatrix} = - \begin{vmatrix} \eta_m \xi'(k_d r_3) & \xi'(k_m r_3) \\ h_n{}^{(1)}(k_d r_3) & h_n{}^{(1)}(k_m r_3) \end{vmatrix} \tag{A.43}$$

$$\begin{aligned} h_n{}^{(1)}(x) &\sim i^{-n-1} \frac{e^{ix}}{x} \\ \xi_n'(x) &\sim i^{-n} e^{ix} \end{aligned} \tag{A.44}$$

$$\det[V_{\mathrm{Md}}] \sim \frac{i^{-2n}}{k_0 r_3} \begin{vmatrix} \eta_m e^{ik_d r_3} & e^{ik_m r_3} \\ e^{ik_d r_3}/k_d r_3 & e^{ik_m r_3}/k_m r_3 \end{vmatrix} \tag{A.45}$$

$n_d = 1$, $n_m = \sqrt{\epsilon_m(\omega)} \equiv n'_m + in''_m$, $k_0 = \omega/c$, $k_x \equiv n_x k_0 \Rightarrow k_m = k'_m + ik''_m$,

$$\begin{aligned}
\det\left[V_{\mathrm{Md}}\right] \sim & \frac{i^{-2n+1}}{k_0 r_3} \begin{vmatrix} \eta_m e^{ik_0 r_3} & e^{in_m r_3} \\ e^{ik_0 r_3} & e^{in_m r_3}/n_m \end{vmatrix} \\
&= \frac{i^{-2n+1}}{k_0 r_3} e^{ik_0 r_3} e^{in_m k_0 r_3} \begin{vmatrix} \eta_m & 1 \\ 1 & \dfrac{1}{n_m} \end{vmatrix} \\
&= \frac{i(-1)^n}{k_0 r_3} e^{ik_0 r_3 (1+n'_m)} \left(n_m - 1\right) e^{-n_m'' k_0 r_3}
\end{aligned} \tag{A.46}$$

$r_3 = S + L + T$

$\Rightarrow$

$$\det\left[V_{\mathrm{Md}}\right] \sim \left\{(-1)^n \left(n_m - 1\right) e^{i(k_0 + k_m)} e^{i(k_0 + k'_m)T} / k_0 (S + L + T)\right\} e^{-k_m'' T} \tag{A.47}$$

APPENDIX B

RECURSIVE CALCULATION OF SPHERICAL SCATTERING

In this appendix we briefly outline the recursive approach to calculating the scattering from an arbitrary, L shelled scatterer. We can write the fields in the ℓth medium as

$$\begin{aligned}\vec{E}_L &= \sum_{n=1}^{\infty} \vec{E}_n \frac{2n+1}{n(n+1)} \left(\left(-b_n{}^{\ell}\right) \vec{M}_{\mathrm{o1n}}{}^{(3)} + a_n{}^{\ell} i\vec{N}_{\mathrm{e1n}}{}^{(3)} + c_n{}^{\ell} \vec{M}_{\mathrm{o1n}}{}^{(1)} - d_n{}^{\ell} i\vec{N}_{\mathrm{e1n}}{}^{(1)} \right) \\ \vec{H}_L &= \sum_{n=1}^{\infty} \vec{H}_n \frac{2n+1}{n(n+1)} \left(a_n{}^{\ell} \vec{M}_{\mathrm{e1n}}{}^{(3)} + ib_n{}^{\ell} \vec{N}_{\mathrm{o1n}}{}^{(3)} + a_n{}^{\ell} \vec{M}_{\mathrm{e1n}}{}^{(1)} + ib_n{}^{\ell} \vec{N}_{\mathrm{o1n}}{}^{(1)} \right)\end{aligned} \tag{B.1}$$

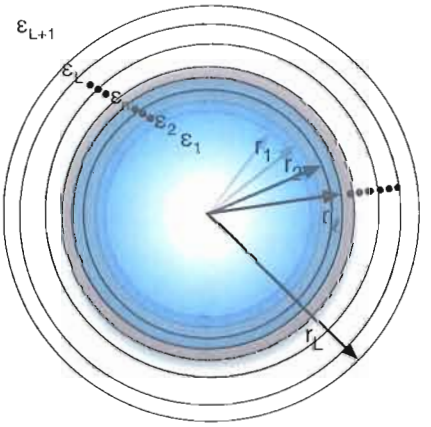

Figure B.1.. Geometry and labels of an L shell system.

Using the same approach as in appendix A, the orthogonality of the vector spherical harmonics yield a set of $2L$ linear equations:

$$
\begin{aligned}
d_n{}^{(\ell+1)} m_{\ell+1}\psi_n(m_{\ell+1}x_\ell) - a_n{}^{(\ell+1)} m_{\ell+1}\xi_n(m_{\ell+1}x_\ell) - d_n{}^{(\ell)} m_\ell\psi_n(m_\ell x_\ell) + a_n{}^{(\ell)} m_\ell\xi_n(m_{\ell+1}x_\ell) &= 0 \\
c_n{}^{(\ell+1)} m_{\ell+1}\psi_n'(m_{\ell+1}x_\ell) - b_n{}^{(\ell+1)} m_{\ell+1}\xi_n'(m_{\ell+1}x_\ell) - c_n{}^{(\ell)} m_\ell\psi_n'(m_\ell x_\ell) + b_n{}^{(\ell)} m_\ell\xi_n'(m_{\ell+1}x_\ell) &= 0 \\
d_n{}^{(\ell+1)}\psi_n'(m_{\ell+1}x_\ell) - a_n{}^{(\ell+1)}\xi_n'(m_{\ell+1}x_\ell) - d_n{}^{(\ell)}\psi_n'(m_\ell x_\ell) + a_n{}^{(\ell)}\xi_n'(m_{\ell+1}x_\ell) &= 0 \\
c_n{}^{(\ell+1)}\psi_n(m_{\ell+1}x_\ell) - b_n{}^{(\ell+1)}\xi_n(m_{\ell+1}x_\ell) - c_n{}^{(\ell)}\psi_n(m_\ell x_\ell) + b_n{}^{(\ell)}\xi_n(m_{\ell+1}x_\ell) &= 0
\end{aligned}
\tag{B.2}
$$

With the additional boundary conditions for in innermost shell ($\ell = 1$) and finite field at infinity ($\ell = L+1$):

$$
\begin{aligned}
c_n{}^{(L+1)} = d_n{}^{(L+1)} &= 1 \\
a_n{}^{(1)} = b_n{}^{(1)} &= 0
\end{aligned}
\tag{B.3}
$$

with the following substitutions into equation (B.2)

$$
\begin{aligned}
a_n^\ell &\to \frac{1}{m_\ell} a_n{}^\ell \\
b_n^\ell &\to \frac{1}{m_\ell} b_n{}^\ell \\
c_n^\ell &\to \frac{1}{m_\ell} c_n{}^\ell \\
d_n^\ell &\to \frac{1}{m_\ell} d_n{}^\ell
\end{aligned}
\tag{B.4}
$$

it can be rewritten as:

$$
\begin{aligned}
d_n{}^{(\ell+1)}\psi_n(m_{\ell+1}x_\ell) - a_n{}^{(\ell+1)}\xi_n(m_{\ell+1}x_\ell) - d_n{}^{(\ell)}\psi_n(m_\ell x_\ell) + a_n{}^{(\ell)}\xi_n(m_{\ell+1}x_\ell) &= 0 \\
c_n{}^{(\ell+1)}\psi_n'(m_{\ell+1}x_\ell) - b_n{}^{(\ell+1)}\xi_n'(m_{\ell+1}x_\ell) - c_n{}^{(\ell)}\psi_n'(m_\ell x_\ell) + b_n{}^{(\ell)}\xi_n'(m_{\ell+1}x_\ell) &= 0 \\
d_n{}^{(\ell+1)} m_\ell\psi_n'(m_{\ell+1}x_\ell) - a_n{}^{(\ell+1)} m_\ell\xi_n'(m_{\ell+1}x_\ell) - d_n{}^{(\ell)} m_{\ell+1}\psi_n'(m_\ell x_\ell) + a_n{}^{(\ell)} m_{\ell+1}\xi_n'(m_{\ell+1}x_\ell) &= 0 \\
c_n{}^{(\ell+1)} m_{\ell+1}\psi_n(m_{\ell+1}x_\ell) - b_n{}^{(\ell+1)} m_{\ell+1}\xi_n(m_{\ell+1}x_\ell) - c_n{}^{(\ell)} m_\ell\psi_n(m_\ell x_\ell) + b_n{}^{(\ell)} m_\ell\xi_n(m_{\ell+1}x_\ell) &= 0
\end{aligned}
\tag{B.5}
$$

$$
\begin{aligned}
a_n{}^{(\ell+1)}\xi_n'\left(m_{\ell+1}x_\ell\right) - d_n{}^{(\ell+1)}\psi_n'\left(m_{\ell+1}x_\ell\right) &= a_n{}^{(\ell)}\frac{m_{\ell+1}}{m_\ell}\xi_n'\left(m_\ell x_\ell\right) - d_n{}^{(\ell)}\frac{m_{\ell+1}}{m_\ell}\psi_n'\left(m_\ell x_\ell\right) \\
a_n{}^{(\ell+1)}\xi_n\left(m_{\ell+1}x_\ell\right) - d_n{}^{(\ell+1)}\psi_n\left(m_{\ell+1}x_\ell\right) &= a_n{}^{(\ell)}\frac{m_{\ell+1}}{m_\ell}\xi_n\left(m_\ell x_\ell\right) - d_n{}^{(\ell)}\frac{m_{\ell+1}}{m_\ell}\psi_n\left(m_\ell x_\ell\right) \\
b_n{}^{(\ell+1)}\xi_n\left(m_{\ell+1}x_\ell\right) - c_n{}^{(\ell+1)}\psi_n\left(m_{\ell+1}x_\ell\right) &= b_n{}^{(\ell)}\frac{m_{\ell+1}}{m_\ell}\xi_n\left(m_\ell x_\ell\right) - c_n{}^{(\ell)}\frac{m_{\ell+1}}{m_\ell}\psi_n\left(m_\ell x_\ell\right) \\
b_n{}^{(\ell+1)}\xi_n'\left(m_{\ell+1}x_\ell\right) - c_n{}^{(\ell+1)}\psi_n'\left(m_{\ell+1}x_\ell\right) &= b_n{}^{(\ell)}\frac{m_{\ell+1}}{m_\ell}\xi_n'\left(m_\ell x_\ell\right) - c_n{}^{(\ell)}\frac{m_{\ell+1}}{m_\ell}\psi_n'\left(m_\ell x_\ell\right)
\end{aligned}
\tag{B.6}
$$

which can be reorganized into a coupled set of recursion relations for the TM inward propagating d_n^ℓ and outward propagating a_n^ℓ modes.

$$
\begin{aligned}
a_n{}^{(\ell+1)}&\left[\psi_n\left(m_{\ell+1}x_\ell\right)\xi_n'\left(m_{\ell+1}x_\ell\right) - \psi_n'\left(m_{\ell+1}x_\ell\right)\xi_n\left(m_{\ell+1}x_\ell\right)\right] = \\
&a_n{}^{(\ell)}\left[\frac{m_{\ell+1}}{m_\ell}\psi_n\left(m_{\ell+1}x_\ell\right)\xi_n'\left(m_\ell x_\ell\right) - \psi_n'\left(m_{\ell+1}x_\ell\right)\xi_n\left(m_\ell x_\ell\right)\right] \\
-&d_n{}^{(\ell)}\left[\frac{m_{\ell+1}}{m_\ell}\psi_n\left(m_{\ell+1}x_\ell\right)\psi_n'\left(m_\ell x_\ell\right) - \psi_n'\left(m_{\ell+1}x_\ell\right)\psi_n\left(m_\ell x_\ell\right)\right]
\end{aligned}
\tag{B.7}
$$

$$
\begin{aligned}
-d_n{}^{(\ell+1)}&\left[\psi_n'\left(m_{\ell+1}x_\ell\right)\xi_n\left(m_{\ell+1}x_\ell\right) - \psi_n\left(m_{\ell+1}x_\ell\right)\xi_n'\left(m_{\ell+1}x_\ell\right)\right] = \\
&a_n{}^{(\ell)}\left[\frac{m_{\ell+1}}{m_\ell}\xi_n\left(m_{\ell+1}x_\ell\right)\xi_n'\left(m_\ell x_\ell\right) - \xi_n'\left(m_{\ell+1}x_\ell\right)\xi_n\left(m_\ell x_\ell\right)\right] \\
-&d_n{}^{(\ell)}\left[\frac{m_{\ell+1}}{m_\ell}\xi_n\left(m_{\ell+1}x_\ell\right)\psi_n'\left(m_\ell x_\ell\right) - \xi_n'\left(m_{\ell+1}x_\ell\right)\psi_n\left(m_\ell x_\ell\right)\right]
\end{aligned}
\tag{B.8}
$$

And the corresponding TE field components:

$$
\begin{aligned}
b_n{}^{(\ell+1)}&\left[\xi_n\left(m_{\ell+1}x_\ell\right)\psi_n'\left(m_{\ell+1}x_\ell\right) - \xi_n'\left(m_{\ell+1}x_\ell\right)\psi_n\left(m_{\ell+1}x_\ell\right)\right] = \\
&b_n{}^{(\ell)}\left[\frac{m_{\ell+1}}{m_\ell}\psi_n'\left(m_{\ell+1}x_\ell\right)\xi_n\left(m_\ell x_\ell\right) - \psi_n\left(m_{\ell+1}x_\ell\right)\xi_n'\left(m_\ell x_\ell\right)\right] \\
-&c_n{}^{(\ell)}\left[\frac{m_{\ell+1}}{m_\ell}\psi_n'\left(m_{\ell+1}x_\ell\right)\psi_n\left(m_\ell x_\ell\right) - \psi_n\left(m_{\ell+1}x_\ell\right)\psi_n'\left(m_\ell x_\ell\right)\right]
\end{aligned}
\tag{B.9}
$$

$$
\begin{aligned}
-{c_n}^{(\ell+1)}\left[\xi_n'\left(m_{\ell+1}x_\ell\right)\psi_n\left(m_{\ell+1}x_\ell\right)-\xi_n\left(m_{\ell+1}x_\ell\right)\psi_n'\left(m_{\ell+1}x_\ell\right)\right]= \\
{b_n}^{(\ell)}\left[\frac{m_{\ell+1}}{m_\ell}\xi_n'\left(m_{\ell+1}x_\ell\right)\xi_n\left(m_\ell x_\ell\right)-\xi_n\left(m_{\ell+1}x_\ell\right)\xi_n'\left(m_\ell x_\ell\right)\right] \\
-{c_n}^{(\ell)}\left[\frac{m_{\ell+1}}{m_\ell}\xi_n'\left(m_{\ell+1}x_\ell\right)\psi_n\left(m_\ell x_\ell\right)-\xi_n\left(m_{\ell+1}x_\ell\right)\psi_n'\left(m_\ell x_\ell\right)\right]
\end{aligned}
\tag{B.10}
$$

Division of (B.7) by (B.8) and (B.9) by (B.10) yields the needed recursion relations for TM:

$$
\begin{aligned}
&{A_n}^{(\ell+1)}= \\
&({A_n}^{(\ell)}\left[\frac{m_{\ell+1}}{m_\ell}\psi_n\left(m_{\ell+1}x_\ell\right)\xi_n'\left(m_\ell x_\ell\right)-\psi_n'\left(m_{\ell+1}x_\ell\right)\xi_n\left(m_\ell x_\ell\right)\right] \\
&-\left[\frac{m_{\ell+1}}{m_\ell}\psi_n\left(m_{\ell+1}x_\ell\right)\psi_n'\left(m_\ell x_\ell\right)-\psi_n'\left(m_{\ell+1}x_\ell\right)\psi_n\left(m_\ell x_\ell\right)\right])/ \\
&({A_n}^{(\ell)}\left[\frac{m_{\ell+1}}{m_\ell}\xi_n\left(m_{\ell+1}x_\ell\right)\xi_n'\left(m_\ell x_\ell\right)-\xi_n'\left(m_{\ell+1}x_\ell\right)\xi_n\left(m_\ell x_\ell\right)\right] \\
&-\left[\frac{m_{\ell+1}}{m_\ell}\xi_n\left(m_{\ell+1}x_\ell\right)\psi_n'\left(m_\ell x_\ell\right)-\xi_n'\left(m_{\ell+1}x_\ell\right)\psi_n\left(m_\ell x_\ell\right)\right])
\end{aligned}
\tag{B.11}
$$

and TE modes:

$$
\begin{aligned}
&{B_n}^{(\ell+1)}= \\
&({B_n}^{(\ell)}\left[\frac{m_{\ell+1}}{m_\ell}\psi_n'\left(m_{\ell+1}x_\ell\right)\xi_n\left(m_\ell x_\ell\right)-\psi_n\left(m_{\ell+1}x_\ell\right)\xi_n'\left(m_\ell x_\ell\right)\right] \\
&-\left[\frac{m_{\ell+1}}{m_\ell}\psi_n'\left(m_{\ell+1}x_\ell\right)\psi_n\left(m_\ell x_\ell\right)-\psi_n\left(m_{\ell+1}x_\ell\right)\psi_n'\left(m_\ell x_\ell\right)\right]) \\
&({B_n}^{(\ell)}\frac{m_{\ell+1}}{m_\ell}\xi_n'\left(m_{\ell+1}x_\ell\right)\xi_n\left(m_\ell x_\ell\right)-\xi_n\left(m_{\ell+1}x_\ell\right)\xi_n'\left(m_\ell x_\ell\right)\right] \\
&-\left[\frac{m_{\ell+1}}{m_\ell}\xi_n'\left(m_{\ell+1}x_\ell\right)\psi_n\left(m_\ell x_\ell\right)-\xi_n\left(m_{\ell+1}x_\ell\right)\psi_n'\left(m_\ell x_\ell\right)\right]
\end{aligned}
\tag{B.12}
$$

The below logarithmic derivatives are used for their computational stability:

$$
\begin{aligned}
D_n(z)&=\frac{\psi_n'(z)}{\psi_n'(z)} \\
F_n(z)&=\frac{\xi_n'(z)}{\xi_n'(z)}
\end{aligned}
\tag{B.13}
$$

Finally, we rewrite (B.11) and (B.12) with the following substitution:

$$\begin{aligned} \overline{A_n}^{(\ell+1)} &\equiv A_n{}^{(\ell)} \frac{\xi_n(m_\ell x_\ell)}{\psi_n(m_\ell x_\ell)} \\ \overline{B_n}^{(\ell+1)} &\equiv B_n{}^{(\ell)} \frac{\xi_n(m_\ell x_\ell)}{\psi_n(m_\ell x_\ell)} \end{aligned} \tag{B.14}$$

To arrive at the recursion relation that can be implemented in our computer algorithm.

$$\begin{aligned} \overline{A_n}^{(1)} &\equiv 0 \\ \overline{B_n}^{(1)} &\equiv 0 \end{aligned} \tag{B.15}$$

For $\ell < L+1$:

$$\begin{aligned} \overline{A_n}^{(\ell+1)} &= \frac{\psi_n(m_{\ell+1}x_\ell)}{\psi_n(m_{\ell+1}x_{\ell+1})} \frac{\xi_n(m_{\ell+1}x_{\ell+1})}{\xi_n'(m_{\ell+1}x_\ell)} \\ &\frac{\overline{A_n}^{(\ell)}\left[\frac{m_{\ell+1}}{m_\ell}F_n(m_\ell x_\ell) - D_n(m_{\ell+1}x_\ell)\right] - \left[\frac{m_{\ell+1}}{m_\ell}D_n(m_\ell x_\ell) - D_n(m_{\ell+1}x_\ell)\right]}{\overline{A_n}^{(\ell)}\left[\frac{m_{\ell+1}}{m_\ell}F_n(m_\ell x_\ell) - F_n(m_{\ell+1}x_\ell)\right] - \left[\frac{m_{\ell+1}}{m_\ell}D_n(m_\ell x_\ell) - F_n(m_{\ell+1}x_\ell)\right]} \end{aligned} \tag{B.16}$$

$$\begin{aligned} \overline{B_n}^{(\ell+1)} &= \frac{\psi_n(m_{\ell+1}x_\ell)}{\psi_n(m_{\ell+1}x_{\ell+1})} \frac{\xi_n(m_{\ell+1}x_{\ell+1})}{\xi_n'(m_{\ell+1}x_\ell)} \\ &\frac{\overline{B_n}^{(\ell)}\left[\frac{m_{\ell+1}}{m_\ell}D_n(m_{\ell+1}x_\ell) - F_n(m_\ell x_\ell)\right] - \left[\frac{m_{\ell+1}}{m_\ell}D_n(m_{\ell+1}x_\ell) - D_n(m_\ell x_\ell)\right]}{\overline{B_n}^{(\ell)}\left[\frac{m_{\ell+1}}{m_\ell}F_n(m_{\ell+1}x_\ell) - F_n(m_\ell x_\ell)\right] - \left[\frac{m_{\ell+1}}{m_\ell}F_n(m_{\ell+1}x_\ell) - D_n(m_\ell x_\ell)\right]} \end{aligned} \tag{B.17}$$

And to calculate the scattered fields, $\ell = L+1$:

$$\overline{A_n}^{(L+1)} = \frac{\psi_n(x_L)}{\xi_n(x_L)} \frac{\overline{A_n}^{(L)}\left[\frac{1}{m_L}F_n(m_L x_L) - D_n(x_L)\right] - \left[\frac{1}{m_L}D_n(m_L x_L) - D_n(x_L)\right]}{\overline{A_n}^{(L)}\left[\frac{1}{m_L}F_n(m_L x_L) - F_n(x_L)\right] - \left[\frac{1}{m_L}D_n(m_L x_L) - F_n(x_L)\right]} \tag{B.18}$$

$$\overline{B_n}^{(L+1)} = \frac{\psi_n(x_L)}{\xi_n(x_L)} \frac{\overline{B_n}^{(L)}\left[\frac{1}{m_L}D_n(x_L) - F_n(m_L x_L)\right] - \left[\frac{1}{m_\ell}D_n(x_L) - D_n(m_L x_L)\right]}{\overline{B_n}^{(L)}\left[\frac{1}{m_L}F_n(x_L) - F_n(m_L x_L)\right] - \left[\frac{1}{m_L}F_n(x_L) - D_n(m_L x_L)\right]} \tag{B.19}$$

APPENDIX C

FEM ANALYSIS OF PERIODIC PLASMONIC STRUCTURES

Setup of FEM Model

Within the framework of the finite element method (FEM) we simulate the electromagnetic properties of the discretized computational domain shown in figure C.1(left). FEM is a frequency domain method approximating of the solution of a PDE over a closed domain Ω, with simplified basis functions (second order polynomials) on a discrete set of N subdomains $d\Omega_i$, where $\Omega = \bigcup_{i=1}^{N} d\Omega_i$ [119]. This discretized set of domains can be seen in figure C.1(left) as light gray lines forming the system free mesh. Through its efficient use of free meshing to divide Ω into $d\Omega_i$, FEM analysis is well suited to the discretization of problems with complex geometries.

In the context of electromagnetic waves coupled to SPPs, we are concerned with solving the Helmholtz equation for TM polarized waves:

$$\nabla\left(\frac{1}{\varepsilon(\omega)}\nabla H_z\right) - \left(\frac{\omega}{c}\right)^2 H_z = 0 \tag{C.1a}$$

$$\vec{\nabla} \cdot H_z \hat{z} = 0 \tag{C.1b}$$

in the periodic domain of figure C.1. In this periodic system, solving Maxwell's equations reduces to finding the allowed eigenfrequencies, ω_k, for a set of Block plane-

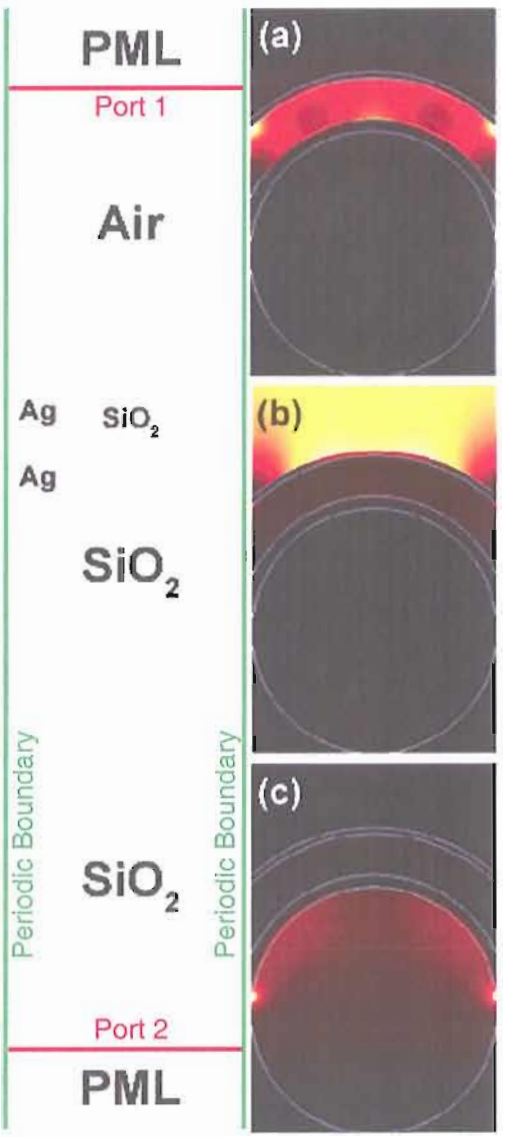

Figure C.1. (left) Geometry and free mesh of the computational domain used in this study. (right) Total energy density plots of (a) an interior surface plasmon mode ($k_x = 0$, $\omega = 1.54$PHz). (b) an external surface plasmon mode ($k_x = 0.5$, $\omega = 1.57$PHz). (c) a localized substrate plasmon mode($k_x = 0$, $\omega = 1.97$PHz).

waves spanning the irreducible Brillouin zone [120]. Because of our use of strongly dispersive metals, we cannot ignore the dependence of ε on ω. This reduces the solution of (C.1) to a nonlinear eigenvalue problem with the form [120, 121]:

$$A(\omega_k)\mathbf{x}_k = \omega_k^2 B(\omega_k)\mathbf{x}_k \tag{C.2}$$

The nonlinear nature of the eigenvalue problem can make the FEM conversion elusive. We solve this problem by first linearizing the eigenvalue problem at an initial frequency ω_0 [122]. Because there exists an infinite number of eigenvalue solutions for a given ω_0, the solution closest to ω_0 must be carefully chosen and iterated upon to retrieve the true eigenvalue ω_k. Using the commercially available software COMSOL [122] this approach is implemented with a two step process: First an eigenmode is found by solving the linearized eigenvalue problem at an in initial ω_0. Next, the eigenmode is used to initialize an iterative Newton's method nonlinear solver to find the true eigenfrequency ω_k. This approach is easily extended to tracing the band structure over the first Brillouin zone by repeated application of the iteration step while the x-component of the parameterizing Bloch vector, $\mathbf{k} = \sqrt{\varepsilon_d}k_0(\sin\theta\hat{x}+\cos\theta\hat{y})$, is slowly varied from 0 to π/a. The boundary conditions are set by the Bloch phase constraint, $H_z(2) = H_z(1)e^{-i\mathbf{k}\cdot\mathbf{R}}$, where the $H_z(X)$ enumerates the field at the periodic boundaries 1 and 2 from figure C.1. Using COMSOL's MATLAB [123] interface, a control script is used to slowly alter the boundary conditions between each iteration by changing k_x. We achieve rapid convergence to the new eigenfrequency, $\omega_{k'}$, by us-

ing the previous solution for the $(\omega_k, H_z(x,y))$ as the initial guess for each iteration step[122]. An example of this script can be found below.

Computational Geometry

Shown on the left hand side of figure C.1 are the geometry and discretized mesh of the FEM computational domain. Through our use of periodic boundary conditions we are representing an infinite array of close-packed silica cylinders with radius r_1. The index of refraction used for all silica regions was $n_d = 1.42$. The rods form a 1-dimensional crystal of periodicity $a = 2r_1$ which rests upon a semi-infinite silica substrate. The cylinders are layered in the positive half-plane with concentric cylindrical shells defined by their radii (r_2, r_3 and r_4) or corresponding shell thickness $S = |r_2 - r_1|$, $L = |r_3 - r_2|$, $T = |r_4 - r_3|$ and their constituent material optical properties. When truncated at the intersection of the adjacent cylinder's shell, the "shells" in fact form a conformal layer along the surface of the cylinder array. By specifying that the layers are silver, silica and silver we form a uniquely modulated MDM geometry simultaneously supporting the three distinctive electromagnetic eigenmodes shown in figures C.1(a)-(c). These modes can be placed into the three classes that we have seen in the case of the MDM sphere: exterior surface plasmons (EPS) along the silver-air interface and the substrate silica-air interface, interior surface plasmons (ISP) confined to the dielectric layer between the adjacent metal films and associated with the coupled plasmons of the two interior silver-silica interfaces, and localized

surface plasmon (LSP) modes associated with the excitation of plasmons at the cusps formed by the intersections of rods or layers.

Silver was chosen in these simulations because it has the lowest losses in the visible/NIR spectral region. As described in chapter II, we use the standard Drude model to characterize the dispersion of the silver film. However, due to the conventions of the COMSOL application we re-express $\varepsilon_m(\omega)$ in terms of conductivity:

$$\varepsilon(\omega) = \varepsilon_r - i\frac{\sigma(\omega)}{\varepsilon_0\omega} \tag{C.3a}$$

$$\sigma(\omega) = \frac{\sigma_{dc}}{1 + i\tau\omega} \tag{C.3b}$$

The astute reader may note the negative imaginary part of $\varepsilon_m(\omega)$. This may look odd to physicists, but it is not incorrect. It is merely the engineering convention used by COMSOL [122]. The best fit parameters used were: $\varepsilon = 4.1$, $\sigma_{dc} = 62^{\mathrm{S}}/_{\mathrm{m}}$ and $\tau = 4 \cdot 10^{-14}$s. In this study we choose to focus on a specific geometry with $r_1 = 300$nm, $S = 30$nm, $L = 100$nm, and $T = 15$nm. As found in chapter IV the strength of the SPP coupling between layers is governed by an exponential decay characterized by silvers skin depth ($\delta \sim 25\,\mathrm{nm}$). The width of the silver layers was chosen to allow significant coupling between the three mode types, while remaining thick enough to support well defined eigenmodes such as shown in figure C.1(a)-(c).

The intersections of the spheres and layers with computational boundaries have been rounded (2.5nm radius) to reduce instabilities in the computation associated with infinitely sharp cusps. This results in 'necked' intersections with the boundaries and the substrate. A situation that is in fact, closer to real physical systems.

The size of the silica spacer, $L = 100\text{nm}$, was chosen to be small enough to constrain SPP excitations in the dielectric gap to be of the symmetric TM, or long-range SPP type [23]. As shown in chapter II, interaction of the two metal surfaces splits the single interface SPP into a symmetric and anti-symmetric pair. However, the anti-symmetric TM mode is forbidden when $L \lesssim \lambda/(2n_d)$, where $n_d = \sqrt{\varepsilon_d}$ is the gap dielectric refractive index [124]. Thus, for the $L = 100\,\text{nm} \sim \lambda/10$ geometry simulated here, we are well within the regime of exclusive symmetric TM SPP propagation.

Boundary Conditions

Periodic Flouqet-Bloch boundary conditions were employed at the left and right boundaries to simulate an infinite array of MDM coated cylinders. In FEM this boundary condition is implemented by employing a Bloch phase constraint $H(1)e^{-i\mathbf{K}\cdot\mathbf{R}} = H(2)$ on the tangential field components (H_z and E_y) at the periodic boundaries 1 and 2, where the reciprocal lattice vector $\mathbf{K} = 2\pi/a \cdot \hat{x}$ and $R = a \cdot \hat{x}$.

Typical in FEM, the open boundary conditions of scattering problems are difficult to correctly simulate. To overcome this difficulty we utilized perfectly matched layers 1.2μm long, at the top and bottom of the computational domain [119]. This allowed the simulation of far-field plane-wave scattering, while inducing a minimum amount of error due to artificial reflections from computational boundaries.

Mesh parameters

Care must be taken when modeling metallic nanosystems due the rapid decay of the evanescent field near the metal surface. We were careful to select a mesh size that

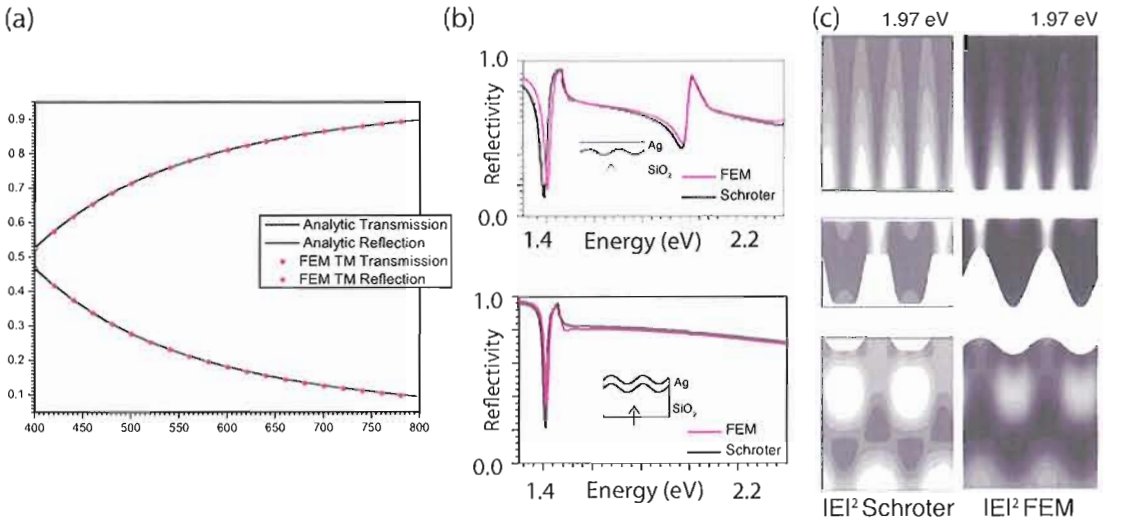

Figure C.2. (a) Comparison of FEM with analytic calculation for normal transmission and reflection through (a) a 27nm thick silver film in air and, (b) asymmetrically (top) and conformally (bottom) modulated sinusoidal silver films from [125]. (c) E-field intensity comparison with Schröter [125] at $\hbar\omega = 1.97\,\text{eV}$. The reflectivity dip at 1.97 eV shows the excitation of a SPP on the air-silver interface.

minimized the computational error while keeping the computation time tractable. Typical mesh sizes of four elements per decay length (skin depth) of 20nm, or a element linear dimension of 5nm, where used near the metal-dielectric interface and inside metal domains. Outside of the metal subdomains, a conservative $\sim \lambda/(20n_d)$ mesh size (30nm typical) was used. Mesh convergence tests showed that this was sufficient to maintain an estimated computational precision of approximately one percent.

To estimate the solution accuracy as a function of mesh size, an FEM simulation of a 27nm metal film was discretized using the same constraints and transmission calculations were compared to the the analytic solution [114]. This is shown in fig-

ure C.2(a). Additionally we have examined the accuracy of the FEM mesh conditions with comparison to Schröter and Heitmann [125]. They have used an analytical method based on coordinate transforms and the transfer-matrix method, to calculate the transmission of light through modulated thin silver films on silica substrates. The accurate reproduction of their results can be found in figures C.2(b) and (c).

MATLAB Band Diagram Script

The following MATLAB scripts can be used to generate the reflection, transmission and mode diagrams of *dispersive* periodic structures. Having setup your `fem` structure (geometry, sub-domain parameters and mesh) using COMSOL, input it into the MATLAB command interface (CTRL-F) and run the following scripts in the order in which they are shown below.

Initial Frequency Sweep

```
function [omegaSolnSort, rtfems, rtfullfem] = evFreqSweep(fem, OmegaRange, kstart, TOL)

%Set the search parameters in frequency space
delOmega = OmegaRange(3);
OmegaStart = OmegaRange(1);
OmegaStop = OmegaRange(2);
omegaVector = OmegaStart:delOmega:OmegaStop;
omegaSoln = [];


%Update magnitude of k
fem.const{2*strmatch('k',fem.const(1:2:end),'exact')} = kstart;

% Initial solution to eigenvalue problem
counter = 1;
omegaSoln = [];

for ind=1:length(omegaVector)
    fprintf(1,'Initalvalue: %g',omegaVector(ind));

    fem.appl{1}.prop.analysis = 'eigen';
    fem = multiphysics(fem);
```

```
23      fem.xmesh = meshextend(fem);
24
25      init = asseminit(fem,'init','0');
26      try
27      fem.sol=femeig(fem, ...
28          'init',init, ...
29          'complexfun','on', ...
30          'conjugate','on', ...
31          'solcomp',{'Hz'}, ...
32          'neigs',1, ...
33          'shift',-i*omegaVector(ind), ...
34          'linsolver','pardiso', ...
35          'maxeigit',100, ...
36          'eigref',sprintf('-i*%g',omegaVector(ind)));
37
38  % Store solution guess for all bands
39      catch
40          fprintf(1,'---NO EVs near %g\n',omegaVector(ind));
41          continue;
42      end
43
44      fprintf(1,'--EV-->%g',-imag(fem.sol.lambda));
45
46      fem.appl{1}.prop.analysis = 'harmonic';
47      fem = multiphysics(fem);
48      fem.xmesh = meshextend(fem);
49
50  %Final refinment of inital EVs using the nonlinear
51  %interative solver
52         init = asseminit(fem,'u',fem.sol);
53      try
54          [fem.sol stp]=femnlin(fem, ...
55          'init',init, ...
56          'linsolver','pardiso', ...
57          'complexfun','on', ...
58          'conjugate','on',...
59          'solcomp',{'Hz','freq'}, ...
60          'outcomp',{'Hz','freq'}, ...
61          'out', {'sol', 'stop'}, ...
62          'Ntol', 1e-1);
63      catch
64          fprintf(1,'--->No eigenfrequency found, skipping\n');
65          continue;
66      end
67      tempom = postint(fem,'nu_rfwh','edim',0,'dl',1,'solnum','all')*2*pi;
68      tempwt = abs(real(tempom) - omegaVector(ind));
69      if(stp~=0)
70          fprintf(1,'Did not converge, skipping %g\n',tempom);
71          continue;
72      else
73          fprintf(1,'--NL-->%g',tempom);
74      end
75
76     if(counter>1)
77      if ( abs((omegaSoln(counter-1)-tempom)/omegaSoln(counter-1)) > TOL)
78
79         omegaSoln(counter)=tempom;
80         wt(counter) = tempwt;
81         initset{counter} = init;
82         femset{counter} = fem.sol;
83         counter = counter + 1;
84         fprintf(1,'-->New, Keeping\n');
85
```

```
86      elseif(wt(counter-1)>tempwt)
87
88          omegaSoln(counter-1)=tempom;
89          initset{counter-1} = init;
90          femset{counter-1} = fem.sol;
91          wt(counter-1) = tempwt;
92          fprintf(1,'-->Closer, Keeping\n');
93
94       else
95           fprintf(1,'-->Repeat, Skipping\n');
96       end
97      else
98           omegaSoln(counter) = tempom;
99           wt(counter) = tempwt;
100          initset{counter} = init;
101          femset{counter} = fem.sol;
102          counter = counter + 1;
103          fprintf(1,'-->First, Keeping\n');
104     end
105 end
106
107 omegaSolnSort = omegaSoln;
108 rtfems = femset;
109 rtinits = initset;
110 rtfullfem = fem;
111 end
```

Iteration of Initial Eigenvalues

```
1   function [evList, femOut] = evIterate(femStruct, femSolIn, evIn)
2
3   TOL = 1e-6; % Tolerance for floating point comparison
4
5   %Final refinment of inital EVs using the nonlinear
6   %interative solver
7
8   % Ensure harmonic analysis, and an extended mesh
9   femStruct.appl{1}.prop.analysis = 'harmonic';
10  femStruct = multiphysics(femStruct);
11  femStruct.xmesh = meshextend(femStruct);
12
13  %Container varibles for solution results
14  omega0 =[];
15  sol = {};
16  counter = 1;
17  numoms = length(femSolIn);
18
19  for ind=1:numoms % Iterate on the reduced set of k=0 EVs
20
21  fprintf(1,'Refining %i/%i, Inital eigenfrequency[Hz]: %g+i*%g',...
22      ind,numoms, real(evIn(ind)),imag(evIn(ind)));
23
24          %Construct the inital mesh solution to seed the nonlinear sovler
25        evsol = femsol(femSolIn{ind}.u, 'lambda', evIn(ind));
26        init = asseminit(femStruct, 'init', evsol);
27
28       try
29         femStruct.sol=femnlin(femStruct, ...
30          'init',init, ...
```

```
        'linsolver','pardiso', ...
        'complexfun','on', ...
        'conjugate','on',...
        'solcomp',{'Hz','freq'}, ...
        'outcomp',{'Hz','freq'});

    catch
        fprintf(1,'--->Refinement Failed, skipping\n');
        continue;
    end

    sol{counter} = femStruct.sol;
    omega0(counter)= postint(femStruct,'nu_rfwh','edim',0,'dl',1,'solnum','all')*2*pi;
    fprintf(1,'--->%g+i*%g\n',real(omega0(counter)),imag(omega0(counter)));
    counter = counter + 1;
end

[evList, ommask] = remDups(omega0,TOL);
PossibleIndex = 1:length(ommask);
maskvector = PossibleIndex(logical(ommask));
evList = evIn(maskvector);
femOut = sol(maskvector);

end
```

Band Trace

```
function [bandenergy, bandkvalues] = BandTrace(fem, omegaIn, femSolIn, KL)

newtmin = 1e-8;

kstart = KL(1);
kend = KL(2);
kdel = KL(3);
kminfactor = 10;
klist = kstart:kdel:kend;

fprintf(1,'Calculating Band Structure:\n');

bandenergy = cell(1,length(omegaIn));
bandkvalues = cell(1, length(omegaIn));
counter = 1;

mkdir('femsolsTM');
save(sprintf('femsolsTM/femfull_kstart%2.1f.mat',kstart), 'fem');

for ind=1:length(omegaIn)
    fprintf(1,'Starting at ev:%g--->',omegaIn(ind));

    evsol = femsol(femSolIn{ind}.u, 'lambda', omegaIn(ind));
    init = asseminit(fem, 'init', evsol);

     fem.sol=femnlin(fem, ...
        'init',init, ...
        'complexfun','on', ...
        'conjugate','on', ...
        'solcomp',{'Hz','freq'}, ...
        'outcomp',{'Hz','freq'}, ...
        'pname','k', ...
```

```
33          'plist',klist, ...
34          'pinitstep',abs(kdel), ...
35          'pminstep',abs(kdel)/kminfactor, ...
36          'pmaxstep',abs(kdel), ...
37          'oldcomp',{}, ...
38          'porder',0, ...
39          'Maxiter',50,...
40          'minstep',newtmin, ...
41          'linsolver','pardiso');
42
43      bandenergy{counter} = postint(fem,'nu_rfwh','edim',0,'dl',1,'solnum','all')*2*pi;
44      bandkvalues{counter} = fem.sol.plist;
45
46      %save the data
47      fprintf(1,'Saving Data-->');
48      femsolu = fem.sol;
49      eigenfreq = bandenergy{counter};
50      kvector = bandkvalues{counter};
51      save(sprintf('femsolsTM/band%d_femsol_kstart%2.1f.mat',counter,kstart), 'femsolu');
52      save(sprintf('femsolsTM/band%d_energy_kstart%2.1f.mat',counter,kstart), 'eigenfreq');
53      save(sprintf('femsolsTM/band%d_kvector_kstart%2.1f.mat',counter,kstart), 'kvector');
54      counter = counter +1;
55      fprintf(1,'Done\n');
56
57  end
58
59    save(sprintf('bands_kstart%2.1f.mat',kstart), 'bandenergy','bandkvalues');
60
61  end
```

BIBLIOGRAPHY

[1] S. Maier, *Plasmonics: Fundamentals and Applications* (New York: Springer, 2007).

[2] A. Sommerfeld, Wiedemanns Annalen **67**, 233 (1899).

[3] J. Zenneck, Annalen Physik **23**, 846 (1907).

[4] G. Mie, Annalen Physik **25**, 377 (1908).

[5] R. Wood, Proceedings of the Physical Society of London **18**, 269 (1902).

[6] M. Faraday, Philosophical Transactions of the Royal Society of London **147**, 145 (1857).

[7] *ISI Web of Knowledge*, URL `http://www.isiknwoledge.com/`.

[8] U. Fano, Journal of the Optical Society of America **31**, 213 (1941).

[9] R. Ritchie, E. Arakawa, J. Cowan, and R. Hamm, Physical Review Letters **21**, 1530 (1968).

[10] R. Ritchie, Physical Review **106**, 874 (1957).

[11] C. Powell and J. Swan, Physical Review **118**, 640 (1960).

[12] M. Daniel and D. Astruc, Chemical Reviews **104**, 293 (2004).

[13] *Fraday Museum Royal Insitution* (2008), URL `http://www.rigb.org/`.

[14] G. Moore, Electronics Journal **38**, 114 (1965).

[15] W. Barnes, A. Dereux, and T. Ebbesen, Nature **424**, 824 (2003).

[16] J. Homola, S. Yee, and G. Gauglitz, Sensors and Actuators B **54**, 3 (1999).

[17] C. Loo, A. Lowery, N. Halas, J. West, and R. Drezek, Nano Letters **5**, 709 (2005).

[18] M. Seydack, Biosensors and Bioelectronics **20**, 2454 (2005).

[19] T. Ebbesen, H. Lezec, H. Ghaemi, T. Thio, and P. Wolff, Nature **391**, 667 (1998).

[20] R. Charbonneau, P. Berini, E. Berolo, and E. Lisicka-Shrzek, Optics Letters **25**, 844 (2000).

[21] M. Quinten, A. Leitner, J. Krenn, and F. Aussenegg, Optics Letters **23**, 1331 (1998).

[22] S. Maier, P. Kik, H. Atwater, S. Meltzer, E. Harel, B. Koel, and A. Requicha, Nature Materials **2**, 229 (2003).

[23] J. Dionne, L. Sweatlock, H. Atwater, and A. Polman, Physical Review B **73** (2006).

[24] G. Veronis and S. Fan, Applied Physics Letters **87** (2005).

[25] R. Zia, M. Selker, P. Catrysse, and M. Brongersma, Journal of the Optical Society of America A **21**, 2442 (2004).

[26] S. Bozhevolnyi, V. Volkov, E. Devaux, J. Laluet, and T. Ebbesen, Nature **440**, 508 (2006).

[27] R. Charbonneau, N. Lahoud, G. Mattiussi, and P. Berini, Optics Express **13**, 977 (2005).

[28] I. Smolyaninov, D. Mazzoni, J. Mait, and C. Davis, Physical Review B **56**, 1601 (1997).

[29] L. Yin, V. Vlasko-Vlasov, J. Pearson, J. Hiller, J. Hua, U. Welp, D. Brown, and C. Kimball, Nano Letters **5**, 1399 (2005).

[30] H. Ditlbacher, J. Krenn, G. Schider, A. Leitner, and F. Aussenegg, Applied Physics Letters **81**, 1762 (2002).

[31] V. M. Shalaev, Nature Photonics **1**, 41 (2007).

[32] D. Smith, J. Pendry, and M. Wiltshire, Science **305**, 788 (2004).

[33] V. Lomakin, Y. Fainman, Y. Urzhumov, and G. Shvets, Optics Express **14**, 11164 (2006).

[34] J. Pendry, Physical Review Letters **85**, 3966 (2000).

[35] A. Alu and N. Engheta, IEEE Transactions on Antennas and Propagation **51**, 2558 (2003).

[36] U. Leonhardt, Science **312**, 1777 (2006).

[37] J. Pendry, D. Schurig, and D. Smith, Science **312**, 1780 (2006).

[38] C. Enkrich, M. Wegener, S. Linden, S. Burger, L. Zschiedrich, F. Schmidt, J. Zhou, T. Koschny, and C. Soukoulis, Physical Review Letters **95** (2005).

[39] V. Veselago, Soviet Physics Uspekhi-Ussr **10**, 509 (1968).

[40] A. Grbic and G. Eleftheriades, Physical Review Letters **92** (2004).

[41] R. Shelby, D. Smith, and S. Schultz, Science **292**, 77 (2001).

[42] T. Yen, W. Padilla, N. Fang, D. Vier, D. Smith, J. Pendry, D. Basov, and X. Zhang, Science **303**, 1494 (2004).

[43] A. Grigorenko, A. Geim, H. Gleeson, Y. Zhang, A. Firsov, I. Khrushchev, and J. Petrovic, Nature **438**, 335 (2005).

[44] A. Alu and N. Engheta, Journal of the Optical Society of America B **23**, 571 (2006).

[45] H. Shin and S. Fan, Physical Review Letters **96** (2006).

[46] C. Rohde, K. Hasegawa, and M. Deutsch, Optics Letters **32**, 415 (2007).

[47] D. Schurig, J. J. Mock, B. J. Justice, S. A. Cummer, J. B. Pendry, A. F. Starr, and D. R. Smith, Science **314**, 977 (2006).

[48] I. Smolyaninov, Y. Hung, and C. Davis, Arxiv preprint arXiv:0709.2862 (2007).

[49] E. Hutter and J. Fendler, Advanced Materials **16**, 1685 (2004).

[50] A. Haes and R. Van Duyne, Laser Focus World **39**, 153 (2003).

[51] A. Haes, D. Stuart, S. Nie, and R. Van Duyne, Journal of Fluorescence **14**, 355 (2004).

[52] M. Moskovits, Reviews of Modern Physics **57**, 783 (1985).

[53] S. Löfås and B. Johnsson, Journal of the Chemical Society **1990**, 1526 (1990).

[54] B. Johnsson, S. Löfís, and G. Lindquist, Analytical Biochemistry **198**, 268 (1991).

[55] R. Karlsson, A. Michaelsson, and L. Mattsson, Journal of Immunological Methods **145**, 229 (1991).

[56] U. Jonsson, L. Fagerstam, B. Ivarsson, B. Johnsson, R. Karlsson, K. Lundh, S. Lofas, B. Persson, H. Roos, and I. Ronnberg, Biotechniques **11**, 620 (1991).

[57] A. Haes and R. Van Duyne, Journal of the American Chemical Society **124**, 10596 (2002).

[58] E. Palik, *Handbook of Optical Constants of Solids* (Academic Press, 1985).

[59] E. Fontana, IEEE Transactions On Microwave Theory and Techniques **50**, 82 (2002).

[60] C. Yonzon, E. Jeoungf, S. Zou, G. Schatz, M. Mrksich, and R. Van Duyne, Journal of the American Chemical Society **126**, 12669 (2004).

[61] A. McFarland and R. Van Duyne, Nano Letters **3**, 1057 (2003).

[62] K. Kneipp, Y. Wang, H. Kneipp, L. Perelman, I. Itzkan, R. Dasari, and M. Feld, Physical Review Letters **78**, 1667 (1997).

[63] S. Nie and S. Emery, Science **275**, 1102 (1997).

[64] C. Haynes and R. Van Duyne, Journal of Physical Chemistry B **107**, 7426 (2003).

[65] C. Rohde, K. Hasegawa, and M. Deutsch, Physical Review Letters **96** (2006).

[66] L. Davis and M. Deutsch, in preparation.

[67] S. Sershen, S. Westcott, N. Halas, and J. West, Journal of Biomedical Materials Research **51**, 293 (2000).

[68] S. Pillai, K. Catchpole, T. Trupke, and M. Green, Journal of Applied Physics **101**, 093105 (2007).

[69] N. Engheta, A. Salandrino, and A. Alŭ, Physical Review Letters **95**, 95504 (2005).

[70] E. Betzig and J. Trautaman, Science **257**, 189 (1992).

[71] X. Luo and T. Ishihara, Applied Physics Letters **84**, 4780 (2004).

[72] W. Srituravanich, N. Fang, C. Sun, Q. Luo, and X. Zhang, Nano Lett **4**, 1085 (2004).

[73] E. Altewischer, M. van Exter, and J. Woerdman, Nature **418**, 304 (2002).

[74] D. E. Chang, A. S. Sorensen, E. A. Demler, and M. D. Lukin, Nature Physics **3**, 807 (2007).

[75] D. Bergman and M. Stockman, Physical Review Letters **90**, 27402 (2003).

[76] E. Prodan, C. Radloff, N. Halas, and P. Nordlander, Science **302**, 419 (2003).

[77] H. Raether, *Surface Plasmons on Smooth and Rough Surfaces and on Gratings* (Springer-Verlag New York, 1988).

[78] E. Economou, Physical Review **182**, 539 (1969).

[79] N. Ashcroft and N. Mermin, *Solid State Physics* (Holt, Rinehart and Winston New York, 1976).

[80] B. Prade, J. Vinet, and A. Mysyrowicz, Physical Review B **44**, 13556 (1991).

[81] H. Shin, M. Yanik, S. Fan, R. Zia, and M. Brongersma, Applied Physics Letters **84**, 4421 (2004).

[82] K. Hasegawa, C. Rohde, and M. Deutsch, Optics Letters **31**, 1136 (2006).

[83] C. Bohren and D. Huffman, *Absorption and Scattering of Light by Small Particles* (Wiley, New York, 1998).

[84] A. Aden and M. Kerker, Journal of Applied Physics **22**, 1242 (2004).

[85] R. Bhandari, Applied Optics **24**, 1960 (1985).

[86] O. Toon and T. Ackerman, Applied Optics **20**, 3657 (1981).

[87] W. Yang, Applied Optics **42**, 1710 (2003).

[88] V. Cachorro and L. Salcedo, Journal of Electromagnetic Waves and Applications **5**, 913 (1991).

[89] S. Lecler, Y. Takakura, and P. Meyrueis, Optics Letters **30**, 2641 (2005).

[90] T. Kaiser and G. Schweiger, Computers in Physics **7**, 682 (1993).

[91] D. Zwillinger et al., *Standard Mathematical Tables and Formulae* (Chapman & Hall/CRC Boca Raton, Fl, 2003).

[92] Z. Wang, B. Luk'yanchuk, M. Hong, Y. Lin, and T. Chong, Physical Review B **70** (2004).

[93] T. Kelf, Y. Sugawara, J. Baumberg, M. Abdelsalam, and P. Bartlett, Physical Review Letters **95** (2005).

[94] A. Moroz, Physical Review Letters **83**, 5274 (1999).

[95] S. Oldenburg, R. Averitt, S. Westcott, and N. Halas, Chemical Physics Letters **288**, 243 (1998).

[96] J. Jackson, S. Westcott, L. Hirsch, J. West, and N. Halas, Applied Physics Letters **82**, 257 (2003).

[97] A. Alu and N. Engheta, Physical Review E **72** (2005).

[98] S. Mohamed, O. Kappertz, T. Pedersen, R. Drese, and M. Wuttig, Physica Status Solidi A **198**, 224 (2003).

[99] R. Ruppin, Physics Letters A **299**, 309 (2002).

[100] D. Smith, H. Chang, K. Fuller, A. Rosenberger, and R. Boyd, Physical Review A **69** (2004).

[101] A. P. Hibbins, W. A. Murray, J. Tyler, S. Wedge, W. L. Barnes, and J. R. Sambles, Physical Review B **74** (2006).

[102] A. Christ, T. Zentgraf, J. Kuhl, S. Tikhodeev, N. Gippius, and H. Giessen, Physical Review B **70**, 125113 (2004).

[103] N. Bonod, S. Enoch, L. Li, E. Popov, and M. Neviere, Optics Express **11**, 482 (2003).

[104] E. Sánchez, L. Novotny, and X. Xie, Physical Review Letters **82**, 4014 (1999).

[105] N. A. Issa and R. Guckenberger, Plasmonics **2**, 31 (2007).

[106] W. Stöber, A. Fink, and E. Bohn, Journal of Colloid and Interface Science **26**, 62 (1968).

[107] H. Giesche, Journal of the European Ceramic Society **14**, 205 (1994).

[108] H. Giesche, Journal of the European Ceramic Society **14**, 189 (1994).

[109] *Deutsch Group Software Repository*, URL `http://mo.uoregon.edu`.

[110] S. Wong, V. Kitaev, and G. Ozin, Journal of the American Chemical Society **125**, 15589 (2003).

[111] R. Rengarajan, D. Mittleman, C. Rich, and V. Colvin, Physical Review E **71** (2005).

[112] D. Hall, P. Underhill, and J. Torkelson, Polymer Engineering and Science **38**, 2039 (1998).

[113] X. Huang, L. Bao, X. Cheng, L. Guo, S. Pang, and A. Yee, Journal of Vacuum Science & Technology B **20**, 2872 (2002).

[114] M. Born and E. Wolf, *Principles of Optics* (Pergamon Press New York, 1980).

[115] A. Haes and R. Van Duyne, Analytical Chemistry **68**, 2629 (1996).

[116] C. Haynes and R. Van Duyne, Journal of Physical Chemistry B **105**, 5599 (2001).

[117] C. Haynes, A. McFarland, M. Smith, J. Hulteen, and R. Van Duyne, Journal of Physical Chemistry B **106**, 1898 (2002).

[118] C. Haynes and R. Van Duyne, Nano Letters **3**, 939 (2003).

[119] J. Jin, *The Finite Element Method in Electromagnetics* (Wiley, New York, 1993).

[120] B. Hiett, J. Generowicz, S. Cox, M. Molinari, D. Beckett, and K. Thomas, IEEE Proceedings on Science Measurement and Technology **149**, 293 (2002).

[121] M. Davanco, Y. Urzhumov, and G. Shvets, Optics Express **15**, 9681 (2007).

[122] *COMSOL Mutliphysics v3.4* (2008), URL `http://www.comsol.com`.

[123] *MATLAB v2007b*, URL `http://www.mathworks.com/`.

[124] I. Avrutsky, I. Salakhutdinov, J. Elser, and V. Podolskiy, Physical Review B **75** (2007).

[125] U. Schroter and D. Heitmann, Physical Review B **60**, 4992 (1999).